

Galvanic Mechanism of Localized Corrosion for Mild Steel in Carbon Dioxide
Environments

A dissertation presented to
the faculty of
the Russ College of Engineering and Technology of Ohio University

In partial fulfillment
of the requirements for the degree
Doctor of Philosophy

Jiabin Han

November 2009

© 2009 Jiabin Han. All Rights Reserved.

This dissertation titled
Galvanic Mechanism of Localized Corrosion for Mild Steel in Carbon Dioxide
Environments

by

JIABIN HAN

has been approved for
the Department of Chemical and Biomolecular Engineering
and the Russ College of Engineering and Technology by

Srdjan Nešić

Professor of Chemical and Biomolecular Engineering

Dennis Irwin

Dean, Russ College of Engineering and Technology

Abstract

HAN, JIABIN, Ph.D., November 2009, Chemical Engineering

Galvanic Mechanism of Localized Corrosion for Mild Steel in Carbon Dioxide Environments (165 pp.)

Director of Dissertation: Srdjan Nešić

Historically, the mechanism of localized corrosion in CO₂ (sweet) environments has been poorly understood. This shortcoming is an obstacle in the development of corrosion control and protection protocols. The purpose of this PhD project was to explore and understand localized sweet corrosion mechanisms through systematic study. An artificial pit cell was developed in order to directly measure the galvanic current resulting from localized corrosion propagation. Thus, galvanic mechanisms of localized CO₂ corrosion were elucidated. It was found that two surfaces coexist as termed anode (bare surface in the pit) and cathode (surrounding surface usually covered by corrosion scales) with open circuit potentials (OCP) for these different surfaces being different under the same bulk environments. This potential difference can be the driving force for localized corrosion propagation when the reactions on the two surface balance (a mixed potential is reached). A “gray zone” criterion was determined through experiments and theory to explain localized CO₂ corrosion propagation. It was concluded that localized corrosion propagates when the conditions are near the saturation point for iron carbonate, *i.e.* in the “gray zone”. Under this condition, which is neither highly supersaturated nor undersaturated, the pit area stays scale free while the scale remains on the surrounding cathode surface. Electrochemical studies demonstrated that passivation, especially

spontaneous passivation, can occur on the cathode surface and that results in a higher open circuit potential on the cathode. Surface analysis using GIXRD and TEM/EDX showed that beneath an iron carbonate film formed first a passive film is formed due to the local high pH conditions underneath the FeCO_3 film. The passive film was identified and confirmed to be magnetite, Fe_3O_4 , under the test conditions using X-ray diffraction (XRD) with grazing incidence, its thickness being at the nanometer level, as detected by TEM/EDX. This passive film is responsible for the spontaneous passivation of the surface and causes the more positive open circuit potential compared with that on the bare surface (pit area). In order to confirm the passivation mechanism, a surface pH probe was developed. The surface pH measurements under simulated iron carbonate scale showed a higher pH value, which was high enough to reach passivation as defined by the Pourbaix diagram. An electrochemical model was constructed based on the described galvanic mechanisms of localized CO_2 corrosion, having the capability to predict bare surface uniform corrosion, filmed surface passivation and galvanic effects for localized corrosion propagation, in other words, a steady state “worst case” localized corrosion propagation scenario.

Approved: _____

Srdjan Nešić

Professor of Chemical and Biomolecular Engineering

Acknowledgments

I want to show my appreciation for my PhD advisor, Dr. Srdjan Nešić, for his dedication, direction and guidance for this project. I became exposed to a new world of science after his training. With his help and supervision, I grew steadily from a naïve young man toward a mature scientist both in terms academic and social. I appreciate his help and the father-like care from the bottom of my heart.

I would like to express my deep love and appreciation to my wife, Jing Chen. She was, is and will always be standing behind me whenever I confront challenges and difficulties. I never would have achieved all this without her love and support. I also want to express my thanks to my parents, Wenji Han and Xinguo Huo for their support to pursue my higher education overseas. My younger brother, Jiatao Han, takes all the responsibility to take care of the whole family and release me so that I can concentrate on my research.

My research was benefited greatly from the involvement and discussions with Dr. David Young. His expertise in chemistry was a well of fortune for me. I benefited from his direct contribution in the part of the thesis related passive film analysis and identification. He is also served as a warm hearted English language instructor and never became frustrated by my poor English skills.

The surface analysis was achieved with the help of several collaborators: Professor David C. Ingram from The John E. Edwards Accelerator Laboratory of Ohio University for RBS and XPS, Dr. Akhilesh Tripathi from Rigaku Inc. for XRD and GIXRD and Hendrik Colijn from CEOF of the Ohio State University for TEM/EDX.

I take this chance to thank Bruce Brown, my project leader for his help and advice during this research program. Thanks also go to technicians John Goettge, Danny Cain and Albert Schubert for their help in the design and manufacture of the testing equipment.

I owe my thanks to a former graduate student Dr. Wei Sun. I “fought” with her on academic and other issues, but I learned so much from her advice which served me well in my research as well as personal life. I also express my thanks to Dr. Ziru Zhang for beneficial discussion and his kind help during my internship at BP, Houston. I want to thank Francois Ayello and Vanessa Fajardo Nino de Rivera which made a friendly and stimulating office environment and made sure I am in good mood every day. The wonderful collaboration with other students at ICMT is appreciated.

The members of graduate committee including Dr. Srdjan Nešić, Dr. Tingyue Gu, Dr. Dusan Sormaz, Dr. David Ingram and Dr. Michael P. Jensen are appreciated for their hard work in reviewing this dissertation.

Dr. Jinsuo Zhang and Dr. Bill Carey are appreciated for their offer of the Summer internship at Los Alamos National Laboratory. I am grateful for this opportunity to expand my knowledge and research experience at the Los Alamos National Laboratory, and develop my future career in the research field. I also acknowledge their efforts on supervising me during this period.

I express my thanks to the sponsor companies for their financial support and academic advisory role in my research.

Table of Contents

Abstract	3
Acknowledgments.....	5
List of Tables	11
List of Figures.....	12
Chapter 1: Introduction	21
1.1 Literature review	21
1.1.1 <i>CO₂ corrosion</i>	21
1.1.2 <i>Localized CO₂ corrosion on mild steel</i>	22
1.2 Objectives	24
Chapter 2: Investigation of the galvanic mechanism for localized CO ₂ corrosion propagation using artificial pit technique	26
2.1 Introduction.....	26
2.2 Experimental design.....	30
2.2.1 <i>Artificial pit design</i>	30
2.2.2 <i>Corrosion cell setup</i>	32
2.2.3 <i>Experimental procedure</i>	32
2.2.4 <i>Test matrix</i>	35
2.3 Results and discussion	36
2.3.1 <i>Galvanic mechanism of localized CO₂ corrosion propagation</i>	36
2.3.2 <i>Conditions required for steady localized CO₂ corrosion propagation</i>	40

2.3.3	<i>Environmental factors affecting propagation of localized corrosion</i>	45
.....		45
Chapter 3:	Role of passivation in localized CO ₂ corrosion of mild steel	57
3.1	Introduction	57
3.2	Experimental design	63
3.2.1	<i>Setup</i>	63
3.2.2	<i>Procedure</i>	63
3.2.3	<i>Test matrix</i>	66
3.3	Results and discussion	68
3.3.1	<i>Passivation observation from potentiodynamic polarization tests</i>	68
3.3.2	Passivation observation from cyclic polarization tests	76
3.3.3	<i>Spontaneous passivation observations</i>	79
3.3.4	<i>Role of CO₂/FeCO₃ in spontaneous passivation</i>	82
Chapter 4:	Chemistry and structure of the passive film on mild steel in CO ₂ corrosion environments	90
4.1	Introduction	90
4.2	Experimental procedures	92
4.3	Results and discussion	95
4.3.1	<i>Spontaneous passivation</i>	95
4.3.2	<i>XRD and GIXRD analysis results</i>	97
4.3.3	<i>TEM/EDX analysis results</i>	101
4.4.	Passivation scenario for mild steel in CO ₂ environments	107

Chapter 5: Mesh-capped probe design for direct pH measurements at an actively corroding metal surface.....	108
5.1 Introduction.....	108
5.1.1 Indirect surface pH measurement probe design	109
5.1.2 <i>Direct surface pH measurement probe design</i>	109
5.2 Experimental	111
5.2.1 <i>Experimental design and setup</i>	111
5.2.2 <i>Experimental test matrix and procedure</i>	115
5.3 Results and discussion	116
5.3.1 <i>Validity and reproducibility of measurement using the surface pH probe</i>	117
5.3.2 <i>Chemical buffer effect on surface pH</i>	120
5.3.3 <i>Temperature effect on surface pH</i>	121
5.3.4 <i>Effect of deposit layer porosity on surface pH</i>	122
5.3.5 <i>Surface pH measurement at different bulk pH values</i>	124
Chapter 6: Modeling localized CO ₂ corrosion on mild steel	125
6.1 Introduction.....	125
6.2 Localized CO ₂ corrosion mechanism.....	126
6.3 Localized CO ₂ corrosion mechanistic model description.....	127
6.3.1 <i>Water chemistry model</i>	128
6.3.2 <i>Electrochemistry model</i>	128
6.4 Experimental validation of the model.....	141

	10
Chapter 7: Conclusions and future work suggestions.....	148
7.1 Conclusions.....	148
7.2 Future research suggestions	149
7.3 Future development concepts: “super artificial pit” design.....	150
References.....	151

List of Tables

Table 1. Chemical composition (weight percent) of C1008 for anode and cathode.....	35
Table 2. Artificial pit test matrix.....	36
Table 3. Chemical reactions for the CO ₂ aqueous environment ^[20, 23]	46
Table 4. Values of the equilibrium constants for the reactions listed in Table 3 ^[20, 23] ...	47
Table 5. The chemical composition (weight percent) for C1018 carbon steel.	65
Table 6. The chemical composition (weight percent) for X65 carbon steel.....	65
Table 7. Potentiodynamic sweep polarization test matrix	66
Table 8. spontaneous polarization tests matrix	67
Table 9. Cyclic polarization test matrix.....	67
Table 10. Test matrix for the passivation experiments	93
Table 11. Surface pH measurement methods.	109
Table 12. Mild steel mesh data.	112
Table 13. Test matrix for the surface pH experiments.....	115
Table 14. Surface pH measurement during mild steel mesh corroding in a CO ₂ saturated solution, with and without deposit layers.	124
Table 15. Comparison compilation of the experimental data and model predictions ...	147

List of Figures

Figure 1. Section of a corroded pipe showing localized attack. Image source ConocoPhillips, with permission.	27
Figure 2. (a) fully assembled artificial pit, (b) cutaway side view, (c) enlarged bottom view of cathode; center hole for anode, (d) detailed cross section view.	31
Figure 3. Glass cell arrangement for the artificial pit test cell.	34
Figure 4. Corrosion rate and open circuit potential (OCP) with time for a typical protective FeCO_3 layer formation process on the cathode during an AP test at $T=80^\circ\text{C}$, pH 6.6, $[\text{NaCl}]=1 \text{ wt}\%$, $P_{\text{CO}_2}=0.53 \text{ bar}$, $[\text{Fe}^{2+}]_{\text{initial}}=50 \text{ ppm}$, stagnant.	37
Figure 5. Disconnected open circuit potentials (OCP) of anode and cathode and coupled (mixed) potential with time at $T=80 \text{ }^\circ\text{C}$, $p\text{CO}_2=0.53\text{bar}$, pH 5.9-6.1, $\text{SS}_{\text{FeCO}_3}=0.3-0.9$, $[\text{NaCl}] = 1 \text{ wt}\%$, shallow pit, stagnant.	38
Figure 6. Galvanic current density calculated with respect to anode (line) and open circuit potential (OCP) difference between anode and cathode (points) with time at pH 5.9, $T=80^\circ\text{C}$, $\text{SS}_{\text{FeCO}_3}=0.8-4$, shallow pit, $[\text{NaCl}]=1\text{wt } \%$, mildly agitated solution by a magnetic stirring bar at 500 rpm.	40
Figure 7. Galvanic current density calculated with respect to anode (line) and open circuit potential (OCP) difference between anode and cathode (points) with time when solution is in the <i>grey zone</i> , i.e $\text{SS}_{\text{FeCO}_3}=0.3-0.9$, at $T=80 \text{ }^\circ\text{C}$, $p\text{CO}_2=0.53\text{bar}$, pH 5.9-6.1, $[\text{NaCl}] = 1 \text{ wt}\%$, stagnant, shallow pit.	42
Figure 8. Uniform corrosion rates for an uncoupled FeCO_3 covered cathode and a bare steel anode vs. the localized corrosion rate seen on a coupled anode at the beginning and	

end of the artificial pit test conducted in the <i>grey zone</i> : $SS_{FeCO_3}=0.3-0.9$, at $T=80\text{ }^\circ\text{C}$, $pCO_2=0.53\text{bar}$, $pH\ 5.9-6.1$, $[NaCl]=1\ \text{wt}\%$, shallow pit, stagnant.	43
Figure 9. Galvanic current density calculated with respect to the anode (line) and OCP difference between anode and cathode (points) with time when solution is not in the <i>grey zone</i> , i.e the solution is supersaturated: $SS_{FeCO_3}=3-9$, at $T=80\text{ }^\circ\text{C}$, $pCO_2=0.53\text{bar}$, $pH\ 5.6$, $[NaCl]=1\text{wt}\%$, stagnant.	44
Figure 10. Galvanic current density calculated with respect to the anode (line) and OCP difference between anode and cathode (points) with time when solution is not in the <i>grey zone</i> , i.e the solution is undersaturated: $SS_{FeCO_3}=0.2-0.5$, at $T=80\text{ }^\circ\text{C}$, $pCO_2=0.53\text{bar}$, $pH\ 5.8$, $[NaCl]=1\text{wt}\%$, solution is mildly stirred by a magnetic bar at 100 rpm.	45
Figure 11. Calculated pH effect on solubility of $FeCO_3$ and the “grey zone” at $T=80^\circ\text{C}$, $pCO_2=0.53\text{bar}$, $[NaCl]=1\ \text{wt}\%$	49
Figure 12. Galvanic current density calculated with respect to the anode with time for different pH at $T=80^\circ\text{C}$, $pCO_2=0.53\text{bar}$, $SS_{FeCO_3}\approx 0.5-4$, shallow pit, $[NaCl]=1\ \text{wt}\%$, stagnant.	50
Figure 13. Calculated effect of CO_2 partial pressure on solubility of $FeCO_3$ and the “grey zone” at $T=80\text{ }^\circ\text{C}$, $pH\ 6.0$, $[NaCl]=1\text{wt}\%$	51
Figure 14. Salt effect on the “grey zone” width at $T=80\text{ }^\circ\text{C}$, $pCO_2=0.53\ \text{bar}$, $pH\ 6.0$	53
Figure 15. Galvanic current density calculated with respect to the anode for different NaCl concentrations at $pH\ 5.9-6.0$, $T=80^\circ\text{C}$, shallow pit, $SS_{FeCO_3}=0.2-4$, $\omega=400\text{rpm}$. ..	54

Figure 16. Galvanic current density calculated with respect to the anode for a stagnant and stirred solution using a rotating magnet at pH 5.8-5.9, $SS_{FeCO_3}=0.3-4$, $T=80^\circ C$, shallow pit, $[NaCl]=1wt\%$	55
Figure 17. Galvanic current density calculated with respect to the anode for a receded pit (depth=2 mm) and shallow pit (depth<0.1 mm) at pH 5.8–5.9, $T=80^\circ C$, $SS_{FeCO_3}=0.2-4$ $[NaCl] =1\%wt$	56
Figure 18 Scenario #1: Open circuit potential decreases for film covered surface where cathodic reaction is mass transfer controlling due to diffusion barrier.....	58
Figure 19. Scenario #2: Open circuit potential remains constant for filmed and bare steel surfaces where both the anodic and cathodic reactions are similarly reduced due to film formation.....	59
Figure 20. Scenario #3: Decrease in the open circuit potential due to the scale reducing the cathodic reactions more than the anodic reaction.	60
Figure 21. Scenario #4: Increase in the open circuit potential due to the scale reducing the anodic reaction more than the cathodic reactions.	61
Figure 22. Scenario #5: Open circuit potential increases for passivated surface compared with bare surface.	62
Figure 23. Three electrode electrochemical glass cell ^[18]	64
Figure 24. Potentiodynamic polarization sweep curves starting from the open circuit potential on active surfaces at $[NaCl] =1\%wt$, $T=80^\circ C$, $pCO_2=0.53$ bar, stagnant flow. 69	

Figure 25. Potentiodynamic polarization sweep curves starting from the open circuit potential on active surfaces at $[\text{NaCl}] = 10\% \text{wt}$, $T=80^\circ\text{C}$, $p\text{CO}_2=0.53$ bar, stagnant flow.	69
Figure 26. Potentiodynamic polarization sweep curves starting from open circuit potential on active surfaces at $[\text{NaCl}] = 1\% \text{wt}$, $T=80^\circ\text{C}$, $p\text{CO}_2=0.53$ bar, stagnant flow condition.	70
Figure 27. Potentiodynamic polarization sweep curves starting from open circuit potential on active surfaces at pH 7, $T=80^\circ\text{C}$, $p\text{CO}_2=0.53$ bar, stagnant flow condition.	71
Figure 28. Potentiodynamic polarization sweep curves starting from open circuit potential on active surfaces at pH 7, $T=80^\circ\text{C}$, $p\text{CO}_2=0.53$ bar, stagnant flow condition.	72
Figure 29. Potentiodynamic polarization sweep curves starting from open circuit potential on active surfaces at pH 8, $T=80^\circ\text{C}$, $p\text{CO}_2=0.53$ bar, stagnant flow condition.	73
Figure 30. Comparison of potentiodynamic polarization sweep curves starting from open circuit potential on active and scaled surfaces at pH 7, $T=80^\circ\text{C}$, $p\text{CO}_2=0.53$ bar, stagnant flow condition.	74
Figure 31. Potential change during the film formation at $\text{pH} \approx 8.0$, $T=80^\circ\text{C}$, $P_{\text{CO}_2}=0.53$ bar, stagnant flow condition.	75
Figure 32. Comparison of potentiodynamic polarization sweep curves starting from open circuit potential on active and filmed surfaces at pH 8, $T=80^\circ\text{C}$, $p\text{CO}_2=0.53$ bar, stagnant flow condition.	76
Figure 33. Cyclic polarization curve of mild steel at different scan rate in CO_2 purged NaHCO_3 solution under $T=80^\circ\text{C}$, pH 8.	77

Figure 34. Cyclic polarization curve of mild steel at different polarization rate in deaerated NaOH solution under $T=80^{\circ}\text{C}$, pH 8.....	78
Figure 35. The open circuit potential during spontaneous passivation is affected by pH at $T=80^{\circ}\text{C}$, $P_{\text{CO}_2}=0.53$ bar, NaCl=1 wt%, stagnant flow condition.	80
Figure 36. Temperature effect on the open circuit potential during spontaneous passivation at pH 7.5, $P_{\text{CO}_2}=0.53$ bar, NaCl=1 wt%, stagnant flow condition	81
Figure 37. Open circuit potential vs. time for mild steel in NaOH system under $T=80^{\circ}\text{C}$, pH8, $P_{\text{N}_2}=0.45$ bar, $P_{\text{CO}_2}=0.07$ bar compared with CO_2 purged solution.....	82
Figure 38. Open circuit potential vs. time of mild steel in NaOH system at pH8, $P_{\text{N}_2}=0.52$ bar, applied anodic current density= 6 A/m^2 ^[57] compared with CO_2 purged solution.....	83
Figure 39. Open circuit potential vs. time for mild steel in NaOH system at pH 9.5, $P_{\text{N}_2}=0.52$ bar compared with CO_2 purged solution.....	84
Figure 40. Case1: The spontaneous passivation (at initial pH 7.8, $T=80^{\circ}\text{C}$, $P_{\text{CO}_2}=0.53$ bar, [NaCl] =1%wt, stagnant solution) and depassivation by decreasing pH from pH 7.8 to pH 5.4.....	85
Figure 41. Case 1: relation between supersaturation of FeCO_3 and depassivation at $T=80^{\circ}\text{C}$, $P_{\text{CO}_2}=0.53$ bar, [NaCl] =1 wt%, stirring speed 300rpm.	86
Figure 42. Case 2: relation between supersaturation of FeCO_3 and initiation point of passivation at $T=80^{\circ}\text{C}$, $P_{\text{CO}_2}=0.53$ bar, [NaCl] =1%wt, stirring speed 300rpm.	87
Figure 43. Case3: relation between supersaturation of FeCO_3 , corrosion potential, and depassivation at $T=80^{\circ}\text{C}$, $P_{\text{CO}_2}=0.53$ bar, [NaCl] =1%wt, mildly stirred.	88

Figure 44. A crystal slice was cut from the bulk surface by FIB.....	95
Figure 45. Open circuit potential history for spontaneous passivation.....	96
Figure 46. Open circuit potential history during initial FeCO ₃ formation before passivation.....	96
Figure 47. XRD and SEM of non-passivated steel surface after 2.7 hours immersion. ..	97
Figure 48. XRD and SEM of passivated steel surface after 65 hours immersion.	98
Figure 49. GIXRD and SEM of non-passivated steel surface after 2.7 hours immersion.	99
Figure 50. GIXRD and SEM of passivated metal surface after 65 hours immersion....	100
Figure 51. HAADF STEM image of a sample with circled surface A and B	101
Figure 52. HAADF STEMEM image of circled area A in Figure 51 with EDX element profile indicated.	102
Figure 53. EDX element profile of different phases for Figure 52. Note: unknown element determined to be iron carbide (Fe ₃ C).	103
Figure 54. The TEM image of edge surface of area B in Figure 51 with designated areas C , D and E for analysis.....	104
Figure 55. Alloyed element Mn is observed by EDX on area C in Figure 54.....	105
Figure 56. Element profile at different phases for area D in Figure 54. EDX directional scan indicated in TEM image.	106
Figure 57. Element profile at different phases for Area E in Figure 54. EDX directional scan indicated in TEM image.	106

Figure 58. A Pourbaix diagram showing an increase of pH and consequently potential beneath a FeCO_3 scale leading to passivation.....	107
Figure 59. Surface pH probe design.	112
Figure 60. SEM images of (a) single sheet mesh, (b) double sheet compressed mesh.	113
Figure 61. The images of particles used to create the deposit (a) typical sand particle (size: 100–500 μm), (b) glass bead particles (size: 50–80 μm).	113
Figure 62. Surface pH measurement setup deployed in a standard three-electrode electrochemical glass cell	114
Figure 63. Two series of surface pH measurements during mild steel mesh corrosion in a CO_2 purged solution at bulk pH 4.0, $T=25^\circ\text{C}$, $p_{\text{total}}=1\text{bar}$, $P_{\text{CO}_2}=0.97\text{ bar}$, $[\text{NaCl}] = 1\text{wt}\%$	118
Figure 64. Surface pH measurements during mild steel mesh corrosion in a CO_2 purged solution at bulk pH 6.0, $T=25^\circ\text{C}$, $p_{\text{total}}=1\text{bar}$, $P_{\text{CO}_2}=0.97\text{ bar}$, $[\text{NaCl}] = 1\text{wt}\%$	118
Figure 65. The surface pH measurement comparison between a single sheet mild steel mesh and a double sheet compressed mild steel mesh at bulk pH 6.0, $T=25^\circ\text{C}$, $p_{\text{total}}=1\text{bar}$, $p_{\text{CO}_2}=0.97\text{bar}$, $[\text{NaCl}]=1\text{wt}\%$	119
Figure 66. Surface pH during mild steel mesh corrosion in an aqueous solution purged with CO_2 or N_2 at bulk pH 4.0, $T=25^\circ\text{C}$, $p_{\text{total}}=1\text{bar}$, $P_{\text{CO}_2/\text{N}_2}=0.97\text{ bar}$, $[\text{NaCl}] = 1\text{wt}\%$	120
Figure 67. Surface pH comparison during a mild steel mesh corrosion, between 25°C and 80°C in a solution saturated with CO_2 under bulk pH 4.0, $p_{\text{total}}=1\text{bar}$, $p_{\text{CO}_2}=0.97\text{bar}$ (at 25°C), $p_{\text{CO}_2}=0.53\text{bar}$ (at 80°C), $[\text{NaCl}] = 1\text{wt}\%$	121

Figure 68. Surface pH measurement during mild steel mesh corrosion under a glass bead deposit layer 5mm in depth at different temperatures under bulk pH 4.0, 5.0, 6.0 and 6.6, $p_{\text{CO}_2}=0.97$ bar (at 25 °C) or $p_{\text{CO}_2}=0.53$ bar (at 80 °C) [NaCl]=1wt%.	122
Figure 69. Surface pH measurement for a bare mild steel mesh and one under 5mm depth deposit, corroding at bulk pH 4.0, 5.0, 6.0, 6.6, $T=25^\circ\text{C}$, $p_{\text{CO}_2}=1$ bar, [NaCl]=1wt%.	123
Figure 70. Surface pH measurement for a bare mild steel mesh and one under 5mm deposit, corroding at bulk pH 4.0, 5.0, 6.0, 6.6, $T=80^\circ\text{C}$, $p_{\text{CO}_2}=0.53$ bar, [NaCl]=1wt%.	123
Figure 71. The mechanism for “mesa” type localized CO_2 corrosion on mild steel	127
Figure 72. Schematic representation of active corrosion on the bare anode surface (pit bottom).....	129
Figure 73. Schematic representation of passive corrosion on the cathode (iron carbonate covered steel surface around the pit).	137
Figure 74. Spontaneous passivation current density as a function of pH at $T=80^\circ\text{C}$, $P_{\text{CO}_2}=0.53$ bar, $P_{\text{total}}=0.53$ bar, NaCl=1 wt. %.....	138
Figure 75. Factor f at $T=80^\circ\text{C}$, $P_{\text{CO}_2}=0.53$ bar, $P_{\text{total}}=1$ bar, NaCl=1 wt. %.....	139
Figure 76. Scheme for galvanic cell established between bare anode and passive cathode	140
Figure 77. Model prediction matches an example of experimental polarization curves on a bare steel surface at $T=80^\circ\text{C}$, pH 7.0, $P_{\text{CO}_2}=0.53$ bar, $P_{\text{total}}=1$ bar, NaCl=1 wt. %.....	141

Figure 78. Open circuit potential change for the case of spontaneous passivation at T=80 °C, pH 7.8, NaCl=1 wt. %, P _{CO2} =0.53 bar, P _{total} =1 bar, Fe ²⁺ _{initial} = 0 ppm.....	142
Figure 79. Comparison of model prediction and an experimental polarization curve on a passive steel surface at T=80 °C, pH 7.8, P _{CO2} =0.53 bar, P _{total} =1 bar, NaCl=1 wt. %... ..	143
Figure 80. Comparison of a spontaneous passivation potential between the model and experimental data at T=80 °C, NaCl=1 wt. %, P _{CO2} =0.53bar, P _{total} =1bar, Fe ²⁺ _{initial} = 0 ppm.	143
Figure 81. Open circuit potential (OCP) profile for spontaneous passivation on the cathode at T=80 °C, pH 6.6, NaCl=1 wt %, P _{CO2} =0.53 bar, P _{total} =1 bar, Fe ²⁺ _{initial} = 0 ppm.	144
Figure 82. Galvanic current density with respect to anode and coupled potential profiles after the anode and cathode were connected during artificial pit test at T=80 °C, pH 6.6, NaCl=1 wt. %, P _{CO2} =0.53 bar, P _{total} =1 bar, Fe ²⁺ _{initial} = 0 ppm, area ratio=350.....	145
Figure 83. Galvanic current density with respect to the anode comparison between model prediction and experimental data at T=80 °C, pH 6.6, NaCl=1 wt. %, P _{CO2} =0.53 bar, P _{total} =1 bar, Fe ²⁺ _{initial} = 0 ppm, area ratio=350.....	146
Figure 84. Localized corrosion acceleration factor comparison between model and experimental data at T=80 °C, pH 6.6, NaCl=1 wt. %, P _{CO2} =0.53 bar, P _{total} =1 bar, Fe ²⁺ _{initial} = 0 ppm, area ratio=350.....	147
Figure 85. Scheme for super artificial pit design.....	150

Chapter 1: Introduction

1.1 Literature review

Corrosion problems have a major impact on US economy. A survey released in 2002 by the US Department of Transportation showed costs as high as \$276 billion per year. Annual direct costs were \$1.4 billion for corrosion related to oil/gas exploration/production and a further \$5.0 billion for gas distribution ^[1]. Corrosion has received much attention from both industry and academia ^[2-59]. The most important form of corrosion in the oil and gas industry is the so called CO₂ corrosion.

1.1.1 CO₂ corrosion

The mechanism of general CO₂ corrosion, by carbonic acid direct reduction, was first published by C. de Waard ^[2, 3]. Pioneering research explicitly studied and discussed this mechanism for fresh metal surface including the effect of environmental parameters ^[4-11], metallurgical factors ^[7], CO₂ hydration reaction ^[8], anodic and cathodic reactions ^[2-5], rate controlling step ^[11], flow effect ^[12, 13], and other corrosive species including oxygen ^[14], H₂S ^[15] and organic acid ^[16, 17]. The electrochemical reaction kinetic parameters, such as exchange current density, standard potential, activation energy and Tafel slopes were published ^[2-27]. The modeling for CO₂ corrosion varied from completely empirical models ^[2, 3], semi-mechanistic models ^[11, 12] to purely mechanistic models ^[10, 25]. Increasingly, efforts have been expended on furthering the more mechanistic modeling.

CO₂ corrosion under scaling conditions can be complex ^[19-27]. The role of the corrosion product layer/film has long been debated. The corrosion film, iron carbonate

for an example, not only serves as a mass transfer barrier, but also has a “covering effect”. Corrosion reaction rate is reduced as more active sites are covered by the film [20–27]. A criterion for protectiveness of iron carbonate film was suggested by B.F.M. Pots using the term of scaling tendency [19]. This was defined as the ratio of iron carbonate precipitation rate and steel corrosion rate. If the scaling tendency (ST) is much smaller ($ST \ll 1$), corrosion under film is dominant. The film formed under this condition is porous and non-protective, and vice versa. The morphology and structure of the films and their impacts on corrosion remain an open topic of research in sweet (CO_2) as well as sour (H_2S) conditions.

1.1.2 Localized CO_2 corrosion on mild steel

Failure caused by localized CO_2 corrosion is a problem for the oil and gas industry. It has been studied by several researchers in the past in order to clarify the influential factors involved [30–59]. Several mechanisms were proposed to explain localized CO_2 corrosion.

Flow induced localized corrosion (FILC) mechanism was reported by G. Schmitt [39–46]. According to Schmitt, micro-turbulence can be created by a fracture of the iron carbonate film. Apparently, the intensity of the turbulence can be strong enough to damage the film, and even further erode the substrate metal. This mechanism strives to explain localized corrosion under violent flow conditions.

Z. Xia [48] proposed that a porous iron carbonate film could be formed under scaling conditions. A galvanic cell was possibly established between the steel surfaces with and without attached iron carbonate. Xia also formed iron carbonate film to

simulate surface with attached film under artificially created local high surface pH through cathodic potential polarization. This filmed surface was then connected with a freshly cleaned specimen to establish a galvanic cell. The test results showed that the galvanic current decreased from a certain value to almost 0 A/m^2 after a short period of time (*ca.* 3 hours). This observation explained some characteristics of localized corrosion related to the galvanic cell. The key information was missing on why the potential on surfaces with or without film were different and why the galvanic current decreased to zero instead of maintaining a steady level, or in other words, why the pitting corrosion did not steadily propagate.

Crolet ^[49] proposed another possibility for localized corrosion under CO_2 environments. The difference in species concentration and/or material properties due to heat treatment, replacement or welding was considered to be reasons for setting up a galvanic cell.

A. Dugstad and R. Nyborg ^[50-53] investigated the effects of chromium concentration, temperature and flow rate on “mesa” type localized corrosion. A video recording technique was employed to monitor “mesa” growth. Based on the experimental results, an initiation and propagation model was proposed which indicated that several pits could initiate underneath the iron carbonate film. The pits grew and merged with neighbors to form a “mesa” feature. It was postulated that the bare surface in the pit and the film covered surrounding surface could establish a galvanic cell. Apparently the localized corrosion propagation could be explained under this assumption.

There were no direct measurements to support this hypothesis. This limitation is common for all previous research on the galvanic effect on localized corrosion.

A so called “gray/grey” zone criterion was first proposed by Y. Sun^[55] based on loop experiments. The “gray zone” is a condition near to saturation point with respect to iron carbonate and scaling tendency around 1, condition leading to a formation of a partially protective film. Localized corrosion was highly likely in this grey zone according to the authors.

From the valid literature, no systematic research was found to explain the onset and propagation of localized corrosion. Experimentation and data analysis could explain some observations, whereas other phenomena could not be explained. A systematic study was necessary and is the topic of this dissertation.

1.2 Objectives

To understand localized CO₂ corrosion mechanisms, several fundamental questions have to be answered. Is the galvanic mechanism valid? If the galvanic mechanism is possible, why are different potentials developed to establish a galvanic cell under the same homogeneous bulk solution? What is the role of corrosion scales in localized corrosion? Why does passivation occur during scale formation? What is the role of local water chemistry on passivation? How can localized corrosion propagation be predicted?

To explore these questions on localized corrosion mechanisms, a series of experimental designs, testing procedures and electrochemical measurements were explored and employed. A direct, accurate, robust and reproducible measuring

technique, artificial pit, was developed to characterize localized corrosion. The purpose of this was the elucidation of the localized corrosion galvanic mechanism. Traditional electrochemical techniques, LPR (linear polarization resistance), EIS (electrochemical impedance spectroscopy), cyclic polarization and potentiodynamic polarization, were employed to study the electrochemical characteristics of passivation, relating to localized corrosion. In order to understand the passivation mechanism of mild steel in acidic CO₂ environments, a surface pH probe was developed. Surface analysis techniques were carried out to define the nature of the passive films and define its relationship to localized corrosion using scanning electron microscopy (SEM), energy dispersive X-ray analysis (EDX), X-ray diffraction with traditional and grazing angle incidence (XRD and GIXRD, respectively) and transmission electron microscopy (TEM) combining EDX. Finally an electrochemical mechanistic model was built for prediction purposes.

Parts of this dissertation have been published as journal or conference papers in the past few years (see list of references ^[56-61]). Jiabin Han was the principal investigator on the work that was published there and the key co-author on all the published papers. He was the driving force behind the whole effort and takes the largest portion of the credit for the work as well as the publications. The other co-authors have served either as advisors or have helped with specific portions of the work, such as surface analysis, etc.

Chapter 2: Investigation of the galvanic mechanism for localized CO₂ corrosion propagation using artificial pit technique¹

2.1 Introduction

Localized CO₂ corrosion is the most dangerous type of internal corrosion of mild steel pipelines seen in the oil and gas industry. The penetration rate of localized corrosion can be one or more magnitudes higher than that of uniform corrosion. This process has been observed frequently in the field and was widely studied in the past. [30–62]

A number of environmental factors have been associated with onset of localized corrosion of mild steel pipelines. These include: poor corrosion inhibition, local water separation in oil-water flow, differential condensation in wet gas flow, flow disturbances such as weld beads, flanges, the presence of bacteria, solids, organic acids, hydrogen sulfide, etc. However, a comprehensive mechanism of “pure” localized CO₂ corrosion of mild steel, without these complicating factors is still not well defined. The localized corrosion mechanistic scenarios “borrowed” from other mild steel and passive metal pitting studies, which have been invoked repeatedly in the past trying to explain localized CO₂ corrosion, including differential aeration^[28] and pit acidification,^[29] do not apply. Differential aeration cannot be considered for obvious reasons, as most CO₂ systems are oxygen-free. The mechanism of pit acidification does not seem to hold either because of the strong buffering capacity of CO₂ solutions, i.e. pH changes are much more difficult to achieve in this case, particularly the large changes needed to explain the pit acidification theory. Furthermore, pit acidification is usually related to formation of ferric oxides and

¹ This chapter has been published as an NACE conference paper, paper No. 07323 and in Corrosion.

hydroxides which are not seen in CO₂ corrosion due to the absence of oxygen. Indeed, the morphology of localized CO₂ corrosion of mild steel is rather different to the one seen on mild steel in neutral solutions and on passive metals (see Figure 1). It is usually qualified as “mesa attack” – including large recessed areas free of corrosion products which have corroded severely, sharply divided from surrounding protected areas covered with a corrosion product. The name “mesa” is borrowed from well known geological formations.



Figure 1. Section of a corroded pipe showing localized attack. Image source ConocoPhillips, with permission.

Another overlapping term which can be found in literature for this type of attack is: “flow induced localized corrosion” or FILC.^[39-46] The name implies that the type of attack is related to the corrosion product film being locally removed by flow causing the metal to be exposed directly to the corrosive environment. While this is a plausible explanation for localized corrosion *initiation*, it cannot explain the process of localized attack *propagation*. If film removal by flow was the full explanation, localized CO₂ corrosion of mild steel would not be any more severe than that of bare steel corrosion at any given set of conditions – and in reality it is. Furthermore, this type of localized corrosion is observed under very mild flow conditions and even in stagnant solutions^[47], therefore additional explanation is required.

Nyborg and Dugstad^[50-53] reported observations of localized corrosion initiation using an optical imaging technique. According to them, given the right set of conditions (involving specific water chemistry and flow), localized corrosion initiates underneath a corrosion product layer made up predominantly from iron carbonate (FeCO₃). Larger pits form by merging with neighboring pits. The unsupported “covers” of the pits made up from corrosion product layer are removed by flow turbulence, thereby exposing the bare steel to an aggressive environment, leading to localized corrosion propagation. A hypothesis was made about galvanic nature of the localized corrosion propagation process, without any further elaboration.

Actually, the galvanic mechanism was often invoked in connection with localized CO₂ corrosion propagation in the past.^[32-35, 37, 48, 49, 50-53] For example Achour^[37], based on his own observations, arbitrarily assumed a potential difference between the protected

and unprotected areas to be 100 mV. While this is possible, there are no studies which have clearly provided evidence in support of the apparent galvanic mechanism of localized CO₂ corrosion propagation. This is the subject of the present study.

Propagation of localized corrosion is in this study hypothesized to occur when a galvanic cell is established by coupling two distinct areas, a bare steel surface (acting as an anode) and a an FeCO₃ layer covered steel surface (acting as a cathode), in a conductive CO₂ solution. It should be noted that in the present work, the discussion will not be focused on mechanisms leading to localized attack *initiation* since there seems to be consensus that this happens when portions of the protective FeCO₃ film are removed from the steel surface by chemical or mechanical means. The focus is on localized attack *propagation*.

An attempt will be made here to answer two basic questions:

What is the mechanism of the accelerated localized corrosion propagation on mild steel in CO₂ solutions?

Which are the key factors that influence it?

To answer these questions, an artificial pit experimental setup was newly developed, as described below, which was inspired by the previously published “pencil pit”^[63] and “artificial pit”^[64] designs. Marsh, *et al*^[63] and Turnbull *et al*^[64] designed an artificial pit (or “pencil pit” as it was called in the first publication^[63]) to investigate the effect of inhibitors on localized corrosion. In their designs, the anode and cathode were isolated from each other in order to measure galvanic coupling resulting in localized corrosion. The two electrodes were physically separated: in Marsh’s, *et al*^[63] case within

a single cell, while in Turnbull's *et al.*^[64] case - between two glass cells connected with a salt bridge. The latter made it easier to control the separate aqueous environments, but also introduced experimental problems, namely: it is difficult to ensure exactly the same corrosive environment for the anode and cathode when in two different cells. In both studies, the most serious drawback was related to the physical separation distance of the anode and cathode. This gives rise to ohmic resistance in the aqueous phase during any galvanic current measurements. In reality, the anode and the cathode are part of the same steel substrate in very close proximity. This was the first modification that was better accounted for in the new artificial pit design. This new design is referred to below as the "artificial pit" (AP).

2.2 Experimental design

2.2.1 Artificial pit design

The goal of the new artificial pit (AP) technique was to simulate a localized corrosion geometry including open pits (both recessed and shallow) as well as occluded pits, using *in situ* measurements. The design of the new AP is shown in Figure 2, the main features being:

- The cathode is a 16 cm² round flat surface, which is approximately 1000 times larger than the 0.018 cm² anode.
- The cathode and anode are electronically insulated from each other by a thin PVC coating on the anode's outer wall. This prevents short-circuiting by direct contact between anode's outer wall and cathode's inner wall in the solution while keeping them as close as possible.

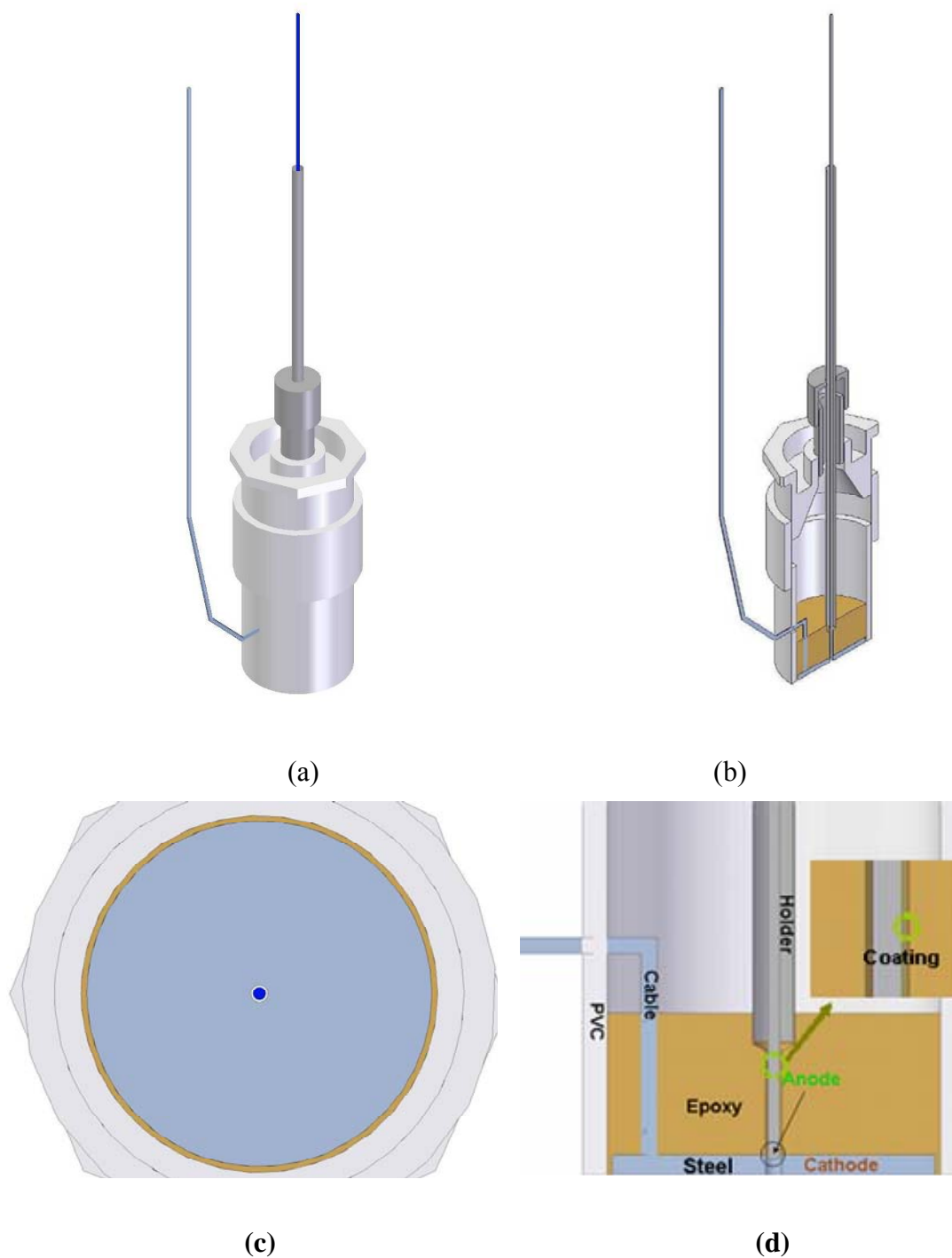


Figure 2. (a) fully assembled artificial pit, (b) cutaway side view, (c) enlarged bottom view of cathode; center hole for anode, (d) detailed cross section view.

- The anode and cathode are externally connected by a zero resistance ammeter (ZRA). This mimics reality where the pit bottom is directly connected to the surrounding steel surface.
- The depth of the anode is adjustable. This allows investigation of pit behavior at different pit depths in different scenarios of pit propagation.
- All parts of the artificial pit are tightly compacted into one unit. The environment for the anode and cathode is similar since they are located in the same glass cell.

As shown in the design of the artificial pit, the coupling current (galvanic current) and the mixed potential (galvanic potential) can be monitored while the anode and cathode are connected externally via a ZRA. The electrochemical characteristics for the disconnected anode and cathode can also be measured by available techniques including linear polarization resistance (LPR), electrochemical impedance spectroscopy (EIS), *etc.*

2.2.2 Corrosion cell setup

The overall AP glass cell test setup is depicted in Figure 3. A classical three-electrode electrochemical arrangement is used including mild steel working electrodes (C1008 was used for both the anode and cathode), platinum wire counter electrode and an external saturated Ag/AgCl reference electrode connected with the cell by using a Luggin capillary and a KCl salt bridge.

2.2.3 Experimental procedure

Two steel surfaces, serving as cathode and anode, were polished using a 200, 400 and 600 grit sand paper in sequence. Each was wetted with 2-propanol to prevent the surface from overheating during polishing. Specimen surfaces were ultrasonicated in 2-

propanol solvent to remove polishing debris, and then dried with a cool air blow. The cathode was placed in an empty glass cell under a dry CO₂ gas environment, while the anode was preserved in a desiccator.

An aqueous NaCl solution was first deaerated with CO₂ and heated to 80°C in another auxiliary glass cell. The pH was adjusted to 6.6 by adding a deaerated 1M NaHCO₃ solution. CO₂ purging continued an additional half hour after the addition of NaHCO₃ solution to ensure best possible deaeration of the solution.

After the solution was prepared in the auxiliary glass cell, the cathode was then submerged in the electrolyte by pumping the prepared solution across. A deaerated dilute FeCl₂ solution was injected into the solution to achieve a high ferrous ion (Fe²⁺) concentration and a FeCO₃ supersaturation (SS_{FeCO_3}) of about 300 at the beginning of the experiment (actual concentration of Fe²⁺ was about 50 ppm), which is required for rapid formation of a corrosion product layer. Typically in less than 2 days of corrosion in such an environment, a reproducible protective FeCO₃ film was developed on the cathode, as the bulk Fe²⁺ concentration decreased to 1-2 ppm due to precipitation. Combined LPR and EIS techniques were employed to measure the general corrosion rate during the FeCO₃ layer formation process. When the corrosion rate became stable and was less than 0.1 mm/y, the FeCO₃ layer formation process on the cathode was deemed complete.

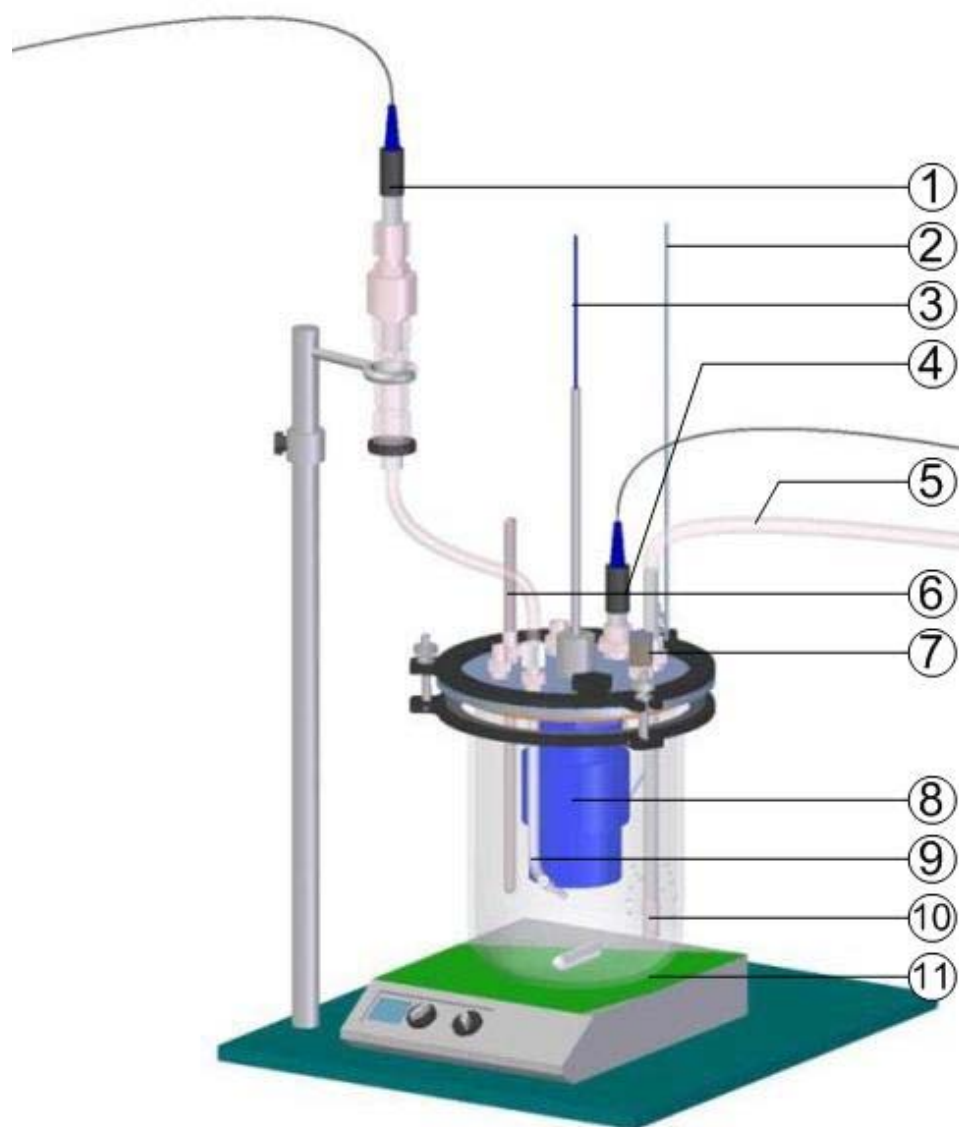


Figure 3. Glass cell arrangement for the artificial pit test cell.

1- Ag/AgCl reference electrode, 2- wire connection to cathode, 3- wire connection to anode, 4- pH probe, 5- gas inflow, 6- thermocouple probe, 7- gas outflow, 8- artificial pit device, 9- Luggin capillary tube, 10- gas dispersion tube, 11- hot plate/stirrer.

Solution conditions were then adjusted for the following AP test. The pH was changed, if needed, by adding a deaerated 1M NaHCO_3 or a dilute 0.01M HCl solution based on the desired water chemistry. After that, the freshly polished anode wire surface

was inserted into the small hole in the center of the cathode. The pit depth was adjusted with respect to the cathode surface by feeding the wire through a compression fitting.

The galvanic current between anode and cathode was recorded using a Gamry® PC4 in a ZRA (zero resistance ammeter) mode. The anode and cathode were disconnected occasionally for a very short period of time (< 1 minute) to measure open circuit potentials and corrosion rates using the LPR technique.

2.2.4 Test matrix

The material used for cathode and anode was mild steel C1008 and its chemical composition is listed in Table 1.

Table 1. Chemical composition (weight percent) of C1008 for anode and cathode

Al	As	C	Co	Cr	Cu	Mn	Mo
0.030	0.004	0.060	0.004	0.033	0.130	0.400	0.017
Nb	Ni	P	S	Sb	Si	Sn	Ta
0.001	0.048	0.010	0.003	0.004	0.039	0.007	0.023
Ti	V	W	Zn	Zr	Fe		
0.004	0.002	0.023	0.003	0.002	Balance		

The test matrix for artificial pit experiments is listed in Table 2. All the tests were carried out at 80 °C. The CO₂ partial pressure for this atmospheric pressure glass cell system was about 0.5 bar at this temperature (the balance being water vapor pressure). The solution was mildly stirred by a magnetic stirring bar to achieve a uniform bulk solution mixing. The pH, FeCO₃ supersaturation, NaCl concentration and stirring speed levels were adjusted to investigate their effects on localized corrosion propagation, as

described below. The simulated pit geometry studied in this work included open shallow and receded pits as well as occluded pits.

Table 2. Artificial pit test matrix

General conditions	Material	C1008
	Temperature	80°C
	Partial pressure of CO ₂	0.53 bar
	Pit depth	<0.1 mm (shallow)
	Area ratio of cathode and anode	1000:1
	NaCl concentration	0.1, 1, 10 wt%
Cathode preparation	Initial pH	6.6
	Initial ferrous iron concentration	50 ppm
	Stirring speed (stir-bar)	0 rpm
	Test period	1–2 days
Artificial pit test	Initial ferrous iron concentration	1–2 ppm
	Adjusted pH	5.8–5.9, 6.6
	SS _{FeCO₃}	0.3–9
	NaCl concentration	0.1, 1, 10 wt%
	Stirring speed (stir-bar)	0, 400–500 rpm
	Pit depth	0 mm, 2mm
	Experiment duration	1–2 days

2.3 Results and discussion

2.3.1 Galvanic mechanism of localized CO₂ corrosion propagation

It was hypothesized above that the galvanic mechanism of localized corrosion propagation in a CO₂ environment is driven by an open circuit potential (OCP) difference between a mild steel surface covered with a protective FeCO₃ layer and a bare steel

surface exposed to the same conditions. Let us see if this scenario is borne out by the measurements.

A typical scaling process, forming protective FeCO_3 on the cathode, is shown in Figure 4.

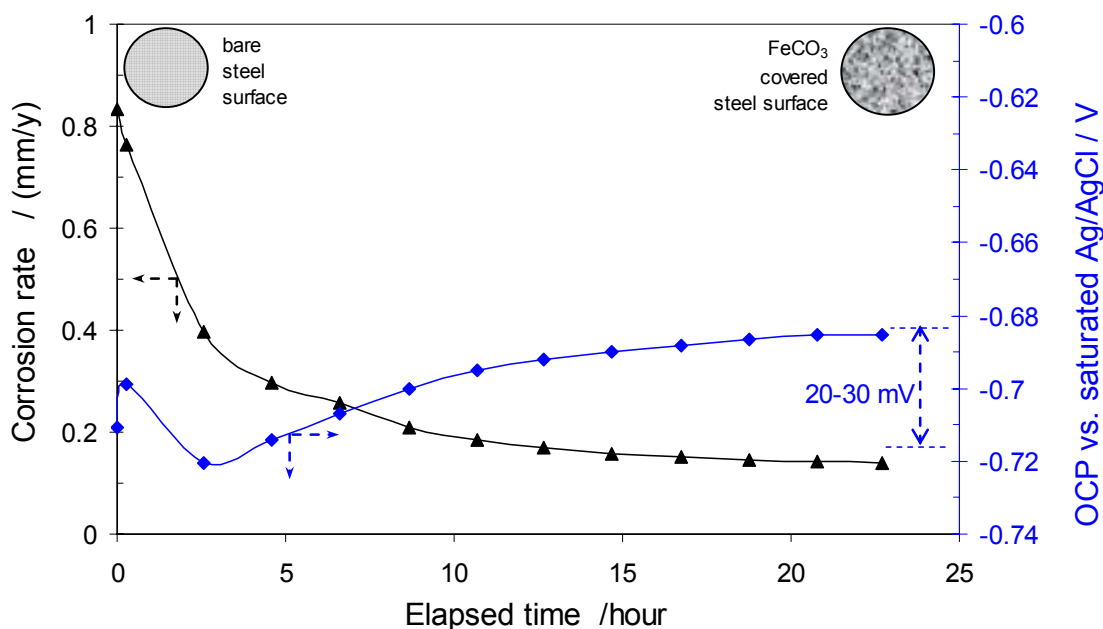


Figure 4. Corrosion rate and open circuit potential (OCP) with time for a typical protective FeCO_3 layer formation process on the cathode during an AP test at $T=80^\circ\text{C}$, $\text{pH } 6.6$, $[\text{NaCl}]=1 \text{ wt}\%$, $P_{\text{CO}_2}=0.53 \text{ bar}$, $[\text{Fe}^{2+}]_{\text{initial}}=50 \text{ ppm}$, stagnant.

During FeCO_3 formation, the general corrosion rate is reduced from the original value of approximately 1 mm/y seen on a fresh bare steel surface to approximately 0.1 mm/y (millimeter per year) on a FeCO_3 covered surface. Simultaneously, the OCP (corrosion potential) initially decreases and then increases. The difference between the open circuit potentials of the FeCO_3 covered surface at the end of the experiment and the

bare steel surface at the beginning of the experiment is typically in the range of 20 to 30 mV under these test conditions. This observation indicates that a galvanic cell may be established between the bare and protected surfaces.

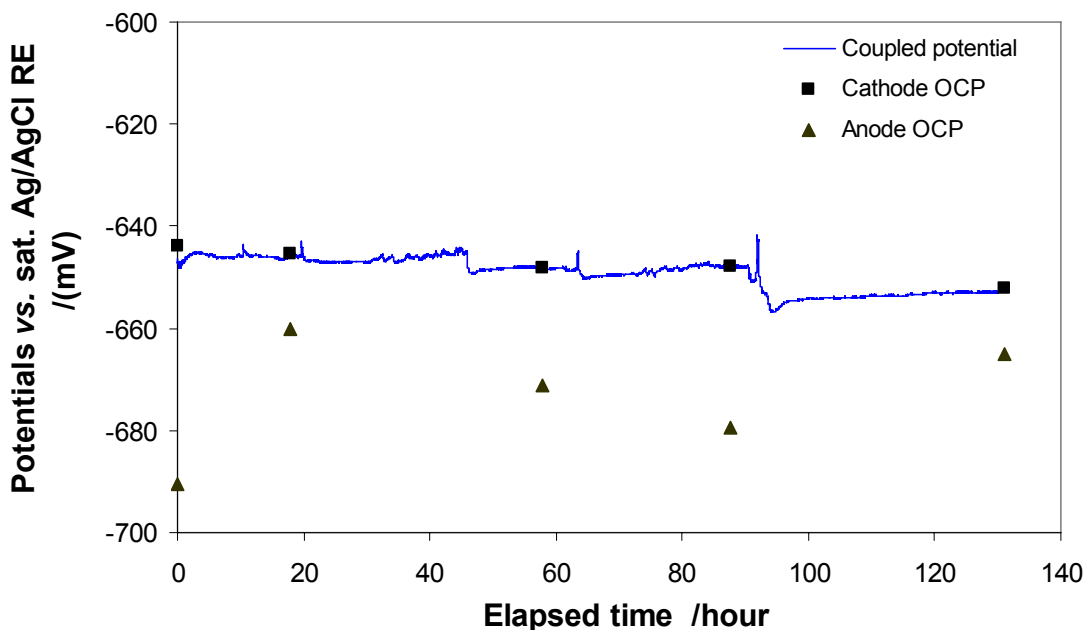


Figure 5. Disconnected open circuit potentials (OCP) of anode and cathode and coupled (mixed) potential with time at $T=80\text{ }^{\circ}\text{C}$, $p\text{CO}_2=0.53\text{bar}$, $\text{pH}5.9\text{-}6.1$, $\text{SS}_{\text{FeCO}_3}=0.3\text{-}0.9$, $[\text{NaCl}]=1\text{ wt}\%$, shallow pit, stagnant.

When a bare steel anode was inserted, and the anode and cathode were connected via a ZRA, the mixed potential was continuously monitored. In the same period the potential difference (galvanic potential) between the anode and cathode was measured by temporarily disconnecting the two. The data obtained (Figure 5) show that when disconnected, the cathode OCP is consistently higher compared to the anode OCP. The coupled or mixed/galvanic potential lies in between, and closer to the cathode potential

due to the much larger surface of the cathode, as would be expected from theory. Therefore it is confirmed that the FeCO_3 covered surface acts as a cathode, and the bare steel surface becomes an anode and a galvanic cell is established between these two surfaces. Since the FeCO_3 covered cathode is much larger, the anode is polarized anodically and this should accelerate its corrosion rate.

It is therefore expected that the OCP difference measured between the anode and cathode drives a significant galvanic current. The coupled/galvanic current measured via a ZRA is shown in Figure 6 along with the OCP difference between the cathode and anode obtained in a disconnected mode. The solid rectangles represent the magnitude of the “driving force” (the OCP difference between disconnected anode and cathode) and the line shows the resulting galvanic current density as a function of time. It is obvious that when the driving force is large (i.e. OCP difference between anode and cathode is high), the galvanic current density is high and vice versa. It should be noted that the current densities shown in Figure 6 are calculated based on the anode surface area. One can conclude that this represents explicit proof for the hypothesis stated above and enables us to generalize that: localized CO_2 corrosion propagates when a stable difference in corrosion potential is established between a larger-area mild steel surface covered by a protective FeCO_3 layer and a smaller-area bare steel surface corresponding to bottom of a pit or a mesa corrosion surface.

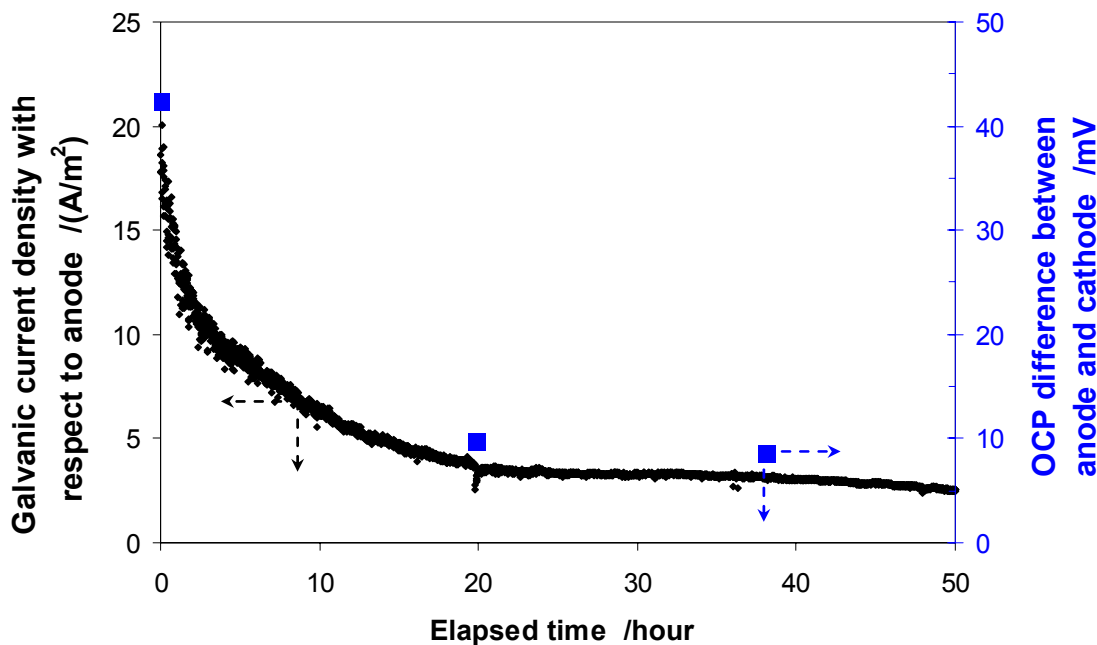


Figure 6. Galvanic current density calculated with respect to anode (line) and open circuit potential (OCP) difference between anode and cathode (points) with time at pH 5.9, $T=80^{\circ}\text{C}$, $SS_{\text{FeCO}_3}=0.8-4$, shallow pit, $[\text{NaCl}]=1\text{wt}\%$, mildly agitated solution by a magnetic stirring bar at 500 rpm.

2.3.2 Conditions required for steady localized CO_2 corrosion propagation

It has been known for a while that while localized corrosion of mild steel in a CO_2 environment initiates and propagates under certain conditions, in other cases it does not. For example Videm and A. Dugstad^[32, 33] observed localized corrosion in turbulent flow only when the solution was nearly or slightly saturated by FeCO_3 . Similar studies were reported by Nyborg^[50, 52] and Nyborg and Dugstad^[53], where they proposed a feasible temperature range being $60-90^{\circ}\text{C}$ for localized corrosion to propagate. Achour^[37] assumed that the pits stopped propagation when they were passivated by FeCO_3 film formation. Sun and Nešić^[54] followed this line of argument and generalized by stating

that only if the corrosion condition fell into the so called “*grey zone*”, the localized corrosion propagated.^[55] The *grey zone* was defined as conditions constituting a solution which is close to saturation for FeCO_3 .

Therefore it is now possible to use the experimental tools and techniques discussed above and explicitly investigate if propagation of localized CO_2 corrosion of mild steel will occur only in the so called *grey zone*. In other words, it is assumed that when the supersaturation with respect to FeCO_3 is high ($\text{SS}_{\text{FeCO}_3} \gg 1$), the FeCO_3 will precipitate on all the surfaces causing any active pits to “heal.” Conversely, if the solution is highly undersaturated ($\text{SS}_{\text{FeCO}_3} \ll 1$), then the FeCO_3 layer on the cathode will dissolve, the driving force for galvanic corrosion will disappear and uniform corrosion will prevail. Consequently only when the solution is near the saturation point with respect to FeCO_3 and is therefore in the *grey zone*, the protective layer will neither dissolve from the cathode nor will it form on the anode and the galvanic cell will operate steadily.

An example of localized corrosion propagation when the solution conditions are in the *grey zone* was already shown in Figure 6 where supersaturation for FeCO_3 varied in the range: $\text{SS}_{\text{FeCO}_3}=0.8-4$. Another example is shown in Figure 7, where it was controlled in a narrower range: $\text{SS}_{\text{FeCO}_3}=0.3-0.9$, i.e. the solution was continuously slightly undersaturated with respect to FeCO_3 . In both cases the galvanic current was very high initially and then stabilized at a lower value as time progressed.

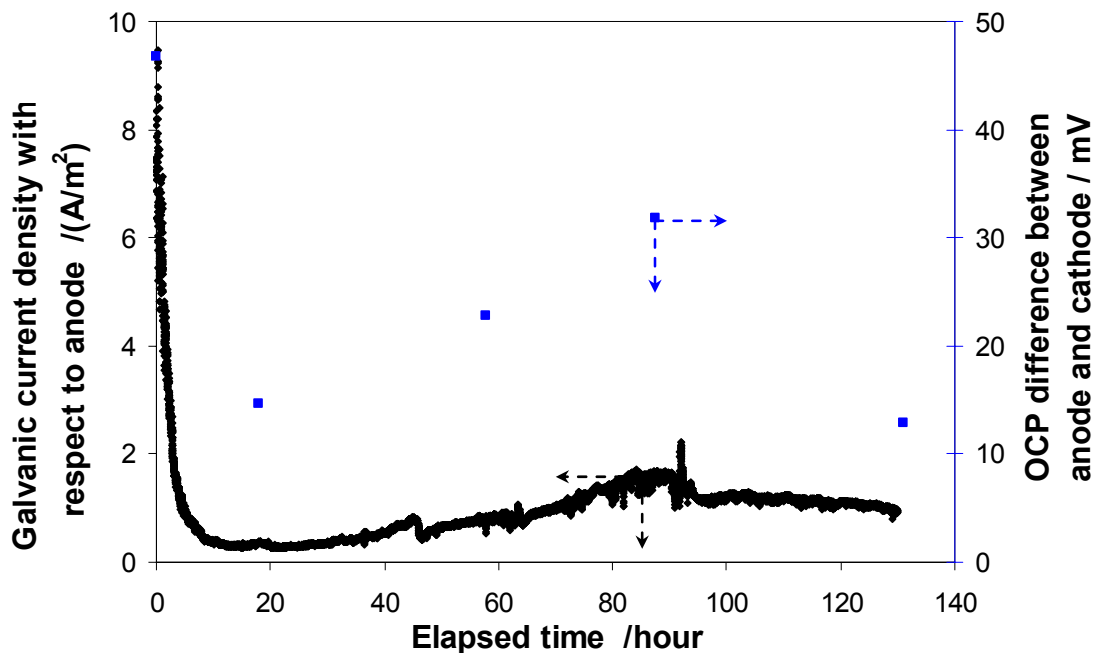


Figure 7. Galvanic current density calculated with respect to anode (line) and open circuit potential (OCP) difference between anode and cathode (points) with time when solution is in the *grey zone*, i.e. $SS_{\text{FeCO}_3}=0.3-0.9$, at $T=80\text{ }^\circ\text{C}$, $p\text{CO}_2=0.53\text{bar}$, $\text{pH } 5.9-6.1$, $[\text{NaCl}]=1\text{ wt\%}$, stagnant, shallow pit.

To put the magnitude of this galvanic current into perspective, it is converted into a corrosion rate and factored into the uncoupled corrosion rates of the anode and cathode. The various corrosion rates of anode and cathode are compared in Figure 8. Clearly, the corrosion rate of the large cathode remains virtually unaffected by the coupling, while the corrosion rate of the coupled anode is doubled.

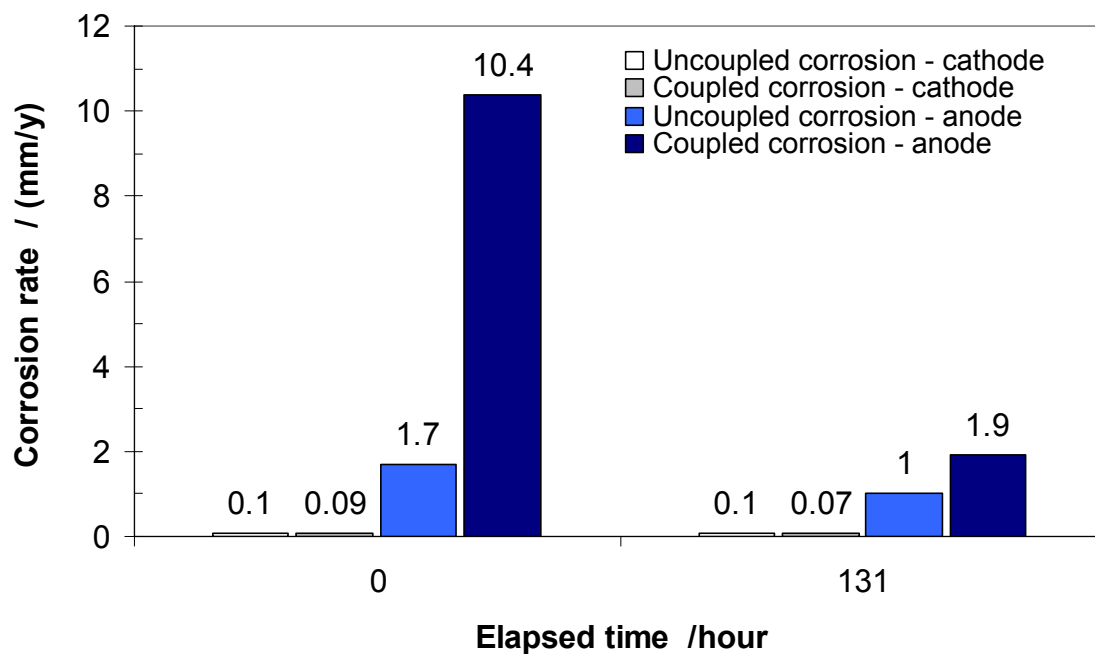


Figure 8. Uniform corrosion rates for an uncoupled FeCO_3 covered cathode and a bare steel anode vs. the localized corrosion rate seen on a coupled anode at the beginning and end of the artificial pit test conducted in the *grey zone*: $\text{SS}_{\text{FeCO}_3}=0.3-0.9$, at $T=80\text{ }^\circ\text{C}$, $p\text{CO}_2=0.53\text{bar}$, $\text{pH } 5.9-6.1$, $[\text{NaCl}]=1\text{ wt\%}$, shallow pit, stagnant.

One situation when the solution is not in the *grey zone* is depicted in Figure 9. In this case the FeCO_3 supersaturation is maintained high ($\text{SS}_{\text{FeCO}_3}=3-9$), and the galvanic current density, which starts very high, is rapidly reduced to zero, indicating that initial propagation of localized corrosion is stifled due to protective FeCO_3 layer formation on the anode. In this case the pit “healed” and the corrosion rates on both cathode and anode equalized and remained low ($<0.1\text{ mm/y}$).

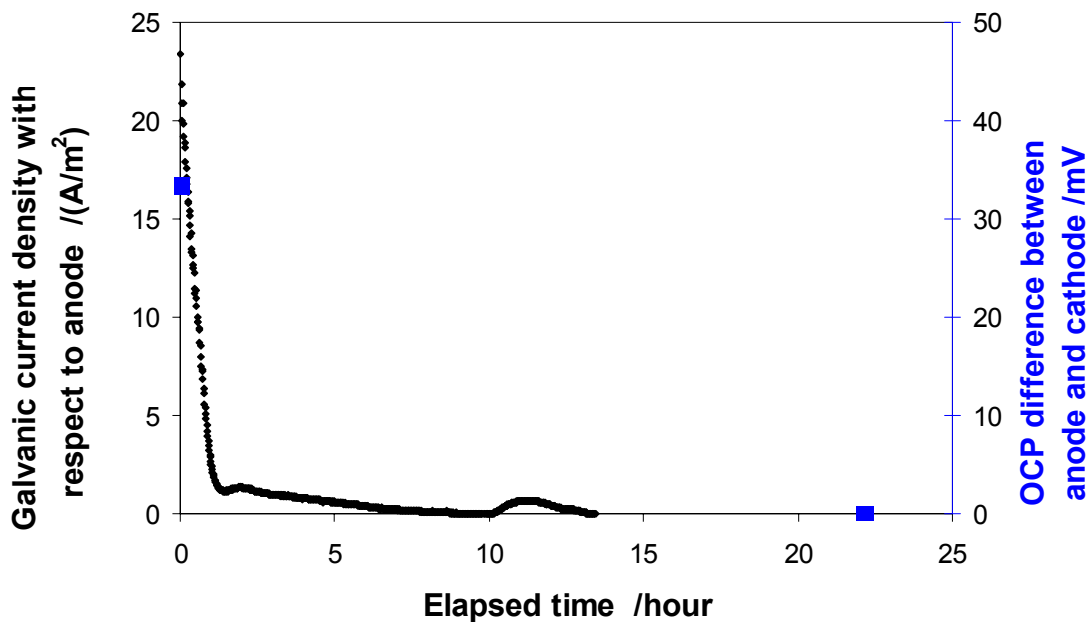


Figure 9. Galvanic current density calculated with respect to the anode (line) and OCP difference between anode and cathode (points) with time when solution is not in the *grey zone*, i.e. the solution is supersaturated: $SS_{\text{FeCO}_3} = 3-9$, at $T=80\text{ }^\circ\text{C}$, $p\text{CO}_2=0.53\text{bar}$, $\text{pH } 5.6$, $[\text{NaCl}] = 1\text{wt}\%$, stagnant.

Another case operating outside the *grey zone* is shown in Figure 10. When FeCO_3 supersaturation is maintained low ($SS_{\text{FeCO}_3}=0.2-0.5$), the galvanic current density also gradually reduces to zero. In this case, it is because the protective FeCO_3 layer on the cathode dissolves (as visually confirmed) and the driving force for the galvanic coupling (potential difference) disappears. Both the anode and the cathode experienced stable high uniform corrosion rates ($>1\text{ mm/y}$).

In summary, it was confirmed that propagation of localized corrosion of mild steel in CO_2 solutions will occur only when the solution is maintained in the *grey zone* i.e. when the conditions are close to saturation with respect to FeCO_3 . Multiple

experiments have shown that this practically translates into a criterion: $SS_{\text{FeCO}_3}=0.5-2$ when no significant FeCO_3 dissolution nor additional precipitation is expected and the galvanic cell is stabilized.

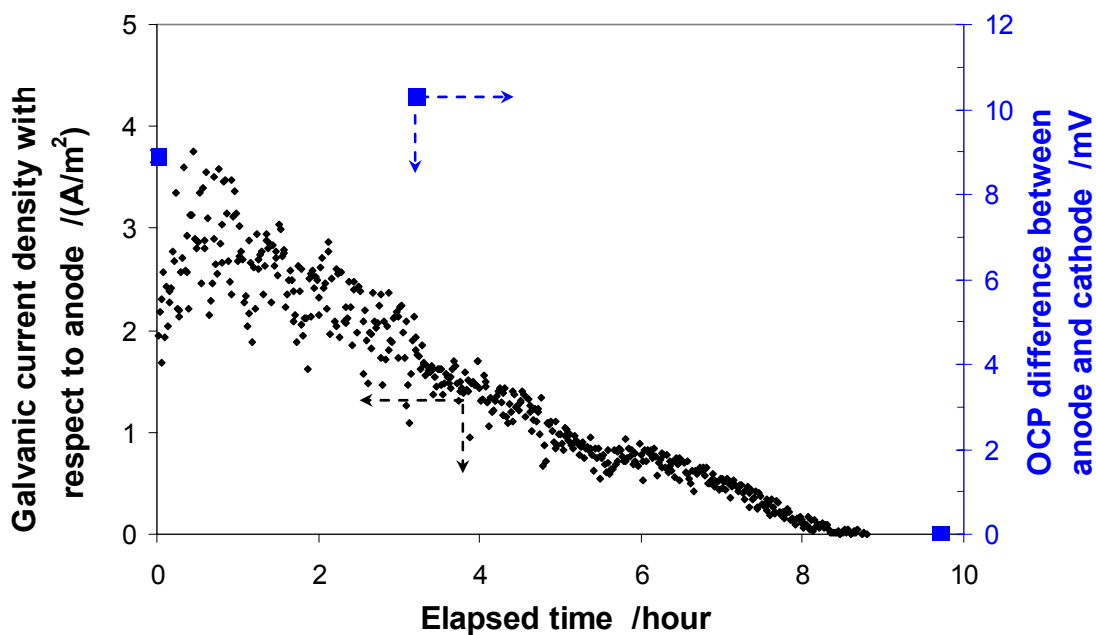


Figure 10. Galvanic current density calculated with respect to the anode (line) and OCP difference between anode and cathode (points) with time when solution is not in the *grey zone*, i.e the solution is undersaturated: $SS_{\text{FeCO}_3}=0.2-0.5$, at $T=80\text{ }^\circ\text{C}$, $p\text{CO}_2=0.53\text{bar}$, $\text{pH} 5.8$, $[\text{NaCl}]=1\text{wt}\%$, solution is mildly stirred by a magnetic bar at 100 rpm.

2.3.3 Environmental factors affecting propagation of localized corrosion

Since FeCO_3 supersaturation (SS_{FeCO_3}) is found to be one of the key factors that determines propagation of localized corrosion when a galvanic cell is established, let us take a closer look at which environmental factors affect it most. SS_{FeCO_3} is defined as the ratio of the concentration product of iron and carbonated ions and the solubility product:

$$SS_{\text{FeCO}_3} = \frac{[\text{Fe}^{2+}][\text{CO}_3^{2-}]}{K_{sp}}$$

where $[\text{Fe}^{2+}]$ is the actual concentration of iron ion, $[\text{CO}_3^{2-}]$ is the actual concentration of the carbonate ion, and K_{sp} is the solubility product for FeCO_3 . To put it simply, the SS_{FeCO_3} expresses the degree of departure from thermodynamic equilibrium for FeCO_3 .

Ferrous ion, Fe^{2+} , is a product of iron dissolution i.e. corrosion and its concentration $[\text{Fe}^{2+}]$ can readily be measured. The carbonate ion, CO_3^{2-} , is assumed to be in equilibrium with the other carbonic species in solution i.e. one can write $[\text{CO}_3^{2-}] = c_{\text{CO}_3^{2-}}$ where $c_{\text{CO}_3^{2-}}$ is the equilibrium concentration. It is influenced by the amount of dissolved CO_2 and pH and can be readily calculated from simple water chemistry models. [20, 23] The pertinent chemical reactions and their equilibrium constants are here briefly reproduced in Table 3 and Table 4 for the convenience of reader, where K represents the equilibrium constant for a given reaction and c the equilibrium concentration of a given species.

Table 3. Chemical reactions for the CO_2 aqueous environment [20, 23]

	Reaction	Equilibrium constant
Carbon dioxide dissolution	$\text{CO}_{2(g)} \xrightleftharpoons{K_{sol}} \text{CO}_2$	$K_{sol} = c_{\text{CO}_2} / p\text{CO}_2$
Carbon dioxide hydration	$\text{CO}_2 + \text{H}_2\text{O} \xrightleftharpoons{K_{hy}} \text{H}_2\text{CO}_3$	$K_{hy} = c_{\text{H}_2\text{CO}_3} / c_{\text{CO}_2}$
Carbonic acid dissociation	$\text{H}_2\text{CO}_3 \xrightleftharpoons{K_{ca}} \text{H}^+ + \text{HCO}_3^-$	$K_{ca} = c_{\text{H}^+} c_{\text{HCO}_3^-} / c_{\text{H}_2\text{CO}_3}$
Bicarbonate anion dissociation	$\text{HCO}_3^- \xrightleftharpoons{K_{bi}} \text{H}^+ + \text{CO}_3^{2-}$	$K_{bi} = c_{\text{H}^+} c_{\text{CO}_3^{2-}} / c_{\text{HCO}_3^-}$
Water dissociation	$\text{H}_2\text{O} \xrightleftharpoons{K_{wa}} \text{H}^+ + \text{OH}^-$	$K_{wa} = c_{\text{H}^+} c_{\text{OH}^-}$
FeCO_3 precipitation	$\text{Fe}^{2+} + \text{CO}_3^{2-} \xrightleftharpoons{K_{sp}} \text{FeCO}_{3(s)}$	$K_{sp} = c_{\text{Fe}^{2+}} c_{\text{CO}_3^{2-}}$

Table 4. Values of the equilibrium constants for the reactions listed in Table 3 [20, 23]

$K_{sol} = \frac{14.5}{1.00258} \times 10^{-(2.27+5.65 \times 10^{-3} T_f - 8.06 \times 10^{-6} T_f^2 + 0.075 \times I)}$ mol/bar
$K_{hy} = 2.58 \times 10^{-3}$
$K_{ca} = 387.6 \times 10^{-(6.41-1.594 \times 10^{-3} T_f + 8.52 \times 10^{-6} T_f^2 - 3.07 \times 10^{-5} p - 0.4772 \times I^{0.5} + 0.1180 \times I)}$ molar
$K_{bi} = 10^{-(10.61-4.97 \times 10^{-3} T_f + 1.331 \times 10^{-5} T_f^2 - 2.624 \times 10^{-5} p - 1.166 \times I^{0.5} + 0.3466 \times I)}$ molar
$K_{wa} = 10^{-(29.3868-0.0737549 \times T_K + 7.4788 \times T_K^2)}$ molar ²

T_f is the temperature in Fahrenheit, T_K is absolute temperature, I is ionic strength in molar and p is the pressure in psi.

The solubility product (K_{sp}) of FeCO_3 has been the subject of some controversy and many different expressions exist [65-76]. Here the latest equation [76] that accounts for both the effects of temperature and ionic strength was used:

$$\log K_{sp} = -59.3498 - 0.041377 \times T_K - \frac{2.1963}{T_K} + 24.5724 \times \log(T_K) + 2.518 \times I^{0.5} - 0.657 \times I$$

where T_K is the temperature in Kelvin. Ionic strength (I) is defined as [77]:

$$I = \frac{1}{2} \sum_i (m_{i+} z_{i+}^2 + m_{i-} z_{i-}^2)$$

where m_i is the species molarity i , z_i is the charge of the species i , symbol + or - indicates the positive or negative charge carried by an ion. The equilibrium equations listed above can be used to determine the actual concentration of the bicarbonate ion $[\text{CO}_3^{2-}]$, required for calculation of supersaturation $\text{SS}_{\text{FeCO}_3}$.

By looking at the expression for SS_{FeCO_3} above, it appears that the key factors that affect it are the concentrations of ferrous ion, $[\text{Fe}^{2+}]$ and the bicarbonate ion $[\text{CO}_3^{2-}]$. The Fe^{2+} concentration $[\text{Fe}^{2+}]$ is usually known, and in the field it is typically present in the concentration range of a few ppm (0 – 10 ppm), while in the lab its concentration can be set and controlled to a desired value. Clearly large concentrations of Fe^{2+} will lead to supersaturation and precipitation of FeCO_3 , particularly at higher temperatures ($>60^\circ\text{C}$) when the kinetics is fast. This fact was used in the present study where rapid formation of FeCO_3 layers was enabled by manipulating the concentration of Fe^{2+} . On the other hand the concentration of the bicarbonate ion $[\text{CO}_3^{2-}]$ is determined primarily by pH and partial pressure of CO_2 . So let us look at the effect of pH first.

Before we proceed, it should be noted that the present analysis relies primarily on thermodynamic considerations. Clearly, the kinetics of FeCO_3 film formation is another important factor that lies beyond the scope of this discussion. While FeCO_3 supersaturation SS_{FeCO_3} is one of the key factors determining the kinetics, the other one is temperature. Only at high temperature ($>50^\circ\text{C}$) FeCO_3 forms fast enough to overpower the undermining corrosion process and form a protective layer. Therefore, the galvanic mechanism of localized corrosion considered here does not carry over to lower temperatures and all the experiments in this study were conducted at 80°C .

2.3.3.1 Effect of pH

As the pH increases (H^+ concentration decreases), the CO_3^{2-} concentration increases as can be easily understood by inspecting the equilibrium reactions listed in Table 3. In Figure 11 the calculated effect of pH on solubility of FeCO_3 is shown for a

given set of operating conditions. Similar graphs for other conditions can be created by solving the equilibrium equations given above. Also in Figure 11 the calculated effect of pH on the *grey zone* is shown, where propagation of localized corrosion can be expected. Practical limits for *grey zone* are taken to be $0.5 < SS_{\text{FeCO}_3} < 2$, as discussed above. If one assumes that the range for Fe^{2+} concentration is 0 – 10 ppm in the field, then under these conditions the graph suggests that it is unlikely to get FeCO_3 precipitation and localized corrosion propagation below pH 5.6. One can judge in this case that the localized attack is possible in the range of pH 5.7 to 6.4. Above pH 6.6 it appears that, for almost any Fe^{2+} concentration, FeCO_3 will precipitate and low uniform corrosion rates will prevail.

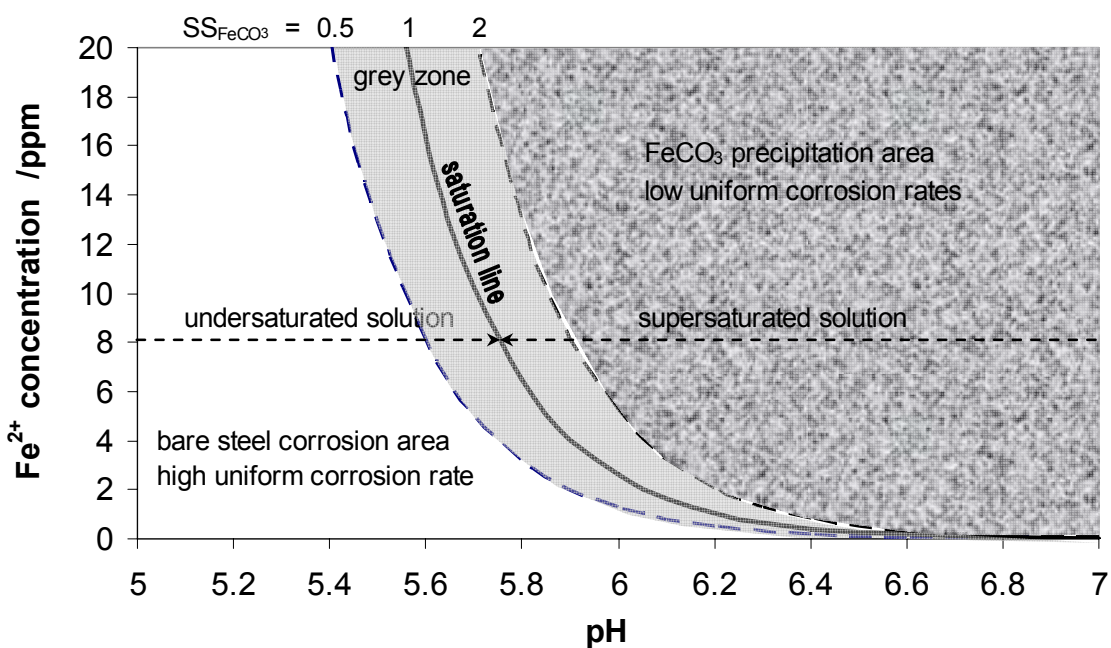


Figure 11. Calculated pH effect on solubility of FeCO_3 and the “grey zone” at $T=80^\circ\text{C}$, $p\text{CO}_2=0.53\text{bar}$, $[\text{NaCl}]=1\text{ wt}\%$.

This was confirmed by conducting AP tests where all parameters were identical other than the pH (Figure 12). The first case at pH5.9 where significant galvanic current and localized corrosion was obtained was already discussed at great lengths above. In an identical experiment conducted at pH6.6 clearly the galvanic current rapidly vanished and no localized corrosion could be observed. Very low general corrosion rates were obtained on both anode and cathode (<0.1 mm/y).

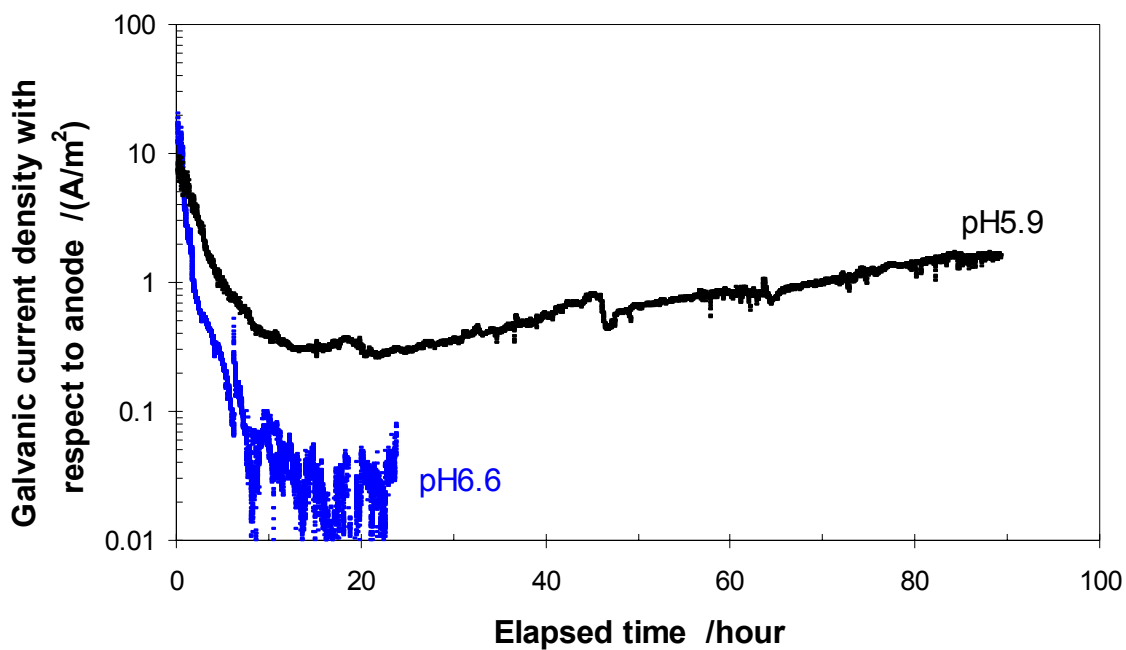


Figure 12. Galvanic current density calculated with respect to the anode with time for different pH at $T=80^{\circ}\text{C}$, $p\text{CO}_2=0.53\text{bar}$, $\text{SS}_{\text{FeCO}_3}\approx 0.5-4$, shallow pit, $[\text{NaCl}]=1\text{wt}\%$, stagnant.

2.3.3.2 Effect of CO₂ partial pressure

The effect of CO₂ partial pressure on solubility of FeCO₃ and indirectly on localized corrosion propagation likelihood can also be deduced by looking at the reaction equilibria presented above. All other conditions being the same, higher partial pressure of CO₂ leads to higher dissolved CO₂ concentration and eventually to higher concentrations of the CO₃²⁻ ion. This means that the solubility of FeCO₃ decreases with increasing partial pressure of CO₂ as shown in Figure 13.

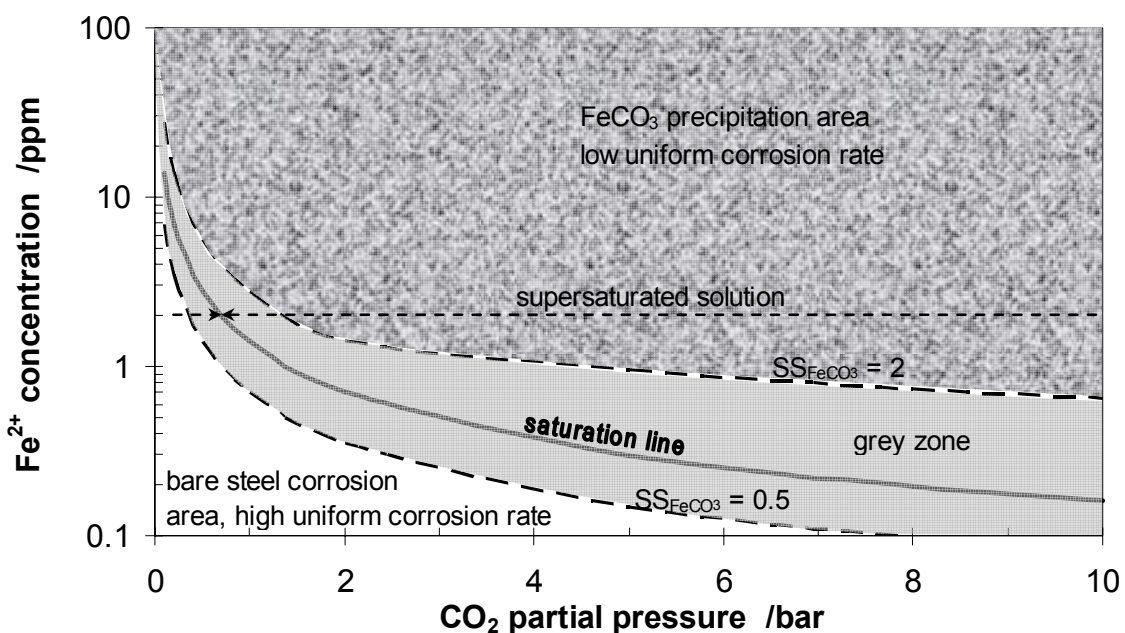


Figure 13. Calculated effect of CO₂ partial pressure on solubility of FeCO₃ and the “grey zone” at T=80 °C, pH 6.0, [NaCl]=1wt%.

It can be seen that at these conditions, FeCO₃ will readily form as the partial pressure of CO₂ exceeds 2 bar for any measurable Fe²⁺ concentration (> 1 ppm) and can

hardly be avoided at even higher partial pressures of CO₂. The *grey zone* conditions can be practically met only in the lower range of partial pressures of CO₂ which are most common for field conditions (< 2 bar). At higher partial pressures of CO₂ the *grey zone* is feasible only for very low Fe²⁺ concentration (< 1 ppm), giving way to protective FeCO₃ film formation, suggesting a very low likelihood of both uniform and localized attack at these conditions.

2.3.3.3 Effect of salt

Another factor that does not appear explicitly in the expression for SS_{FeCO₃} above, but needs to be considered, is the effect of salt (NaCl). Typical concentrations seen in the field brine are 1–3 wt% while condensed water seen in wet gas lines has no salt. However, cases with up to 20 wt% of salt in the brine are not uncommon. In a recent study no effect of salt on general CO₂ corrosion was found across a broad concentration range. However, the effect of Cl⁻ ion concentration on localized CO₂ corrosion has been reported in the literature,^[45, 54, 55] with lower pit density^[45] and higher localized corrosion rate^[54, 55] observed at higher NaCl concentration. In the first approximation, the effect of salt can be included in this analysis by looking at the effect it has on reaction equilibria shown above, by considering a change in ionic strength of the solution. This is summarized in Figure 14 where the calculated effect of NaCl concentration on the solubility of FeCO₃ and the *grey zone* is shown, for a given set of operating conditions. It can be seen that the solubility FeCO₃ increases with increasing salt concentration, making it more difficult to form protective FeCO₃ layers. It also shows that the “grey zone”

widens as the salt concentration increases, making it more likely to get localized corrosion propagation as the concentration of NaCl increases.

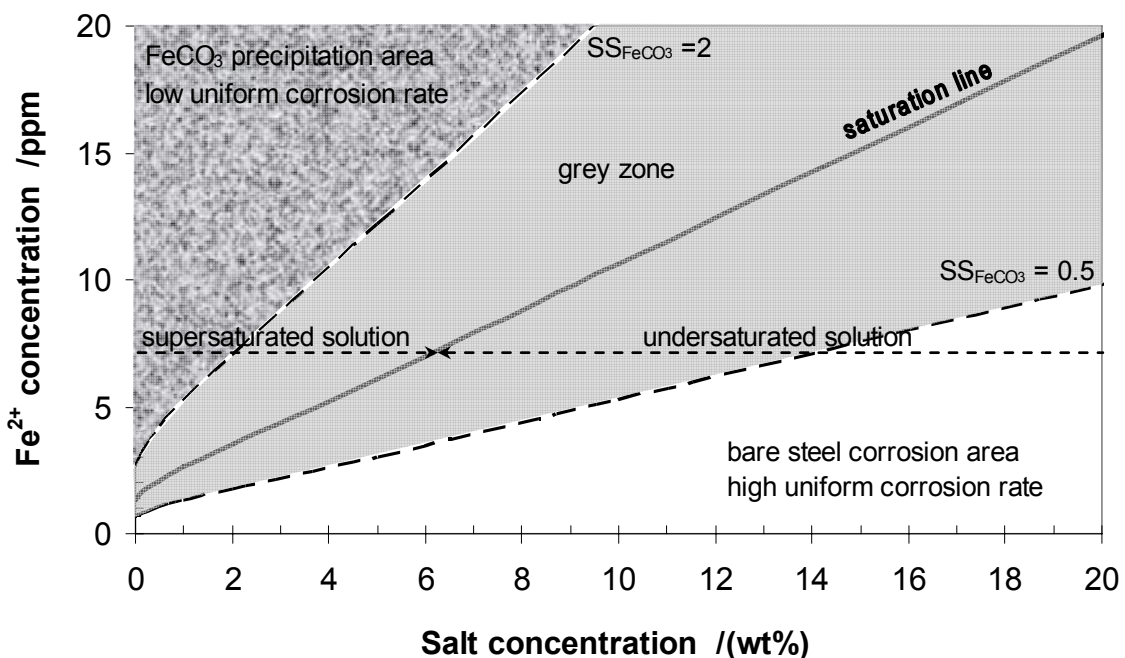


Figure 14. Salt effect on the “grey zone” width at $T=80\text{ }^{\circ}\text{C}$, $p\text{CO}_2=0.53\text{ bar}$, $\text{pH } 6.0$.

To verify this observation, a series of AP tests were conducted at various salt concentrations. The results are summarized in Figure 15, where a significant effect of salt concentration on the galvanic current is evident. The highest localized attack was obtained for the highest NaCl concentration. No localized attack was obtained for the lowest NaCl concentration, what could also be in part attributed to the lower conductivity of the solution.

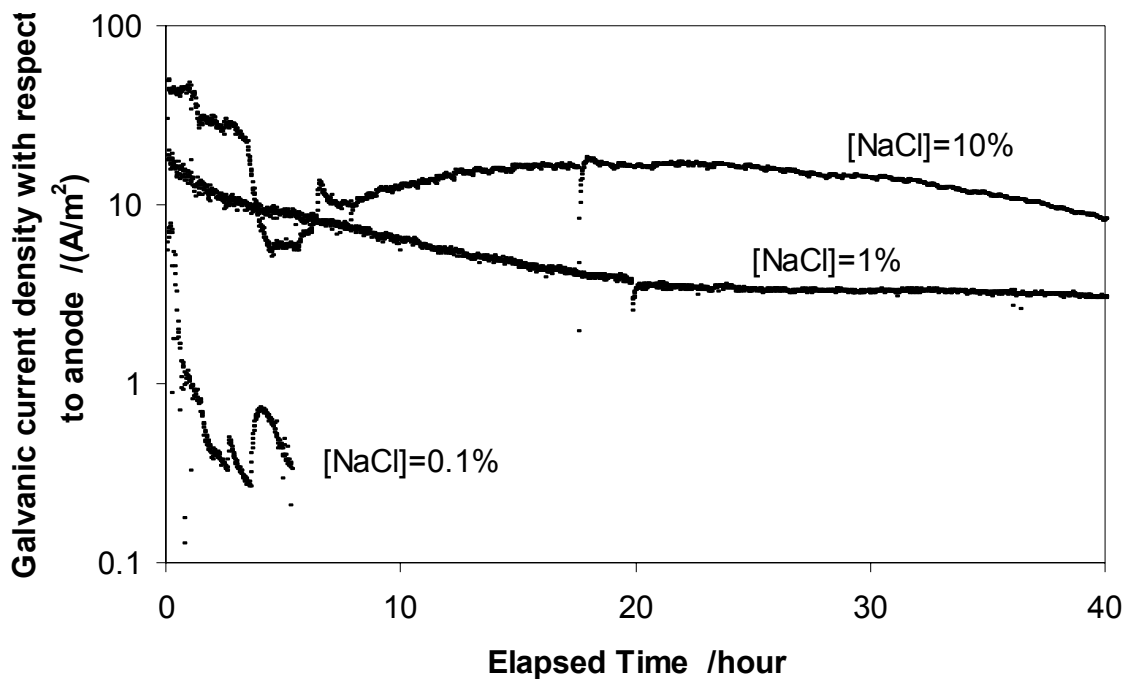


Figure 15. Galvanic current density calculated with respect to the anode for different NaCl concentrations at pH 5.9–6.0, $T=80^{\circ}\text{C}$, shallow pit, $\text{SS}_{\text{FeCO}_3}=0.2\text{--}4$, $\omega=400\text{rpm}$.

2.3.3.4 The effect of flow

Fluid flow was already mentioned as one of the key factors in *initiation* of localized CO_2 corrosion of mild steel. In this study, the focus is on localized corrosion *propagation* and the role of mixing introduced by turbulent flow. To study this effect, another series of tests was conducted with vigorous stirring using a rotating magnet (at 500 rpm) and the results were compared with the stagnant test in the same environment. It is recognized here that this is not the best way to introduce controlled flow conditions; however, it was the only way easily achievable given the constraints of the equipment used. The galvanic current density comparison (stagnant vs. 500 rpm) is depicted in

Figure 16. A significant increase in the galvanic current density under stirred flow condition is observed (although the effect seems to diminish over time). The large difference in the galvanic current can be easily explained by the fact that any accumulation of corrosion products on the anode was minimized by the flow, because of turbulent mixing sweeping away any corrosion products generated in the vicinity of the anode and thereby stabilizing the galvanic cell.

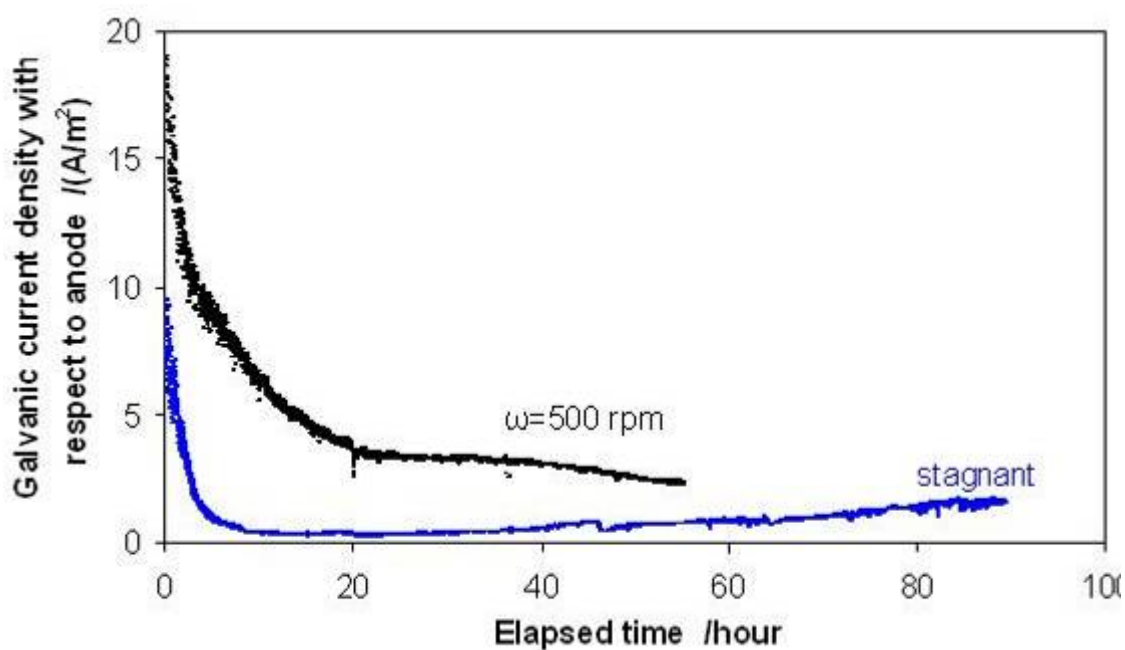


Figure 16. Galvanic current density calculated with respect to the anode for a stagnant and stirred solution using a rotating magnet at pH 5.8-5.9, $SS_{FeCO_3}=0.3-4$, $T=80^\circ C$, shallow pit, $[NaCl]=1wt\%$.

In another series of tests, the anode was receded within the cathode by 2 mm, in order to create a quiet environment shielded from the bulk flow which was agitated by the rotating magnet (Figure 17). These results are compared with others obtained in

experiments conducted under similar conditions in Figure 15. As expected, the receded pit behaved similar to a shallow pit under stagnant condition.

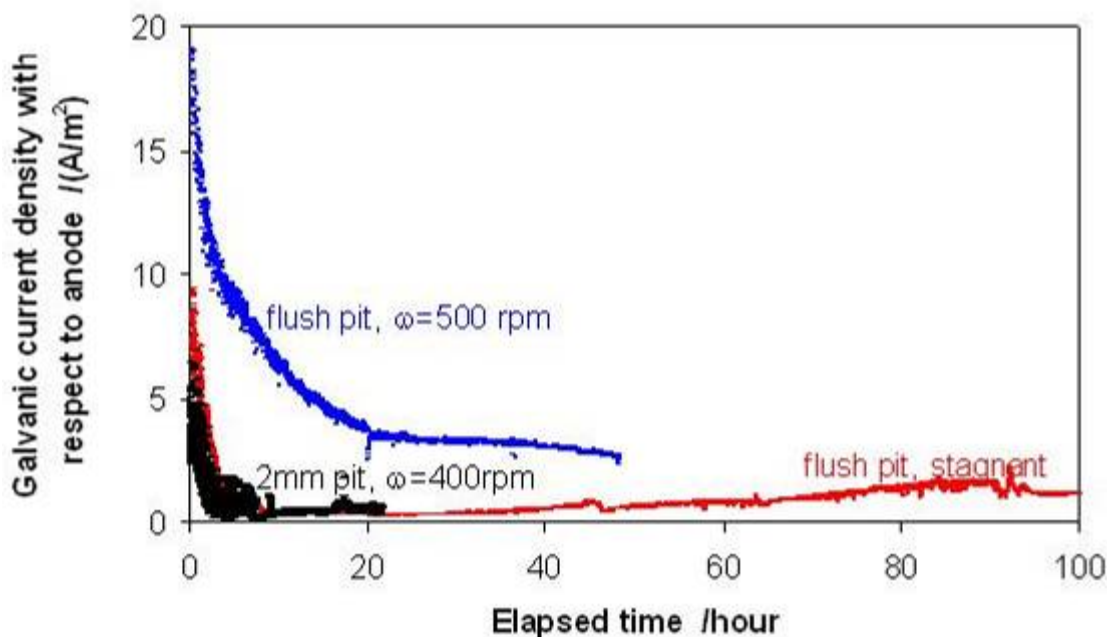


Figure 17. Galvanic current density calculated with respect to the anode for a receded pit (depth=2 mm) and shallow pit (depth<0.1 mm) at pH 5.8–5.9, T=80°C, SS_{FeCO₃}=0.2–4 [NaCl] =1%wt.

In summary these results indicate that once a bare steel surface is exposed to turbulent flow, localized corrosion propagation proceeds very fast initially, due to a galvanic coupling with the FeCO₃ covered surface. However, as the pit recedes, the propagation rate slows down to mass transfer limitations. At some point the propagation may stop altogether if protective FeCO₃ reforms on the steel surface. Conversely if flow and water chemistry conditions remain favorable, rapid pit propagation may continue until the point of line failure.

Chapter 3: Role of passivation in localized CO₂ corrosion of mild steel²

3.1 Introduction

It has already been established that the open circuit potential (OCP) on the scaled surface is higher than that of the bare steel surface and that this results in a galvanic cell being established between these two surfaces, which are connected via the steel substrate. As a consequence, the bare pit surface (anode) is polarized positively and the surrounding cathode surface is negatively polarized at the equilibrium potential (called: galvanic potential, mixed potential or connected potential). The contribution of the cathode to the equilibrium potential is often dominant because the ratio of cathode area to anode area is large in reality (>1000) and is approximately 1000 for artificial pit used here. As a result, the anode is corroded much faster, having been positively polarized.

However the origin of the potential difference between the anode and cathode of the galvanic cell remains unexplained. Possible explanations from electrochemical theory are reviewed below.

It has frequently been stated that the role of iron carbonate scale is to provide a diffusion barrier and a blocking effect to the corrosion reactants moving to the reaction site. If for example the transfer of protons in the cathodic reaction is retarded, the cathodic current becomes diffusion limited. This scenario (#1) is illustrated schematically in Figure 18. The open circuit potential decreases with film formation compared to corrosion of the bare steel surface. However, this is was found to be the case for the beginning of the process of iron carbonate scale formation but ultimately the opposite happened: the potential increased (see Figure 4).

² This chapter has been published as an NACE conference paper, paper No. 08332.

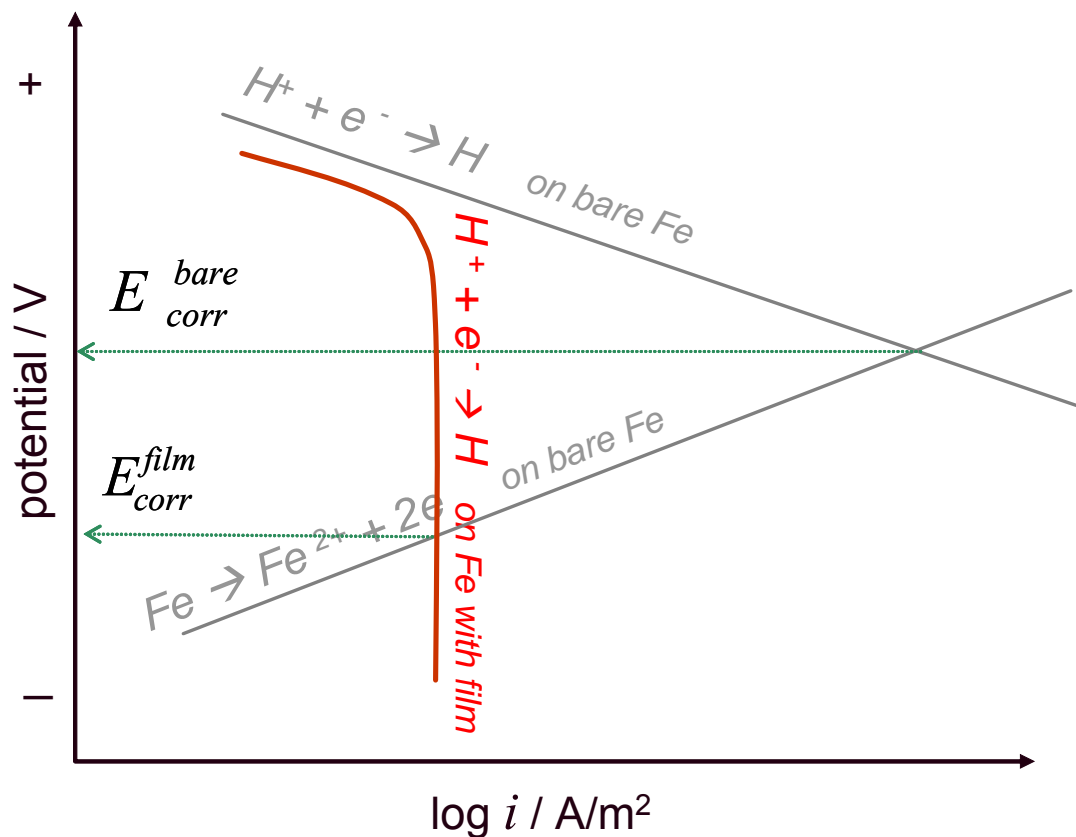


Figure 18 Scenario #1: Open circuit potential decreases for film covered surface where cathodic reaction is mass transfer controlling due to diffusion barrier.

On the other hand, it can be assumed that the corrosion process remains under electrochemical charge transfer control, while the role of the iron carbonate scale is to partially cover/block the active sites for anodic and cathodic reactions – equally. This results in scenario #2, depicted schematically in Figure 19, where both the anodic and cathodic reactions are retarded proportionally due to scale formation. The open circuit

potentials would remain the same before and after film formation. This was obviously not the case (see Figure 4) and this scenario can be discarded as unrealistic.

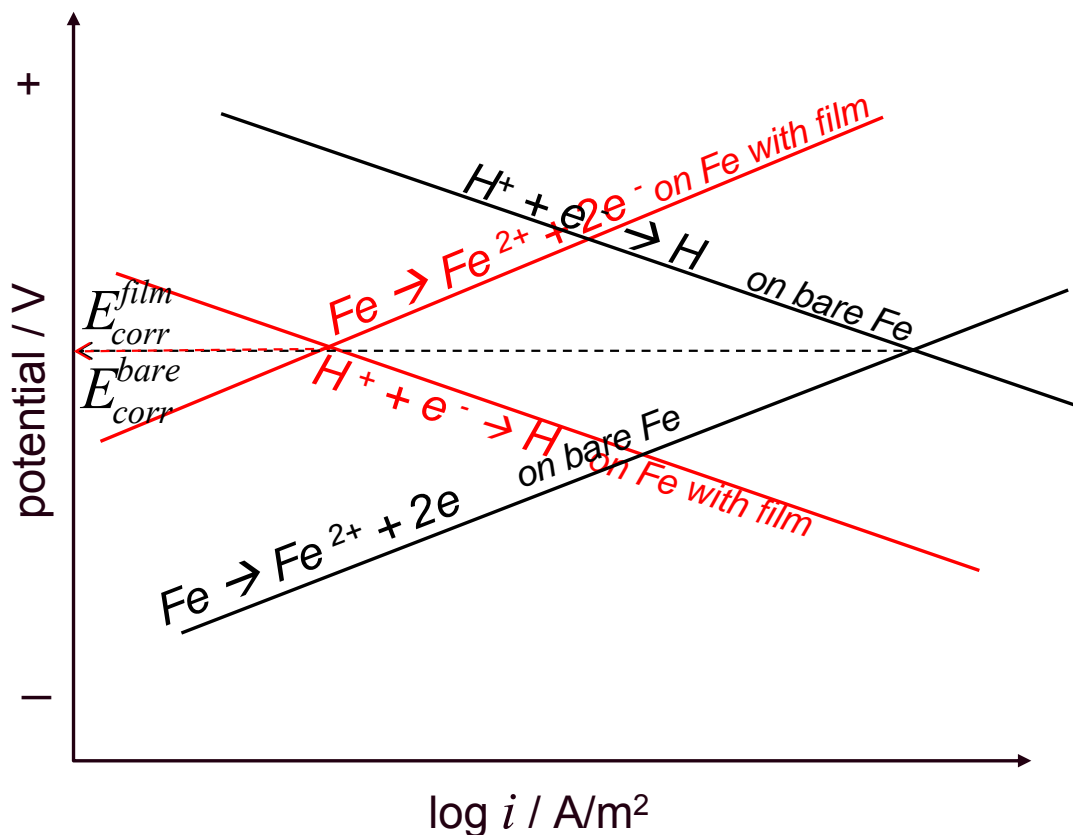


Figure 19. Scenario #2: Open circuit potential remains constant for filmed and bare steel surfaces where both the anodic and cathodic reactions are similarly reduced due to film formation.

Let us consider scenario #3: charge transfer control of the electrochemical reactions persists during scale formation but somehow the cathodic reactions are reduced more than the anodic reactions. This scenario is depicted schematically in Figure 20. The open circuit potentials decrease under scaling conditions what is similar to what is

seen in scenario #1, nevertheless it is now much harder to explain why this selective retardation of the cathodic charge transfer would occur.

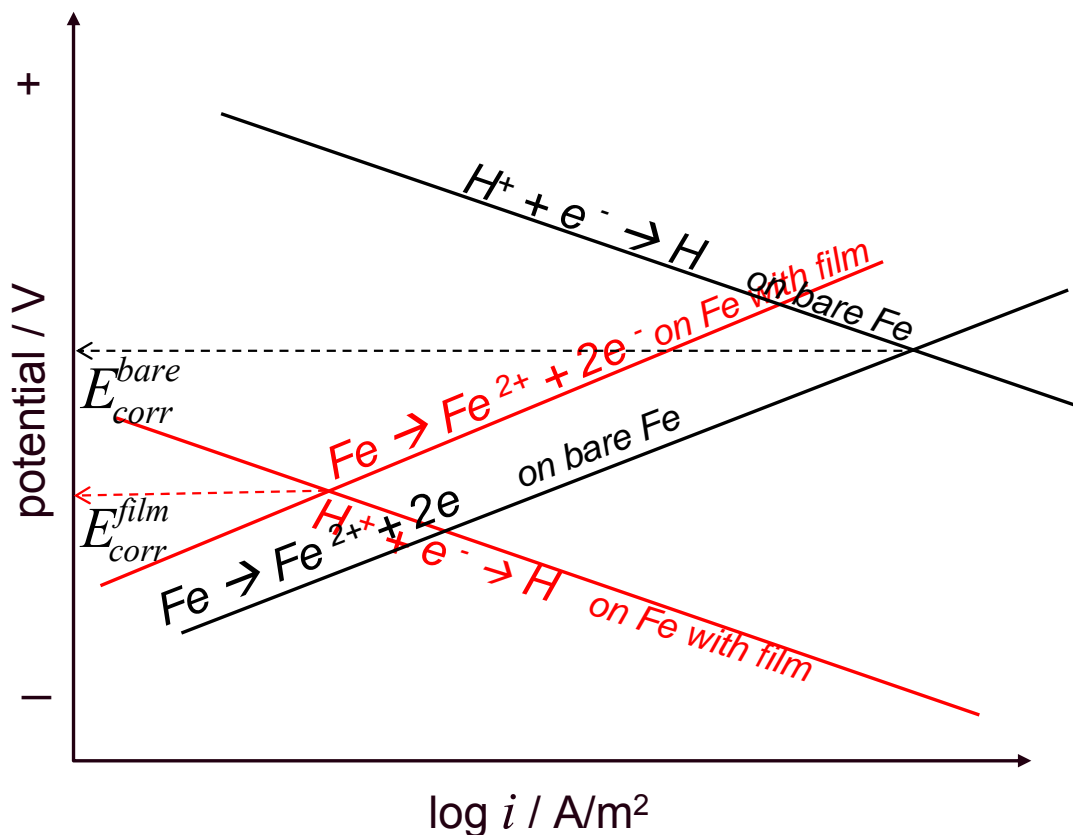


Figure 20. Scenario #3: Decrease in the open circuit potential due to the scale reducing the cathodic reactions more than the anodic reaction.

Another possibility: scenario #4: both reactions remain under charge transfer control but the anodic reaction is selectively more retarded under scale forming conditions as schematically depicted in Figure 21. In this case, the open circuit potentials increases under scaling conditions compared with non scaling conditions. This is a

plausible scenario, given the observed behavior, but it remain hard to explain why this selective retardation is happening.

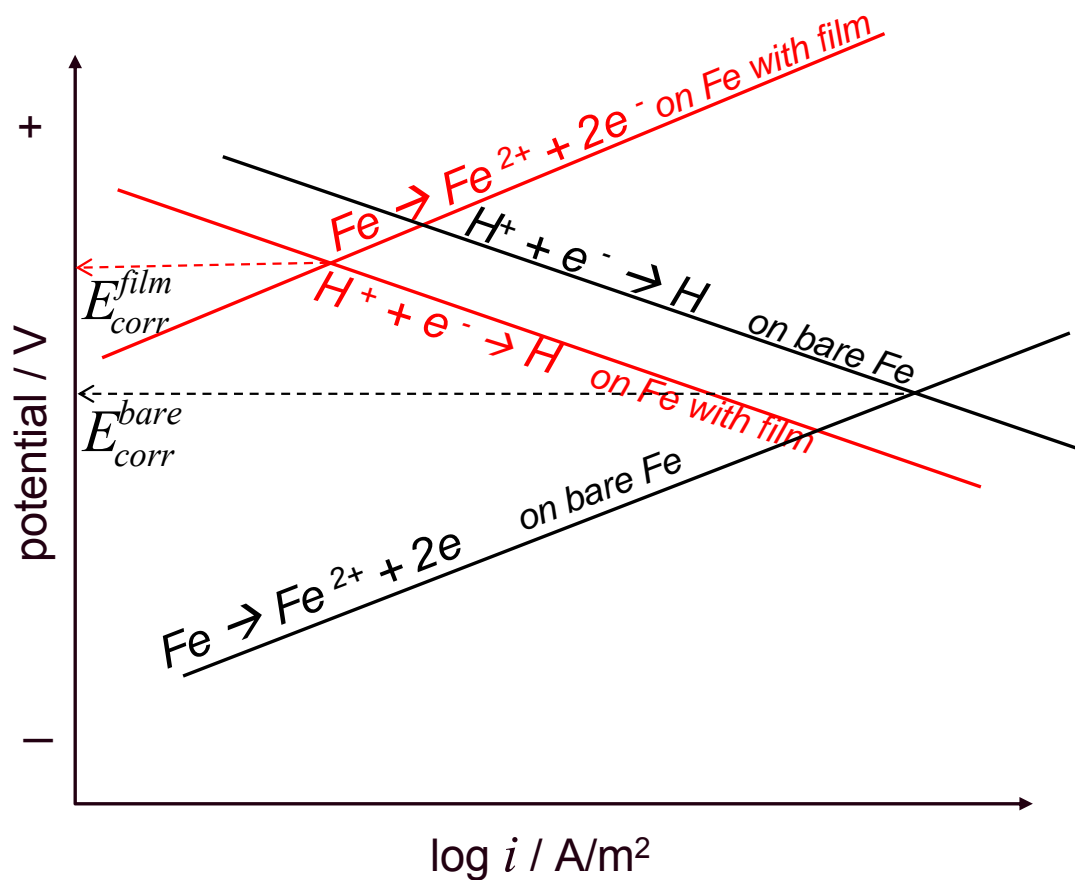


Figure 21. Scenario #4: Increase in the open circuit potential due to the scale reducing the anodic reaction more than the cathodic reactions.

Another scenario (#5) includes steel surface passivation, and is similar to the previous scenario, but offers an explanation why the open circuit potential increase after scale formation: due to formation of a very thin but protective layer that slows down anodic dissolution of iron (such as in stainless steels). Thus, the anodic reaction reaches

a limiting - passive current as demonstrated in Figure 22. The open circuit potential (point B) becomes higher under the passivation than if it were under active charge transfer control at a bare surface (point A). It is hypothesized that this can happen due to the change of local electrolyte condition at the steel surface beneath the FeCO_3 scale

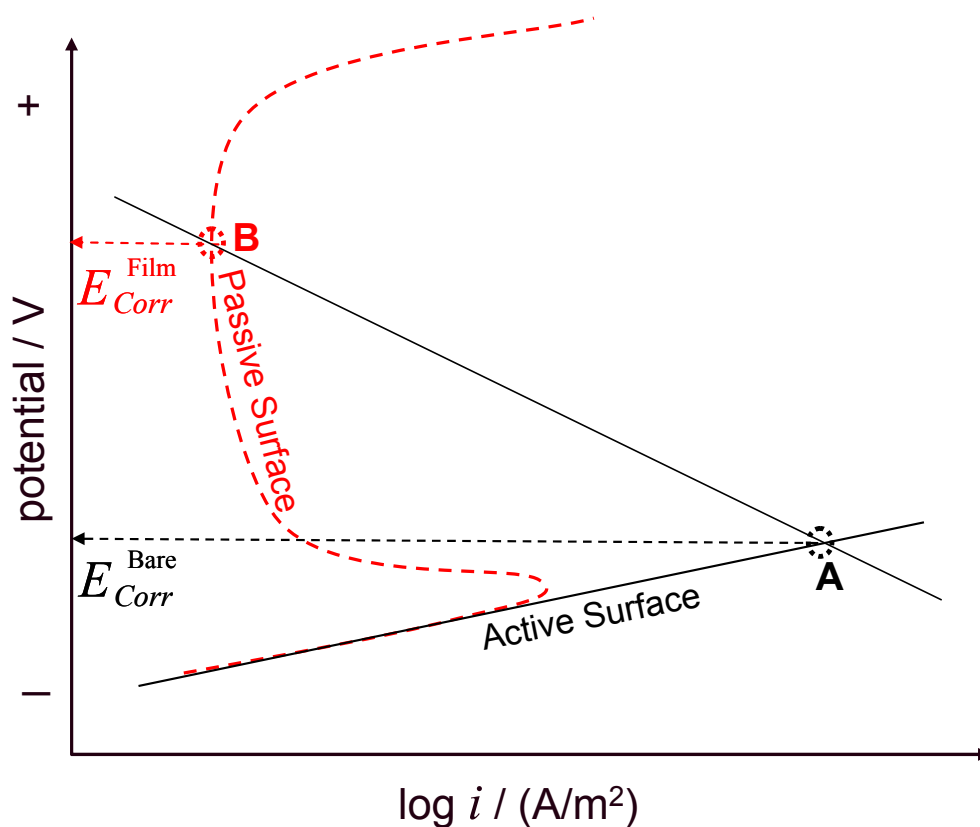


Figure 22. Scenario #5: Open circuit potential increases for passivated surface compared with bare surface.

As seen from the analysis above based on simple electrochemical theory, the potential can increase under scaling conditions only if the anodic reactions are reduced more than the cathodic ones, the most plausible reason for this being when the actively

corroding steel surface becomes passivated. Therefore the objective is now to verify if the mechanism for the potential increase during scale formation is caused by passivation or some other way.

To achieve this goal, a series of tests were conducted using electrochemical methods including potentiodynamic polarization, linear polarization resistance, cyclic polarization on the active and passive surfaces and immersion tests to create a passivated surface without external electrochemical stimuli.

3.2 Experimental design

3.2.1 Setup

A typical three-electrode glass cell was used for the electrochemical polarization tests (Figure 23). The temperature was controlled automatically by the heating plate. The cylindrical rotating cylinder electrode (out wall surface area=5.2 cm²) was polarized potentiodynamically using Gamry® electrochemical measurement equipment.

3.2.2 Procedure

Sodium chloride electrolyte (1 wt% or 10 wt%) was heated to the designated temperature and purged with carbon dioxide for at least three hours. After the temperature was achieved, the pH was adjusted by solid NaHCO₃ (ACROS, ACS analytical grade 99.7%) or its 1M solution and 0.1 M HCl. Extra deaeration was necessary to remove the dissolved oxygen added with the NaHCO₃/HCl. The cylindrical electrode coupon made of C1018 (chemical composition shown in Table 5) or X65 (chemical composition shown in Table 6) mild steel was polished sequentially by 240,

400, 600 grit sand paper. The coupons were cooled by flushing with 2-propanol during polishing, ultrasonicated in 2-propanol then blow dried.

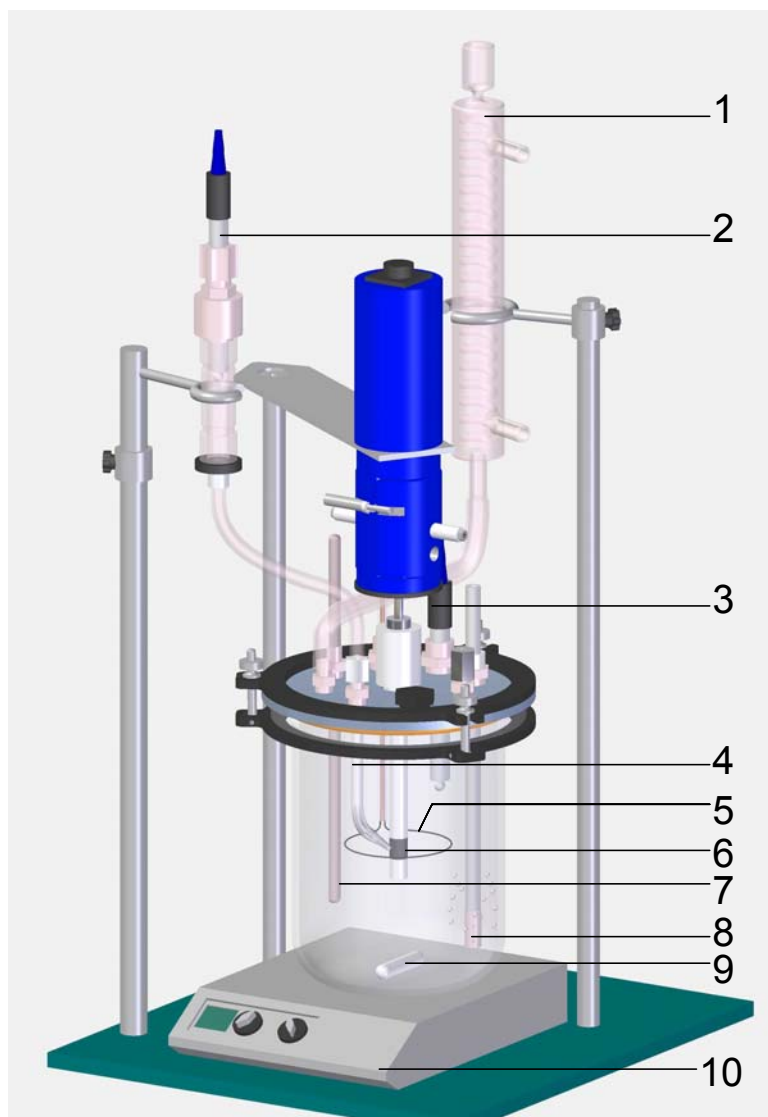


Figure 23. Three electrode electrochemical glass cell ³ [18].

1.- condenser, 2.- reference electrode, 3.- pH probe, 4.- Luggin capillary, 5.- platinum ring, 6.- working electrode, 7.- thermo probe, 8.- gas bubbler, 9.- magnetic stirrer bar, 10.- hotplate.

³ Figure reproduced from ICMT image library with permission.

Table 5. The chemical composition (weight percent) for C1018 carbon steel

Al	As	B	C	Ca	Co	Cr	Cu
0.080	0.060	0.001	0.200	0.001	0.011	0.061	0.028
Mn	Mo	Nb	Ni	P	Pb	S	Sb
0.900	0.018	0.014	0.044	0.017	0.032	0.012	<0.001
Si	Sn	Ta	Ti	V	Zr	Fe	
0.044	0.011	0.023	0.005	0.004	0.007	balance	

The coupons were then immersed into the prepared electrolyte. The solution pH and ferrous ion concentration were continuously monitored during the tests. Open circuit potential (OCP) and polarization resistance were frequently measured. The anodic and cathodic Tafel slopes, 40mV and 120mV respectively, were used to calculate the corrosion rate from the polarization resistance measured by LPR and EIS.

Table 6. The chemical composition (weight percent) for X65 carbon steel

Al	As	B	C	Ca	Co	Cr	Cu
0.00322	0.005	0.0003	0.05	0.004	0.006	0.042	0.019
Mn	Mo	Nb	Ni	P	Pb	S	Sb
1.32	0.031	0.046	0.039	0.013	0.02	0.002	0.011
Si	Sn	Ta	Ti	V	Zr	Fe	
0.31	0.001	0.007	0.002	0.055	0.003	balanced	

For the potentiodynamic sweep polarization, cathodic polarization started first from the stable open circuit potential. Anodic polarization was executed after the open circuit potential was attained. Most of the specimen were polarized in less than 20 minutes right after immersion.

For the cyclic polarization experiments, the potential sweep always began from the initial open circuit potential and increased in the positive direction and then reversed back to initial open circuit potential at scanning rates of 0.2 mV/s, 1 mV/s and 5 mV/s.

Spontaneous passivation was achieved when the open circuit potential increased and stabilized without any external electrochemical stimuli after the coupon was immersed in the corrosion environment. Spontaneous passivation potential was in some cases 400 mV higher than the open circuit potential for the fresh metal surface. Once spontaneous passivation was achieved, deaerated 0.01 M hydrochloric acid was added in order to decrease pH and induce depassivation.

3.2.3 Test matrix

Table 7. Potentiodynamic sweep polarization test matrix

Coupon material	C1018
Coupon area /cm ²	5.4
Temperature /°C	80
Partial pressure of CO ₂ /bar	0.53
pH	3–6, 7, 8
NaCl concentration /(wt%)	1, 10
Ferrous iron concentration /ppm	0, 2, 11
Flow	0
Polarization speed /(mV/s)	0.2
Anodic polarization range /(V vs. OCP)	0.2, 0.6–0.8
Cathodic polarization range /(V vs. OCP)	-0.2

The test matrix for potentiodynamic polarization testing is listed in Table 7. Environmental factors including NaCl concentration, pH and ferrous iron concentration were investigated. The salt concentration was controlled at 1 wt% and 10 wt%. The pH was controlled between 4 and 8. Fe^{2+} concentration was in the range of 0–11 ppm.

Table 8. spontaneous polarization tests matrix

Coupon material	C1018
Coupon area / cm^2	5.4
Temperature / $^{\circ}\text{C}$	25, 50, 80
Partial pressure of CO_2 / bar	0.53
pH	6.6, 7.1, 7.8, 8.0
NaCl concentration / wt%	1
Ferrous iron concentration / ppm	Initial =0
Solution stirring	0

Table 9. Cyclic polarization test matrix

Coupon material	C1018
Coupon area / cm^2	5.4
Temperature / $^{\circ}\text{C}$	80
Partial pressure of CO_2 /bar	0, 0.1
pH	7, 8
NaCl concentration /(wt%)	1
Initial Fe^{2+} concentration /ppm	0
Flow	0
Polarization speed /(mV/s)	0.2, 1 and 5
Anodic polarization range /(V vs. OCP)	0.2, 0.6–0.8
Cathodic polarization range /(V vs. OCP)	-0.2

From spontaneous passivation tests, the pH and temperature effects on spontaneous passivation were studied mainly in deaerated 1 wt% NaCl electrolyte with CO₂. The conditions are summarized in Table 8. The conditions shown in Table 8 for depassivation only differ from those used for the spontaneous passivation in that the temperature and initial pH are fixed at 80°C and 7.8, respectively. Stepwise reduction in pH used to initiate depassivation was achieved by addition of hydrochloric acid with mild solution rotation in order to ensure uniform mixing. Table 9 summarizes the conditions for cyclic polarization tests.

3.3 Results and discussion

3.3.1 Passivation observation from potentiodynamic polarization tests

The potentiodynamic sweeps were carried out for the active surface in the range of bulk pH 4 to pH 7 at salt concentrations of 1 wt% (Figure 24) and 10 wt% (Figure 25).

For both salt concentration levels, steel passivation was observed above pH 7 within the 200 mV anodic polarization range. The passivation current density and potential were smaller for pH 8 than those at pH 7. This indicates that passivation preferably occurred at a higher pH. This fact can facilitate the understanding of the localized corrosion mechanism previously observed which suggests that passivation can happen under locally high pH conditions between the iron carbonate scale and the steel surface even if the bulk pH is not high enough to initiate passivation. It is necessary to mention that many of the following tests were carried out under high pH, ca. 7-8, in order to speed up the measurements and simulate the locally higher pH beneath the iron carbonate scale.

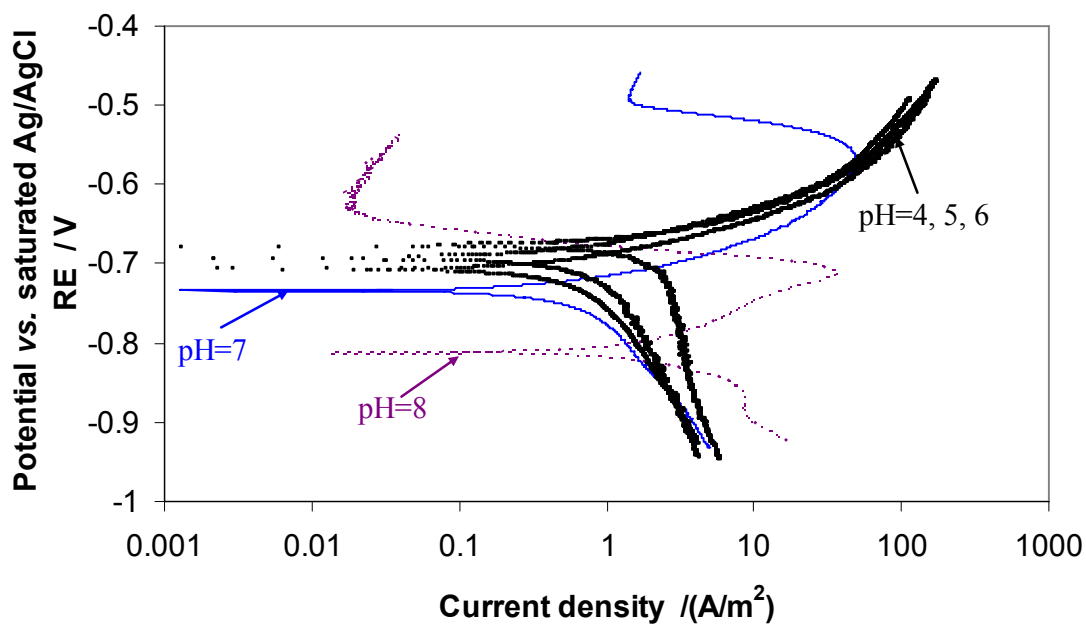


Figure 24. Potentiodynamic polarization sweep curves starting from the open circuit potential on active surfaces at $[\text{NaCl}] = 1\% \text{wt}$, $T=80^\circ\text{C}$, $p\text{CO}_2=0.53 \text{ bar}$, stagnant flow.

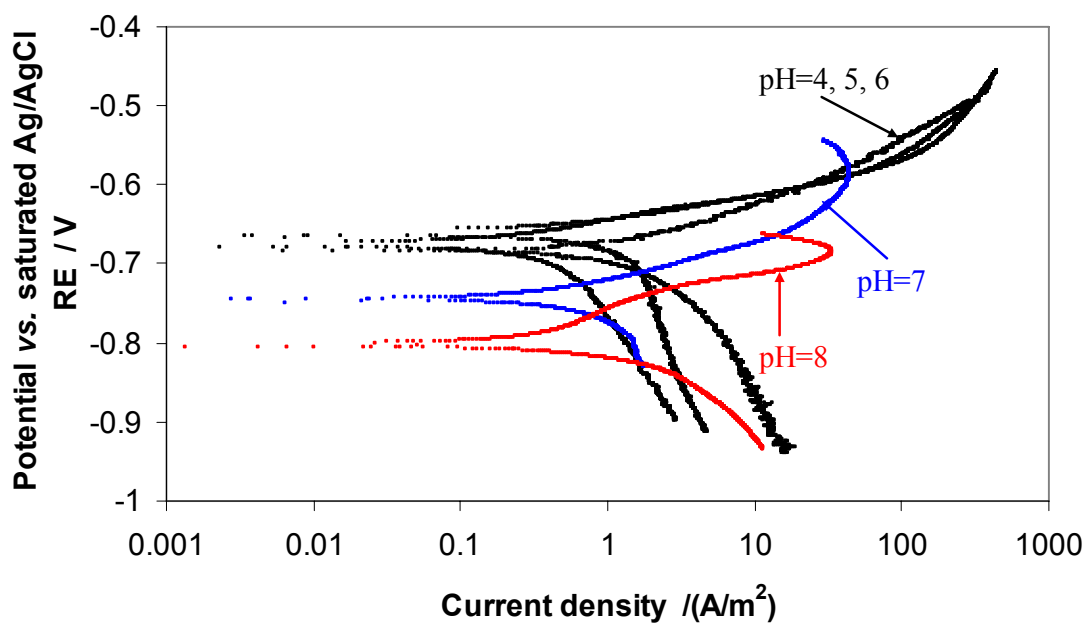


Figure 25. Potentiodynamic polarization sweep curves starting from the open circuit potential on active surfaces at $[\text{NaCl}] = 10\% \text{wt}$, $T=80^\circ\text{C}$, $p\text{CO}_2=0.53 \text{ bar}$, stagnant flow.

pH effect on passivation

The polarization sweep curves at pH7 and pH8 are shown in Figure 26. From the results, the active surface at pH 8 is passivated at a lower anodic overpotential and current density.

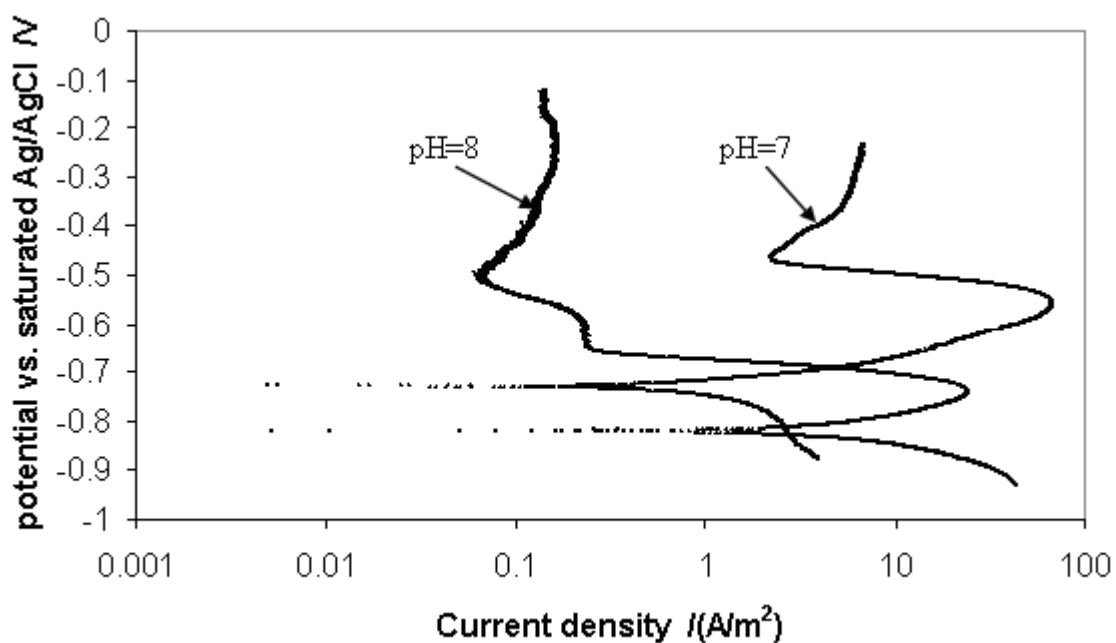


Figure 26. Potentiodynamic polarization sweep curves starting from open circuit potential on active surfaces at $[\text{NaCl}] = 1\% \text{wt}$, $T = 80^\circ\text{C}$, $p\text{CO}_2 = 0.53 \text{ bar}$, stagnant flow condition.

Salt effect on passivation

Two sweep tests were run at the same conditions except for the salt concentration levels to investigate the effect on corrosion mechanisms as shown in Figure 27. No significant passivation difference was observed for the pitting potential and passive

current density between the two tests, which seems to be going against the prevailing literature which suggest that Cl^- affects the pitting CO_2 corrosion. This could be explained by the water chemistry used in the present experiments. To achieve solution pH of 7, a large amount of sodium bicarbonate (200 grams) was added. The contribution to the ionic strength by NaCl (1 wt%) was offset by the already present NaHCO_3 (20 wt%). Therefore it is not surprising that little effect of NaCl concentration on the passivation or localized corrosion was observed.

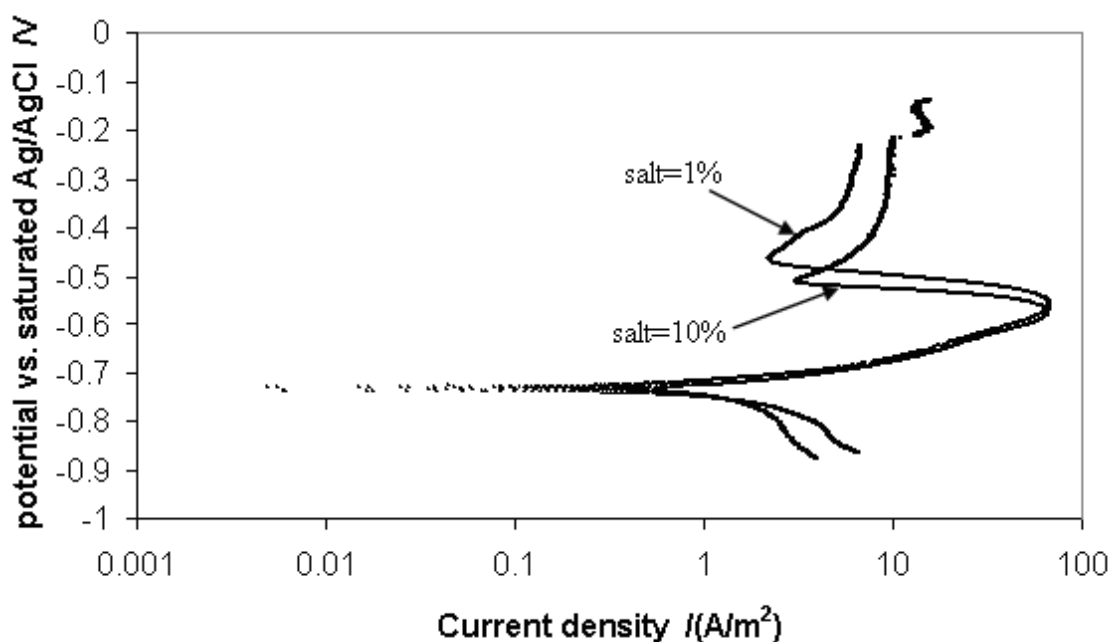


Figure 27. Potentiodynamic polarization sweep curves starting from open circuit potential on active surfaces at pH 7, $T=80^\circ\text{C}$, $p\text{CO}_2=0.53$ bar, stagnant flow condition.

Ferrous iron concentration effect on passivation

Sets of electrochemical characteristics for passive potentials are demonstrated from the potentiodynamic sweep curves as depicted in Figure 28 and Figure 29 under

different levels of Fe^{2+} concentration (0 ppm and 1 ppm at pH 7, 0 ppm and 11 ppm at pH 8). The passive current density and passivation potential at 0 and 11 ppm iron concentration show the same magnitude indicating that ferrous ions do not have a significant effect on the passive or trans-passive potentials when they are polarized starting from the fresh active surface.

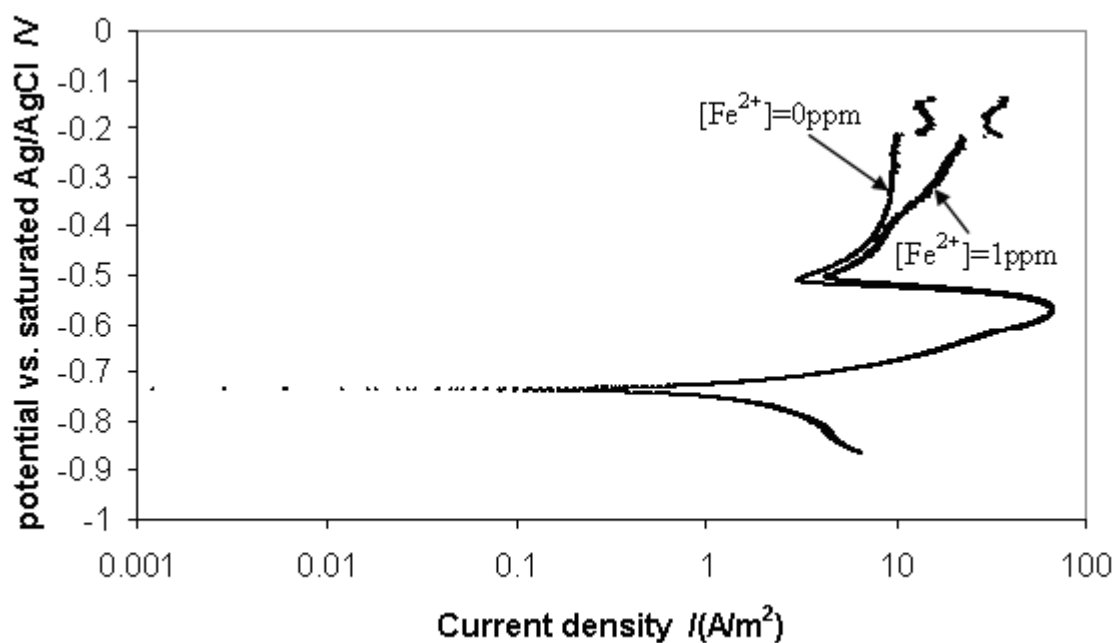


Figure 28. Potentiodynamic polarization sweep curves starting from open circuit potential on active surfaces at pH 7, $T=80^\circ\text{C}$, $p\text{CO}_2=0.53 \text{ bar}$, stagnant flow condition.

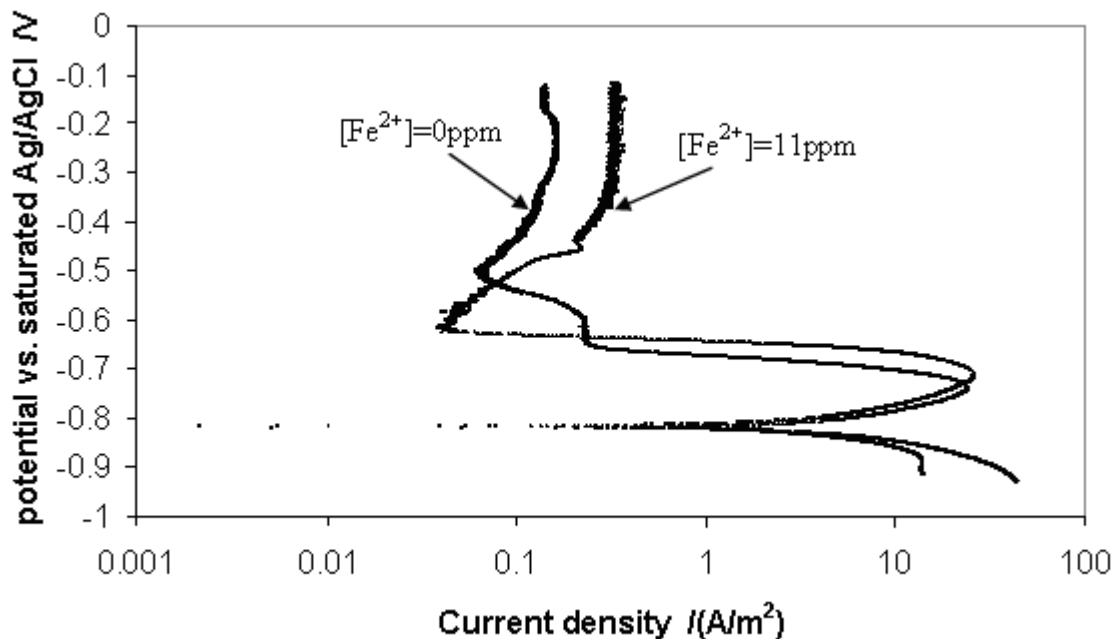


Figure 29. Potentiodynamic polarization sweep curves starting from open circuit potential on active surfaces at pH 8, $T=80^{\circ}\text{C}$, $p\text{CO}_2=0.53$ bar, stagnant flow condition.

Scale effect on passivation

Corrosion product scale, mainly composed of iron carbonate, can be formed throughout the corrosion process in undersaturated conditions in the bulk, once supersaturation at the steel surface is achieved, irrespective of whether anodic potential is applied or not. The effect of scales on the passivation was investigated and presented below.

Potentiodynamic polarization was applied before and after forming an iron carbonate scale (see Figure 30). Comparison of these two polarization curves show that both the anodic and cathodic reactions are retarded by the scale. The passivation potential for the scaled surface is lower (ca. 60mV) than that for the bare surface. The current needed to reach passivation is also lower for the scaled surface than that for the

fresh steel surface. These observations suggest that iron carbonate scale assists the passivation, in other words, passivation is preferentially established under scale formation conditions.

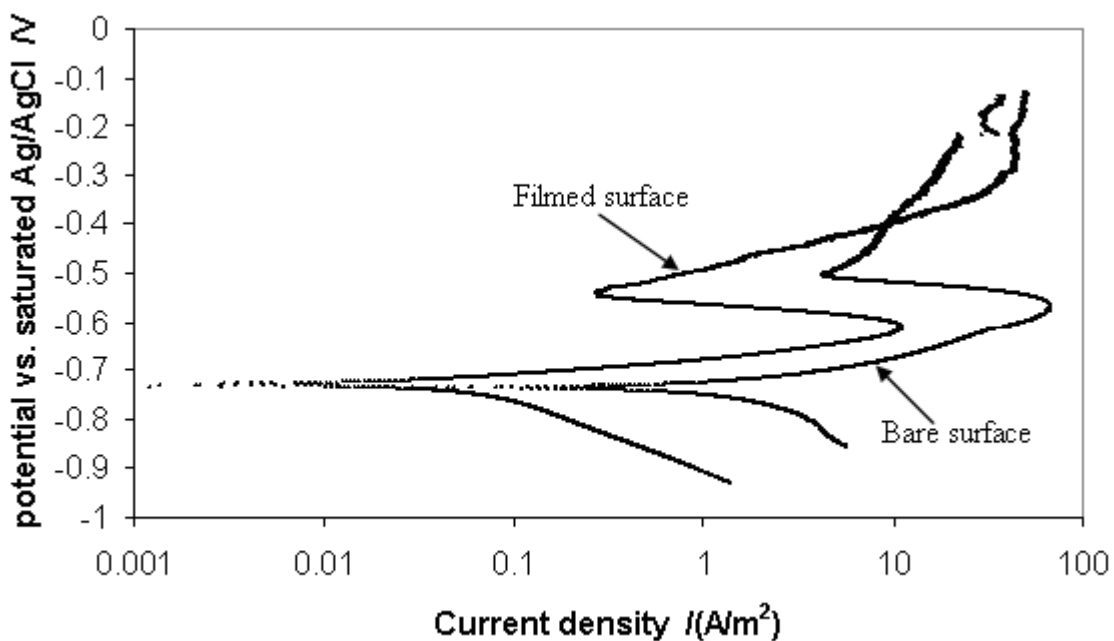


Figure 30. Comparison of potentiodynamic polarization sweep curves starting from open circuit potential on active and scaled surfaces at pH 7, $T=80^{\circ}\text{C}$, $p\text{CO}_2=0.53$ bar, stagnant flow condition.

In another series of experiments, the steel coupons were immersed in the solution without an external applied potential or current. Initially an iron carbonate scale was formed on the surface, the corrosion potential decreased initially and a protective film was formed. Subsequently the potential increased (due to self-polarization) to a potential which was 400 mV higher than the initial corrosion potential as recorded in Figure 31. This is clearly a spontaneous passivation process.

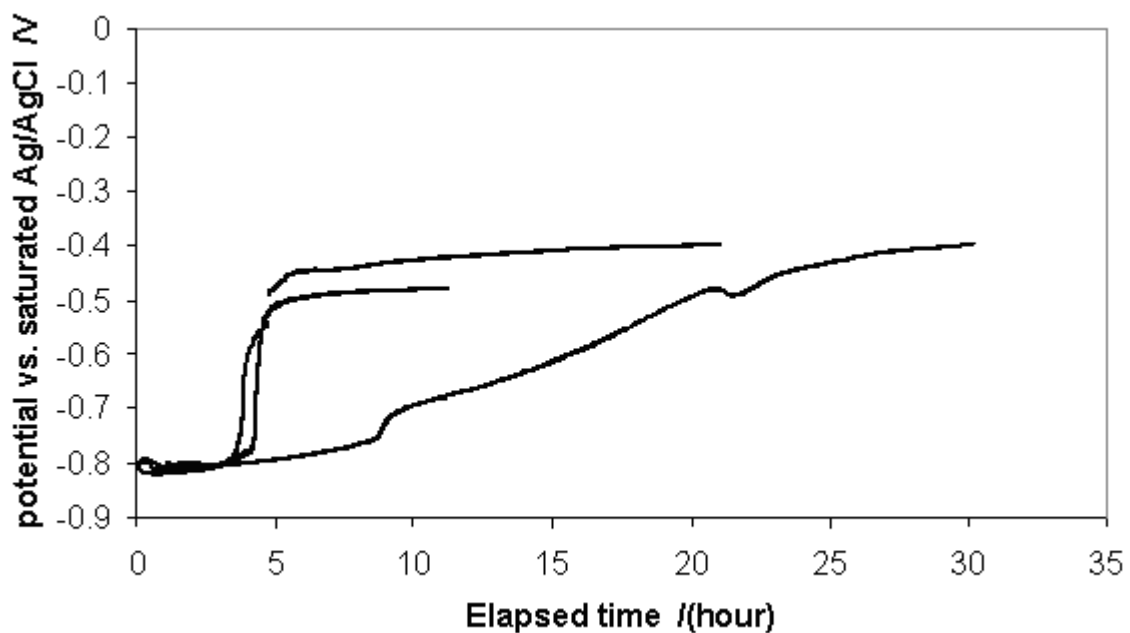


Figure 31. Potential change during the film formation at $\text{pH}\approx 8.0$, $T=80^\circ\text{C}$, $P_{\text{CO}_2}=0.53$ bar, stagnant flow condition.

The polarization sweep, as shown in Figure 32, was carried out when a spontaneous passive film was formed after 20 hours, which was indicated by an increased and stabilized open circuit potential around -400 mV vs. saturated Ag/AgCl reference electrode and corrosion rate was in the magnitude of 0.01 mm/y. Notice that the open circuit potential for bare steel was at -800 mV vs. reference electrode with a corrosion rate around 2-3 mm/y.

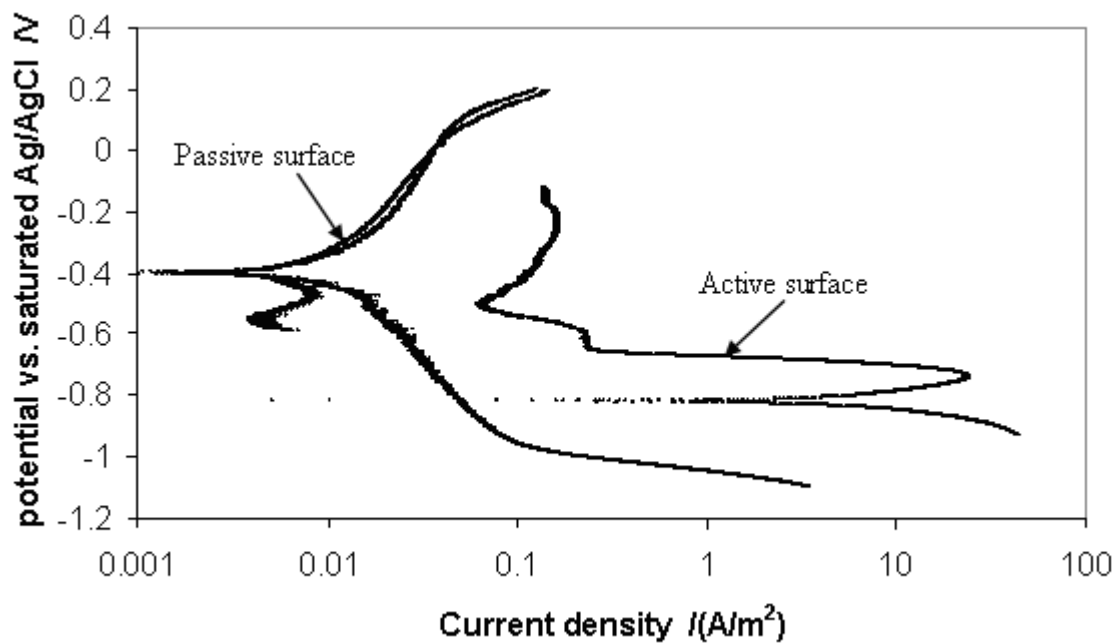


Figure 32. Comparison of potentiodynamic polarization sweep curves starting from open circuit potential on active and filmed surfaces at pH 8, $T=80^{\circ}\text{C}$, $p\text{CO}_2=0.53$ bar, stagnant flow condition.

3.3.2 Passivation observation from cyclic polarization tests

Polarization technique, cyclic polarization, was applied to investigate the passive film properties under mildly alkaline conditions, in a simulation of the local environment beneath the iron carbonate scale. The scan rate was varied from 0.2mV/s to 5mV/s . The tests were run under dilute NaOH or NaHCO_3 solutions (for comparison) deaerated by pure nitrogen, pure carbon dioxide or their mixtures at 80°C and pH 8–9.

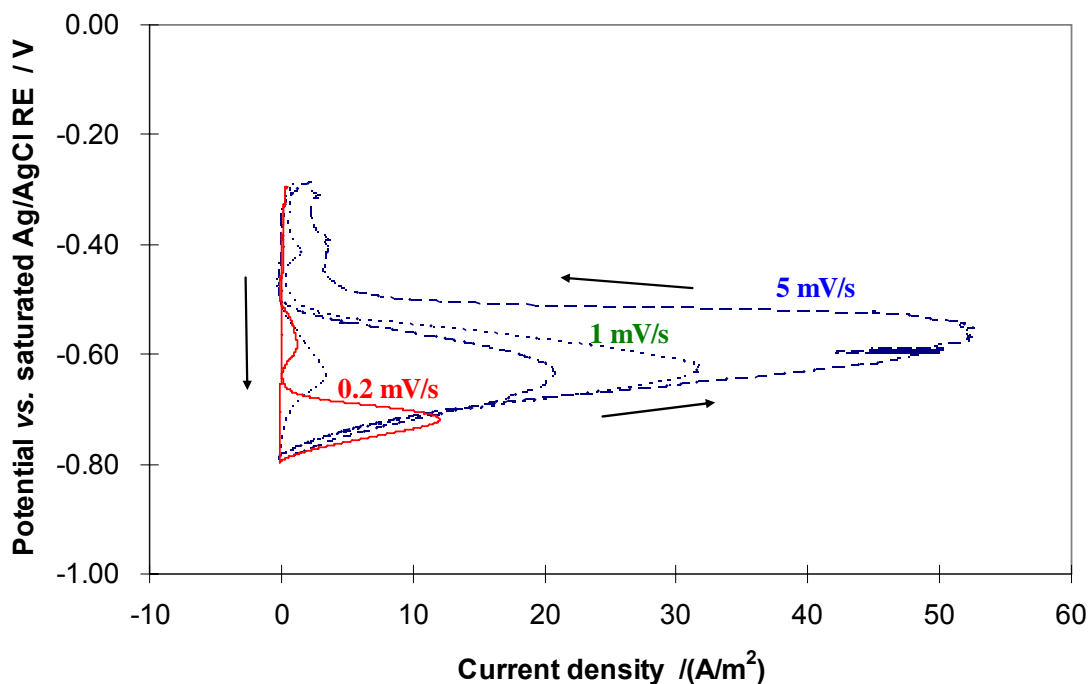


Figure 33. Cyclic polarization curve of mild steel at different scan rate in CO₂ purged NaHCO₃ solution under T=80°C, pH 8.

Surface passivation (as characterized by the inflection where the current or current density began to decrease as the potential is forced to be more positive) was found consistently under the CO₂ purged NaHCO₃ environments for all the polarization rates tested from 0.2mV/s to 5mV/s as shown in Figure 33. From this figure, it can be seen that the metal was passivated during the first half of the polarization sweep in which the potential was changed in the more positive direction. During the second half of each cyclic polarization, the potential was changed in the more negative direction following the end of the first half of the scan cycle. The film appears to have survived the reverse scan as no significant reduction peaks were observed.

In the NaOH solution purged by nitrogen (without CO₂), passivation was only observed at the lowest polarization rate of 0.2mV/s as shown in Figure 34. The passivation potential was much higher than that at the same polarization rate in a CO₂ system with same bulk pH. This indicates that the passivation is more difficult to achieve under the alkaline solutions without the presence of CO₂.

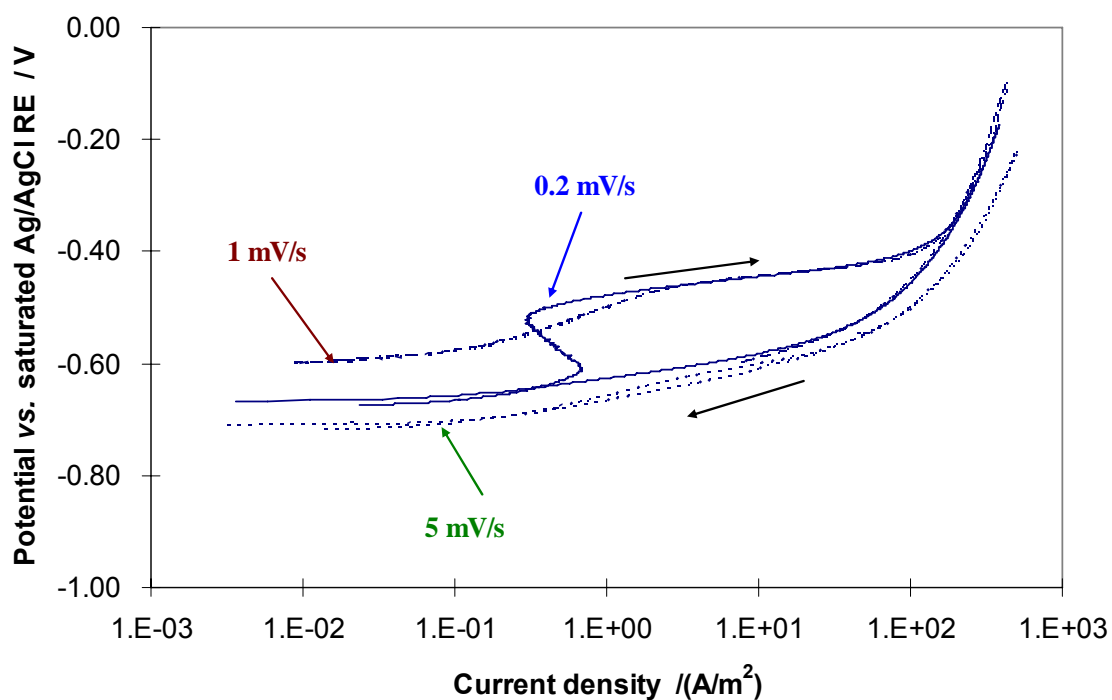


Figure 34. Cyclic polarization curve of mild steel at different polarization rate in deaerated NaOH solution under T=80°C, pH 8.

In summary, the observations made using the potentiodynamic polarization sweeps support the assumption that mild steel passivation is preferentially achieved at higher pH, *i.e.*, due to the locally increased pH beneath the iron carbonate scale. In order

to find further compelling evidence for this hypothesis, spontaneous passivation process was investigated next and the results are presented below.

3.3.3 Spontaneous passivation observations

It has been clearly shown that the passivation of mild steel in CO₂ solutions can be achieved by anodic polarization, *i.e.*, by accelerating the anodic reaction. Therefore, a new series of experiments was done to establish if this will also happen spontaneously, in a process without any external electrochemical stimuli including applied current or potential. This is a more realistic scenario closely related with the observations of localized corrosion and is termed “self-passivation” or “spontaneous passivation” and will be discussed in the following sections.

The effect of pH on spontaneous passivation

To carry out a spontaneous passivation test, freshly ground steel was immersed in the electrolyte and allowed to corrode without external polarization *i.e.* at its open circuit potential. An open circuit potential increase was observed after a few hours of immersion at pH 8 as depicted in Figure 35. This spontaneous passivation phenomenon was also observed in the pH range from 7.1 to 8.1, however the time to reach spontaneous passivation was longer at lower pH, which not surprising as more time is needed to accumulate sufficient ferrous iron to form a corrosion scale and a passive film. The stabilized spontaneous passivation potential tended to decrease at lower pH values as depicted in Figure 35.

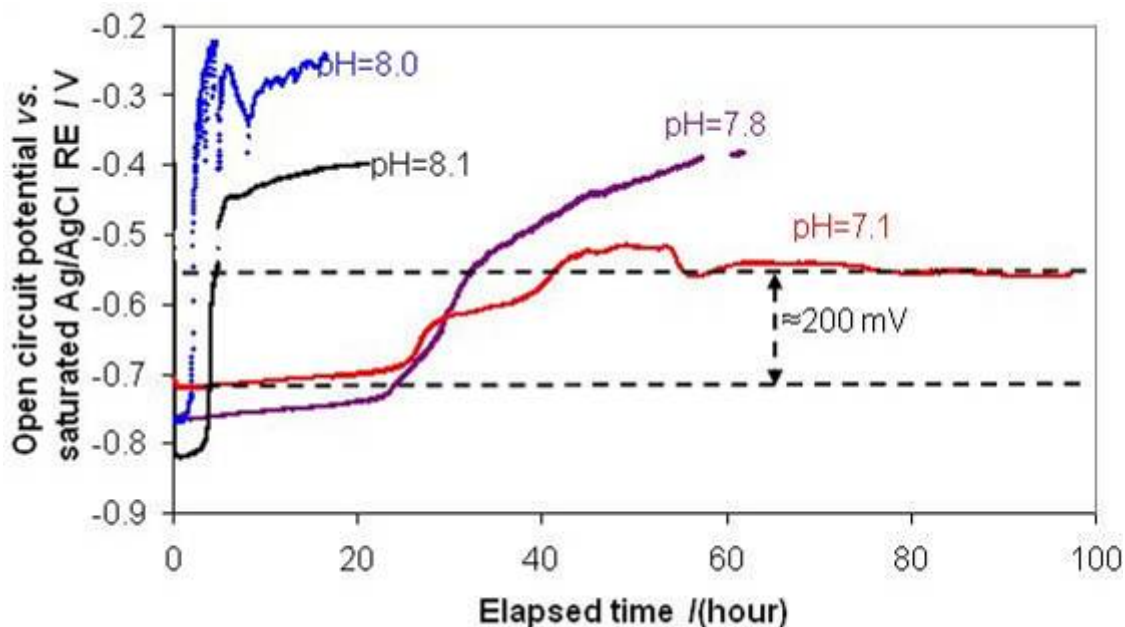


Figure 35. The open circuit potential during spontaneous passivation is affected by pH at $T=80^{\circ}\text{C}$, $P_{\text{CO}_2}=0.53$ bar, $\text{NaCl}=1$ wt%, stagnant flow condition.

These experiments can be seen as direct proof of the hypothesis made at the beginning of this chapter suggesting that spontaneous passivation will occur and increase the potential of the iron carbonate covered steel surface. Let us recall what the implications are for spontaneous passivation for localized corrosion? Consider an experiment where carbon steel has been completely spontaneously passivated at a pH of 7.1, as in Figure 35. The open circuit potential is around -0.550 V vs. a saturated Ag/AgCl reference electrode. If the iron carbonate scale and the passive film are partially damaged, the open circuit potential for the bare metal surface would be equal to the initial potential of the bare surface immediately after immersion (≈ -0.730 V vs. saturated Ag/AgCl RE). A galvanic cell would be established between these two surfaces. The potential difference (*ca.* 200 mV) can, in theory, cause localized corrosion

rates to become thousands of times greater than the uniform corrosion rate of a bare metal surface, these extreme numbers estimated without consideration of IR drop, mass transfer and pit geometry.

The effect of temperature on spontaneous passivation

The spontaneous passivation curves at different temperature (25°C and 80°C) are shown in Figure 36. The time to reach spontaneous passivation is longer at lower temperatures, as expected. No significant difference was observed for spontaneous passivation potential.

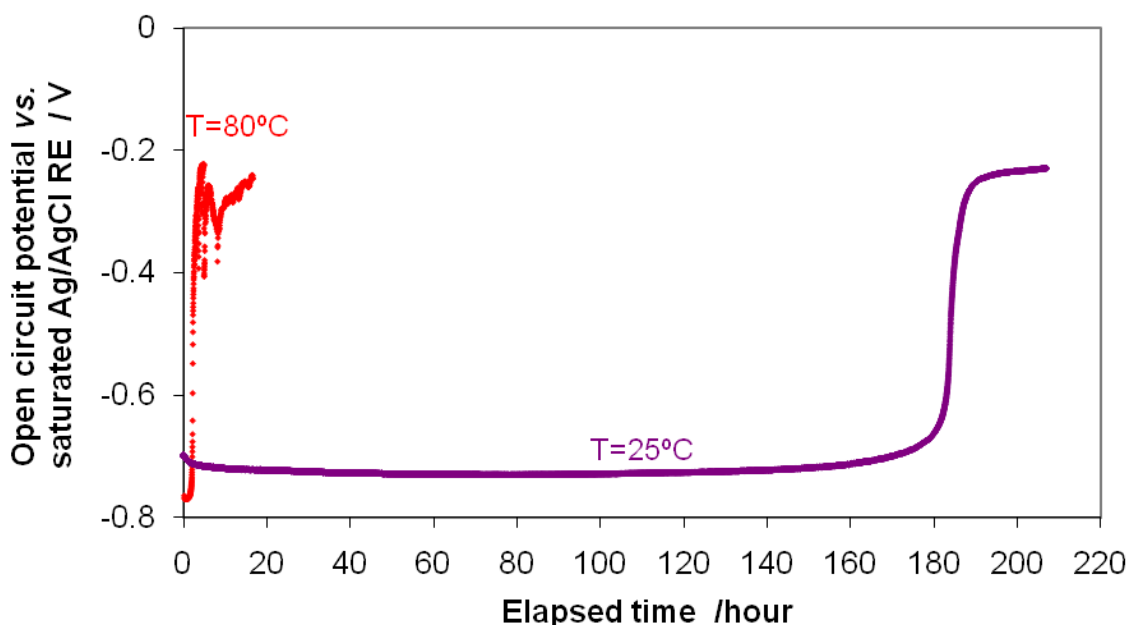


Figure 36. Temperature effect on the open circuit potential during spontaneous passivation at pH 7.5, $P_{CO_2}=0.53$ bar, NaCl=1 wt%, stagnant flow condition.

3.3.4 Role of $\text{CO}_2/\text{FeCO}_3$ in spontaneous passivation

From the potentiodynamic polarization experiments, preliminary results suggested that CO_2 was necessary to assist in the passivation of the steel. Its effect on the spontaneous passivation was investigated in the following series of experiments.

Role of $\text{CO}_2/\text{FeCO}_3$ on the spontaneous passivation

The passivation tests were carried out in electrolyte saturated with CO_2 , N_2 and the mixture of gases at 80°C and pH 8 for N_2 purged NaOH solution and CO_2 purged NaHCO_3 solution. The spontaneous passivation test results, as demonstrated in Figure 37, show that spontaneous passivation was observed even with a 7% molar fraction of CO_2 in the gas phase, but was not observed when pure N_2 was used as the purge gas.

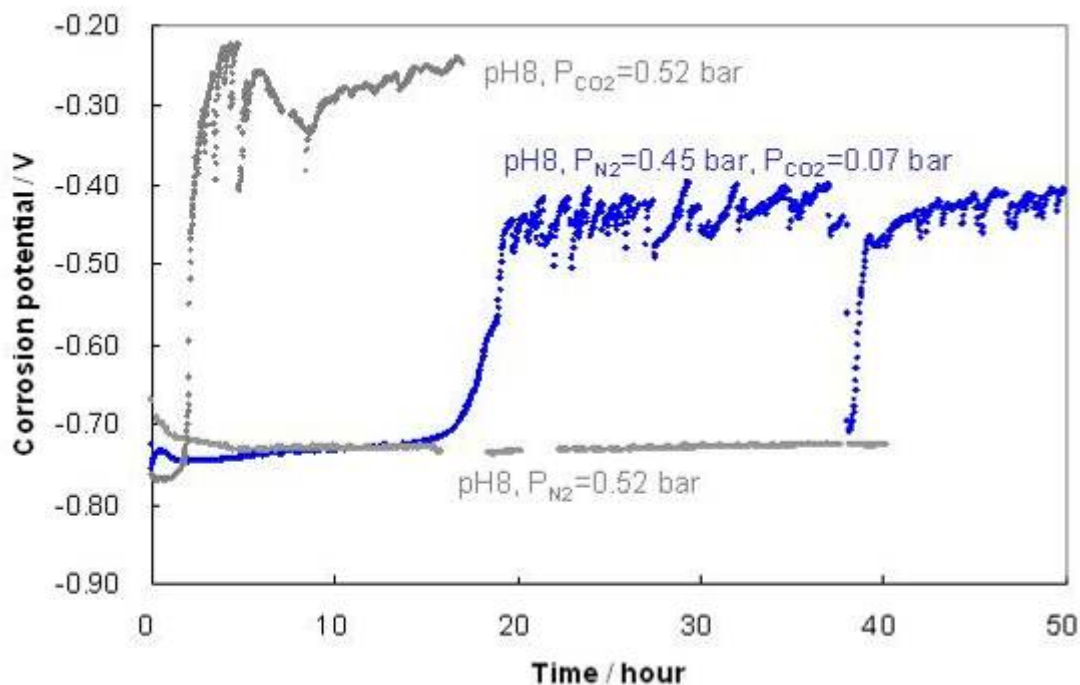


Figure 37. Open circuit potential vs. time for mild steel in NaOH system under $T=80^\circ\text{C}$, pH8, $P_{\text{N}_2}=0.45$ bar, $P_{\text{CO}_2}=0.07$ bar compared with CO_2 purged solution.

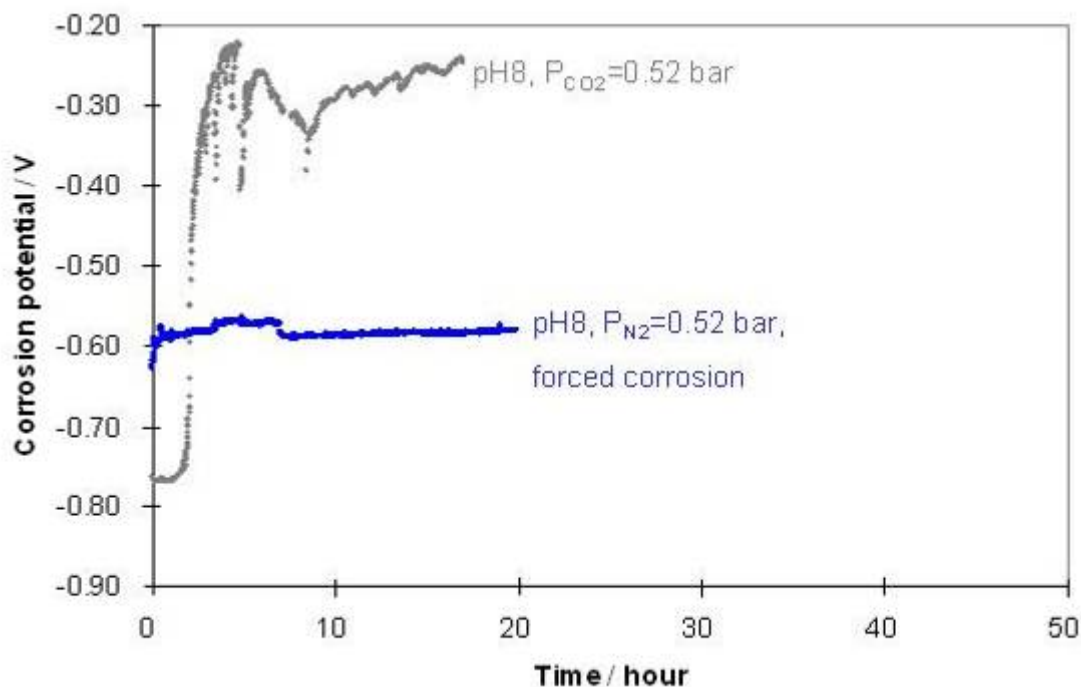


Figure 38. Open circuit potential vs. time of mild steel in NaOH system at pH8, $P_{N_2}=0.52$ bar, applied anodic current density= 6 A/m^2 ^[57] compared with CO_2 purged solution.

A possible reason for the lack of spontaneous passivation in the absence of CO_2 could be that the corrosion rate is different for these two systems although under same pH. This is due to one extra cathodic reaction, the direct reduction of carbonic acid, which leads to a much higher corrosion rate in a CO_2 system compared to a N_2 system, and generates much more ferrous ions required for scaling and passivation. As measured, the corrosion rate under the CO_2 purged solution can reach 2–3 mm/yr, which is one magnitude higher than the corrosion rate under N_2 purged electrolyte. In an attempt to prove this hypothesis, an anodic current was applied to the steel sample in N_2 purged

solution, which resulted in a corrosion rate almost three times higher than that in the CO₂ saturated electrolytes. However the hypothesis had to be discarded as spontaneous passivation was not achieved (Figure 38) even with accelerated corrosion in a N₂ purged solution.

The steel surface was not spontaneously passivated even at a pH of 9.5 in the nitrogen purged NaOH alkaline solution as depicted in Figure 39. Thus, this argument suggests that formation of passive films is closely related with the presence of CO₂ in solution.

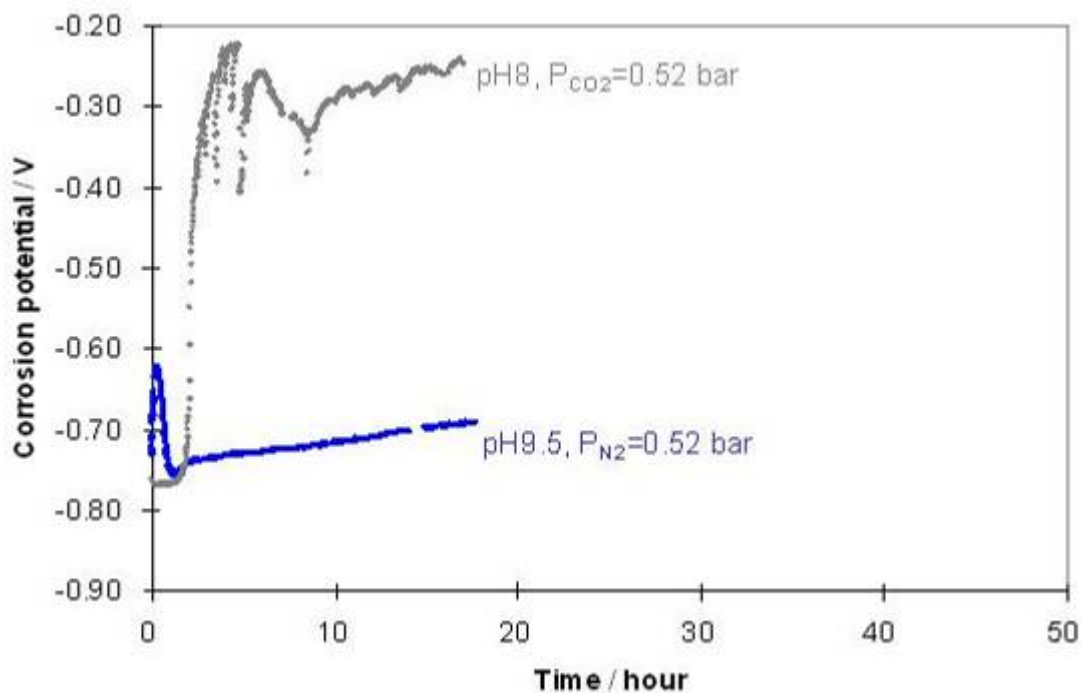


Figure 39. Open circuit potential vs. time for mild steel in NaOH system at pH 9.5, P_{N₂}=0.52 bar compared with CO₂ purged solution.

The role of FeCO₃ in Passivation and Depassivation?

From the above discussion on the role of iron carbonate scale in passivation, it appears that FeCO_3 scale is closely related to mild steel passivation. We can go one step further and boldly assume that the passive film is made up from iron carbonate. One can then assume that passivation can only be achieved when the saturation point for iron carbonate is greater than unity and should dissolve away if the solution becomes undersaturated wrt. iron carbonate. The first part of this hypothesis was proven many times over and described in the text above but let us investigate the second half of the hypothesis by inducing depassivation by decreasing pH on a steel surface where an iron carbonate scale already formed and passivation was observed.

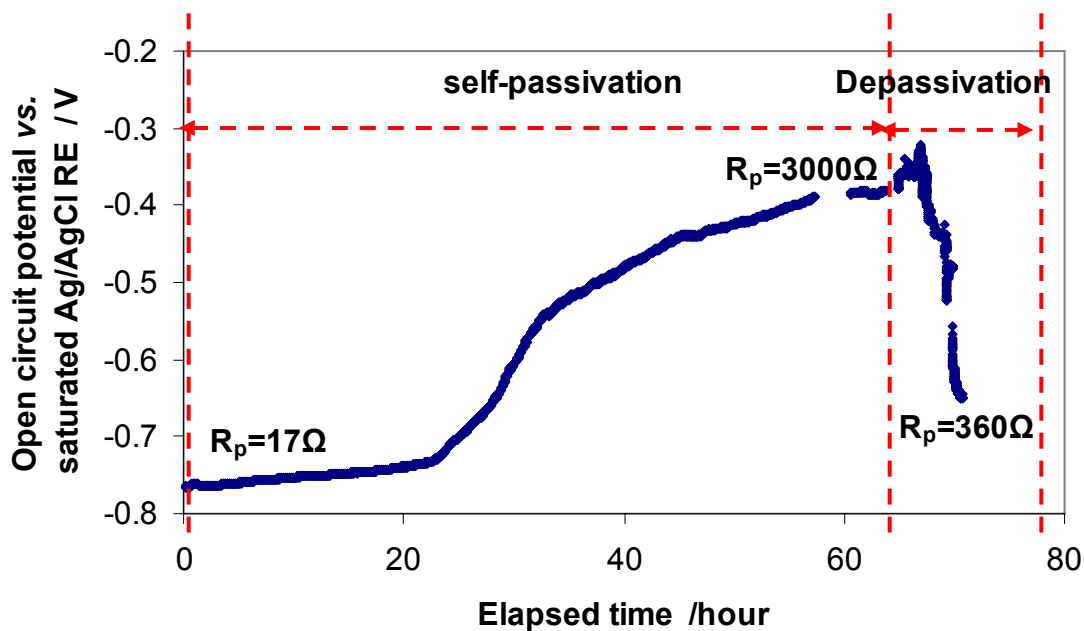


Figure 40. Case1: The spontaneous passivation (at initial pH 7.8, $T=80^\circ\text{C}$, $P_{\text{CO}_2}=0.53$ bar, $[\text{NaCl}] = 1\%$ wt, stagnant solution) and depassivation by decreasing pH from pH 7.8 to pH 5.4.

A typical potential profile in a spontaneous passivation and depassivation test called “Case 1”, is depicted in Figure 40. This case shows that after passivation was achieved, depassivation was directly related to the pH decrease as indicated by the decrease in open circuit potential.

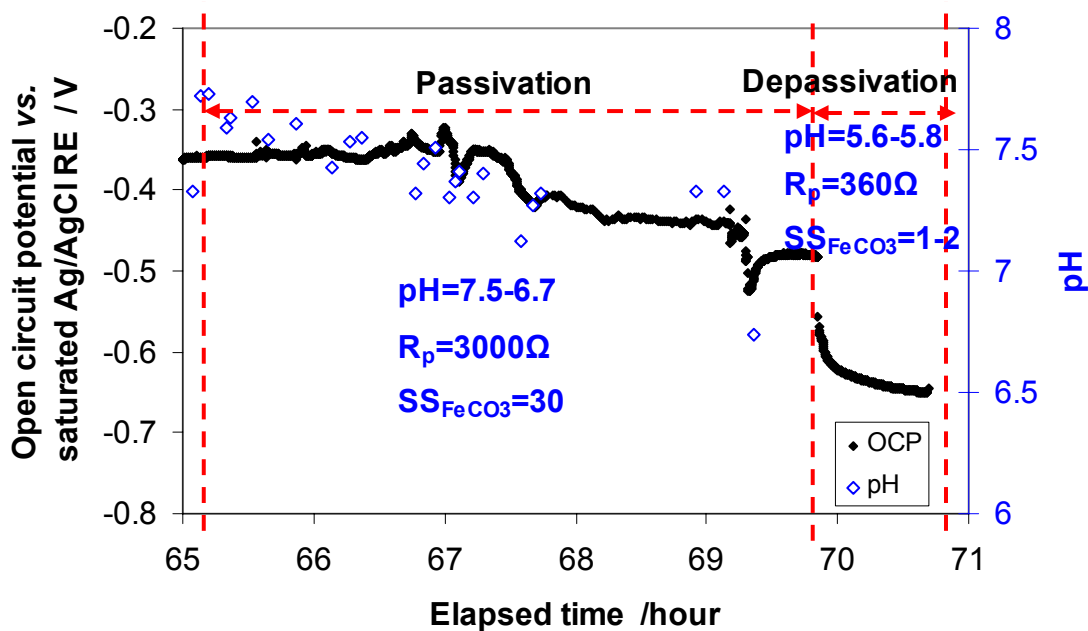


Figure 41. Case 1: relation between supersaturation of FeCO_3 and depassivation at $T=80^\circ\text{C}$, $P_{\text{CO}_2}=0.53$ bar, $[\text{NaCl}]=1$ wt%, stirring speed 300rpm.

A more detailed version of the same graph with passivation/depassivation is given in Figure 41 where values for pH and FeCO_3 supersaturation (calculated from the model by W. Sun, *et al.*⁷⁶) were added, both of which directly relate to FeCO_3 formation/dissolution. Note that during depassivation the solution conditions with respect to FeCO_3 actually remained supersaturated (saturation $\gg 1$) as the pH was decreased and passivation was gradually lost. This implies that the ferrous carbonate

scale did not dissolve, but the mild steel surface depassivated. The survival of iron carbonate scales was confirmed by scanning electron microscopy.

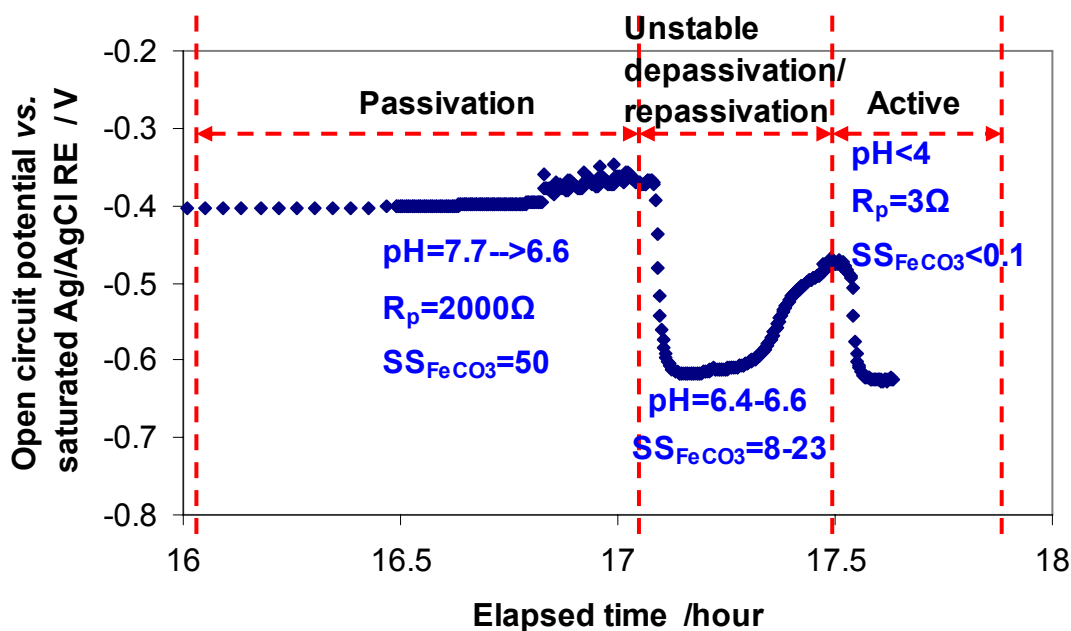


Figure 42. Case 2: relation between supersaturation of $FeCO_3$ and initiation point of passivation at $T=80^\circ C$, $P_{CO_2}=0.53$ bar, $[NaCl]=1\%$ wt, stirring speed 300rpm.

It can be argued that in the previous experiment iron carbonate was near the saturation point and could have dissolved due to slight fluctuations in solution conditions or an error in our ability to predict saturation conditions accurately. To check this possibility, another previously scaled and passivated surface was depassivated by carefully and slowly decreasing the pH as depicted in Figure 42 (called Case 2). In this experiment the steel surface lost passivation in the pH range of 6.4 to 6.6. The subsequent repassivation in the same range of pH clearly suggests this range should be considered the initiation point of the passive film while the calculation of iron carbonate

supersaturation ($SS=8-23$) shows the bulk solution supersaturation value is well above unity. For this condition, iron carbonate that was formed should remain in place.

Repeated observations, including previously described depassivation and depassivation/repassivation, were obtained in the “Case 3” example as shown in Figure 43. Depassivation was evidenced at iron carbonate supersaturation around 8 after pH was decreased from original 7.7 to 6.9. Sustained depassivation was observed in the region of iron carbonate supersaturation from 8 down to 1. These observations confirmed that passivation did not exclusively depend on iron carbonate scale as concluded from previously presented “Case 1” and “Case 2”.

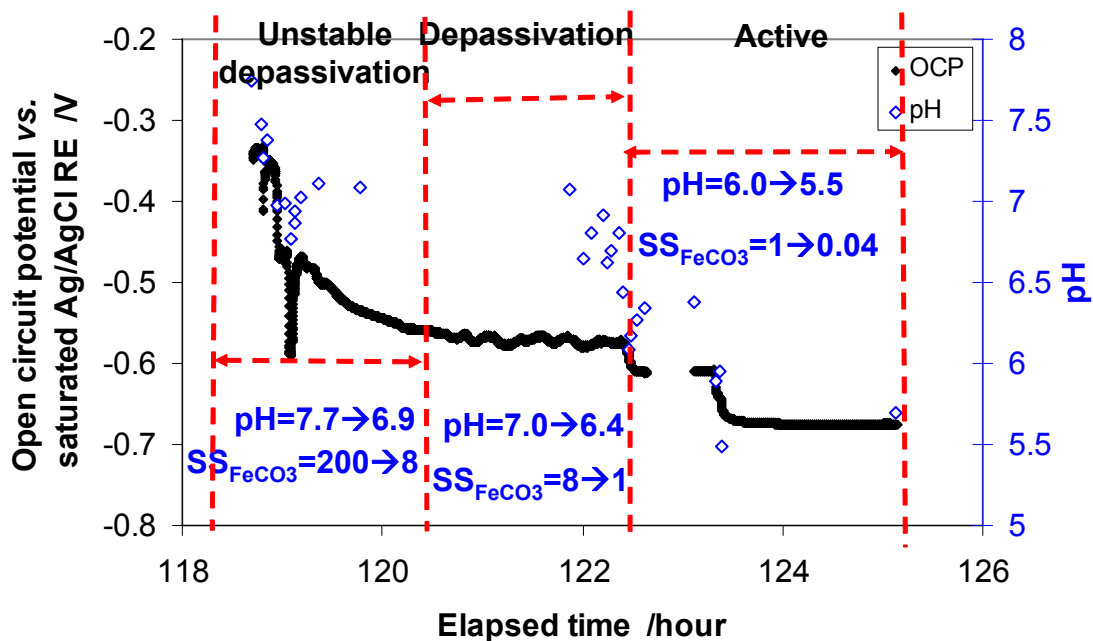


Figure 43. Case3: relation between supersaturation of FeCO_3 , corrosion potential, and depassivation at $T=80^\circ\text{C}$, $P_{\text{CO}_2}=0.53$ bar, $[\text{NaCl}]=1\%$ wt, mildly stirred.

In summary, all the depassivation experimental results clearly confirmed that passivation occurs only after iron carbonate scale was formed however also that depassivation can happen with this FeCO_3 scale intact i.e. while the bulk solution is still supersaturated. This suggests that the passive film in CO_2 environments is not made up only from iron carbonate.

Attention must be drawn to the fact that the polarization resistance increased from 17Ω for the bare surface, corresponding to a corrosion rate 2 mm/yr , to 3000Ω for the passivated surface, corresponding to a corrosion rate of 0.01 mm/yr . After the depassivation, the passive film was lost while iron carbonate scale still remained. The polarization resistance became 360Ω corresponding to a corrosion rate 0.1 mm/y . This observation indicates that protective iron carbonate scale can retard corrosion kinetics somewhat but also demonstrates the super-protectivity of the passive film.

Chapter 4: Chemistry and structure of the passive film on mild steel in CO₂ corrosion environments⁴

4.1 Introduction

Previous chapters have revealed the galvanic mechanism of localized CO₂ corrosion. It was argued that the potential difference between the bare steel anode and the iron carbonate covered cathode drives the localized corrosion propagation. Further investigation discovered a passive film which can be formed under the iron carbonate scale and is responsible for the higher potential on the cathode surface. However, while this passive film was indirectly identified via electrochemical measurements, it is not entirely clear what is the nature and makeup of this passive film. This chapter will present the investigation of the chemistry and the structure of the passive film in CO₂ corrosion.

Grazing incidence X-ray diffraction (GIXRD) is an important characterization method for identification of thin films on a surface. The penetration depth in an asymmetric (2 θ) GIXRD analysis is well controlled and is based on incident angle compared to conventional symmetric (θ/θ) X-ray diffraction.^[81, 82, 83] GIXRD enhances diffraction from the outer thin layer of the analyzed surface, and minimizes diffraction from the substrate.

The transmission electron microscope (TEM) or scanning transmission electron microscope (STEM) can image surfaces at sub-nanometer resolution.^[78] Combining with EDX analysis elemental chemistry information can be obtained.

⁴ This chapter has been published as an ICC 17th conference paper (paper No. 2511) and in *Industrial & Engineering Chemistry Research*, 48 (13), 2009.

In principle, the methodology outlined herein could be applied to study the reactivity of any metal surface. The study outlined in this section shows how GIXRD combined with electrochemical measurements can be used to explain reactivity and corrosion of a mild steel surface in a typical corrosion environment. TEM together with EDX can be used to determine the fine structure and chemistry of complex layered scales. The system involved passive film formation on mild steel in CO₂ saturated electrolyte, a typical sweet corrosion environment.

Generally, passivation can be distinguished from immunity by an electrochemical definition. For noble metals such as platinum and gold, the bare metal surface maintains absolute resistance to corrosion up to relatively high potentials. This differs from what is observed for normally actively corroding metals such as: aluminum and titanium, where corrosion resistance is obtained at higher potentials due to formation of a thin compact passivating film. In this work spontaneous passivation has been observed for mild steel in CO₂ aqueous media as described above.^[57] The conditions correspond to an actively corroding metal under typical CO₂ aqueous environments, as acknowledged by the open literature¹⁸. The process of passivation occurs spontaneously, when compared with passivation artificially achieved by external application of potential or current,^[85, 87] as described in the definition of passivation *vide supra*.

In the literature, ferrous oxide [FeO], ferrous hydroxide [Fe(OH)₂], magnetite [Fe₃O₄] or ferric hydroxide [Fe(OH)₃] have been proposed to be responsible for the passivation of the metal in H₂O–iron environments, under both aerobic and anaerobic conditions.^[85] FeCO₃, also known as siderite, was proposed as a phase which had “the

potential to form passive films” in the $\text{H}_2\text{O}-\text{CO}_2-\text{Fe}$ system by Heuer (1999).^[87] Carbonate containing compounds including $\text{Fe}_2(\text{OH})_2\text{CO}_3$ and $\text{Fe}_2\text{O}_2\text{CO}_3$, were proposed to be passive layer forming by De Marco and coworkers (2007).^[89] Guo and Tomae (1999) observed trace $\text{Fe}_3\text{O}_4 / \text{Fe}(\text{OH})_2$ in the dominant FeCO_3 scale.^[86]

In the current study, phase composition and the structure of the spontaneous passive film formed on mild steel exposed to CO_2 saturated solutions were expected to be identified with the aid of GIXRD and TEM/EDX, in order to help advance the understanding of phenomena that underpin passivation in this corrosion environment.

4.2 Experimental procedures

The spontaneous passivation tests were conducted in a three electrode electrochemical glass cell^[18] as depicted in Figure 23. Mild/carbon steel coupons were used to produce the working electrode. Potential was measured with reference to the saturated Ag/AgCl reference electrode. The counter electrode was made out of a platinum ring. This setup is a universal apparatus for electrochemical study of metal reactivity, at ambient pressure and temperatures that do not exceed solution boiling points.

Sodium chloride electrolyte (1 wt. %) was prepared, heated to 80°C and deaerated with sparging by carbon dioxide. The pH of the solution was adjusted to pH 8.0 by addition of solid NaHCO_3 (ACROS, ACS analytical grade 99.7%) in order to speed up the formation of FeCO_3 scale and passive film. Mild steel, X65 (composition shown in Table 6), corrosion coupons were polished sequentially by 200, 400 and 600 grit silicon carbide abrasive paper. This sample was used for GIXRD/XRD analysis. The sample

used for TEM/EDX analysis was similar – carbon steel C1018 (composition shown in Table 5). During sample cross section preparation for TEM, the sample was finished with 1 μm diamond paste. During polishing the coupons were simultaneously cooled by flushing with 2-propanol, then ultrasonicated in 2-propanol and blow dried. The coupons were prepared as describe in Chapter 3. The test conditions are listed in Table 10 under pH=8, T=80 C and 1 wt% NaCl saturated with CO₂. The corrosion resistance was measured using the Linear Polarization Resistance (LPR) technique *via* a Gamry Inc. PC4 potentiostat.

Table 10. Test matrix for the passivation experiments

Material	C1018, X65
Temperature /°C	80
pH	8.0
Purged Gases	CO ₂
NaCl concentration / wt%	1
Flow conditions /rpm	300 (stirring bar)
Gas partial pressure /bar	0.53

After a very brief period of bare steel surface corrosion, solid FeCO₃, was the initially formed corrosion product at the steel surface. The open circuit potential decreases as this diffusion barrier develops. The corrosion rate also decreases due to surface coverage by this scale which limits the supply of the corrosion reactants. Subsequently spontaneous passivation was achieved as evidenced by the increased open circuit potential.⁵⁷ The spontaneous passivation potential could be up to 400 mV higher

than the initial open circuit potential for the bare metal surface. Coupons were removed from solution before and after passivation, as identified by differences in the measured corrosion potentials. They were immediately flushed with 2-propanol to dehydrate them until they cooled from 80°C to room temperature, in order to avoid oxidation of wet films at elevated temperature. If salt precipitation (NaHCO_3 or NaCl) was observed on coupon surfaces during the cooling and drying process, they were quickly rinsed with CO_2 deaerated deionized water, then immediately flushed with 2-propanol. This removed any deposited salts and water from the surface. Any remaining 2-propanol was blown from the surface with dry air. Samples were then stored in desiccators under a nitrogen atmosphere prior to analysis. The sample surface was analyzed by XRD and GIXRD using a Rigaku Ultima III X-ray diffractometer.

(S)TEM with EDX analysis was done on a FEITecnai F20 with an EDAX EDX unit. The FEI TIA software was used to collect EDX spectral profiles. The cross-section of the surface was prepared using standard Focused Ion Beam (FIB) techniques using *ex-situ* liftout (Figure 44 a-d). To improve conductivity, the sample was coated with gold; a thick layer of platinum was deposited to both smooth the FeCO_3 surface and protect the cross-section during the FIB milling process. After thinning to electron transparency (Figure 44 a), the cross-sectional membrane was lifted out of the trench (Figure 44 b,c,d) and placed on a 20nm carbon support film on a copper TEM grid.

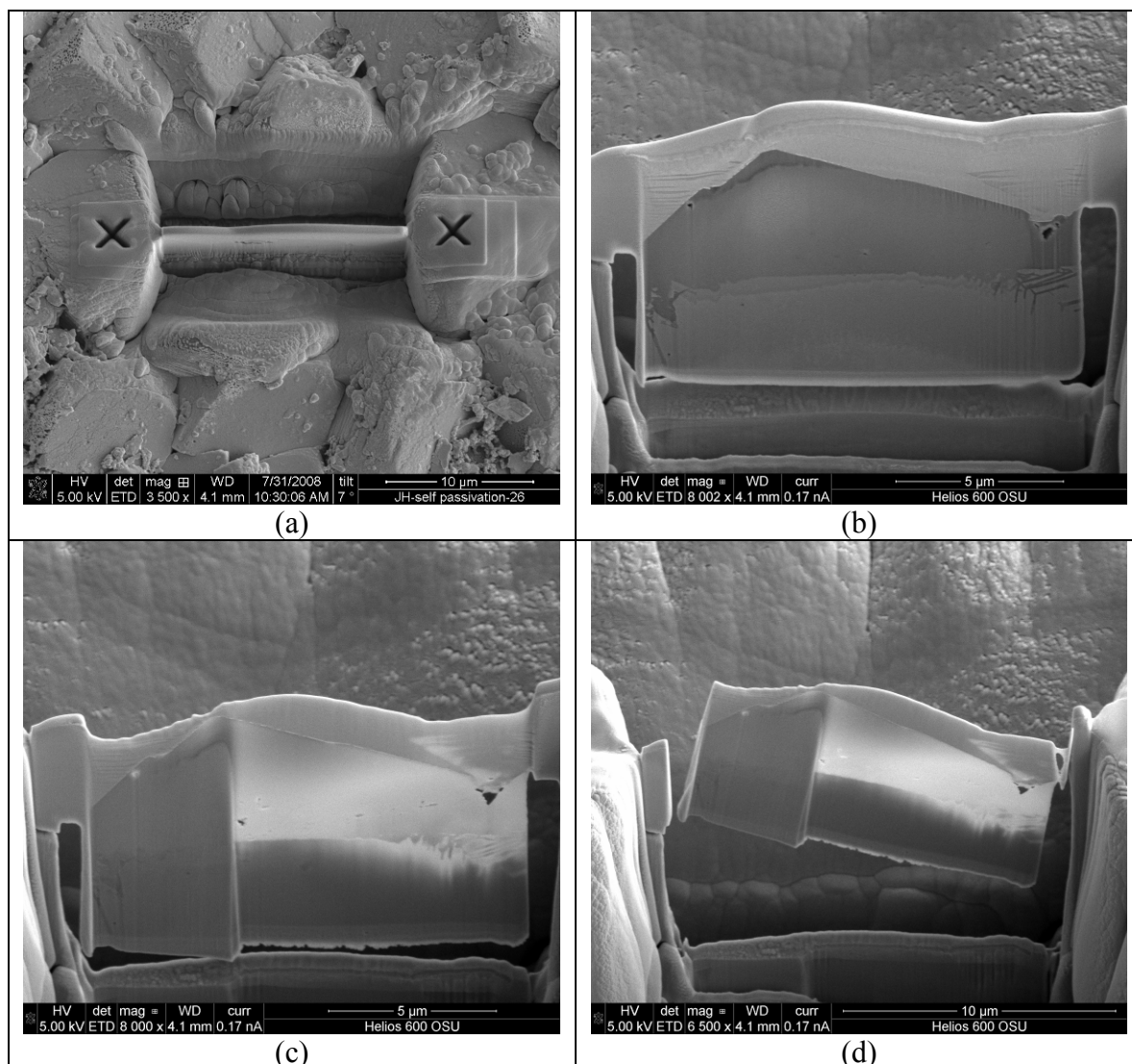


Figure 44. A crystal slice was cut from the bulk surface by FIB.

4.3 Results and discussion

4.3.1 Spontaneous passivation

The passivation process as indicated by the slower corrosion rate and the open circuit potential history sample during spontaneous passivation is depicted in Figure 45 and Figure 46. The open circuit potential steadily increased to a -450 mV.

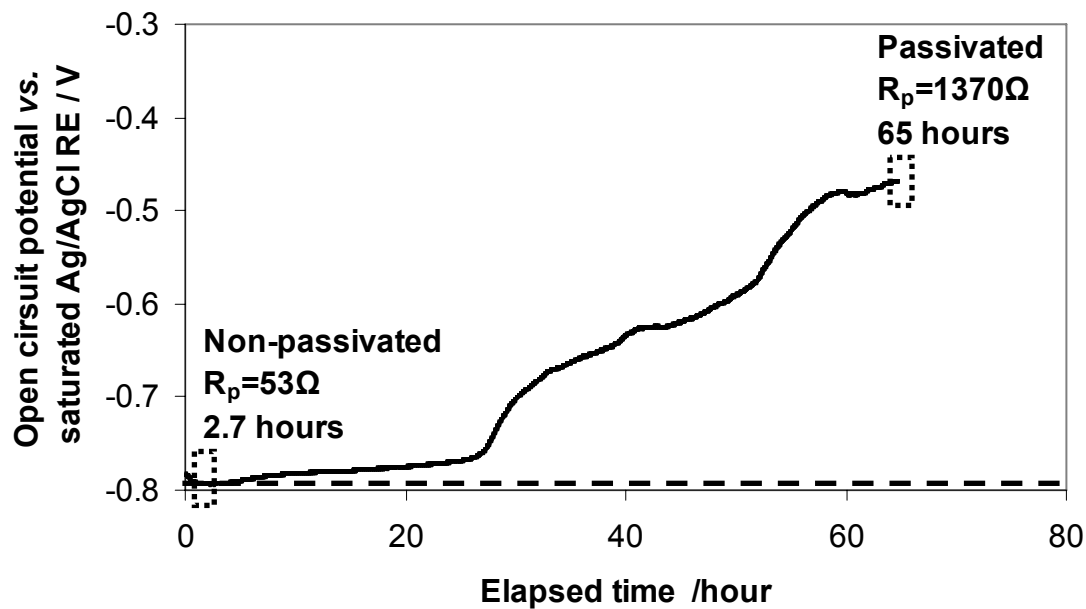


Figure 45. Open circuit potential history for spontaneous passivation.

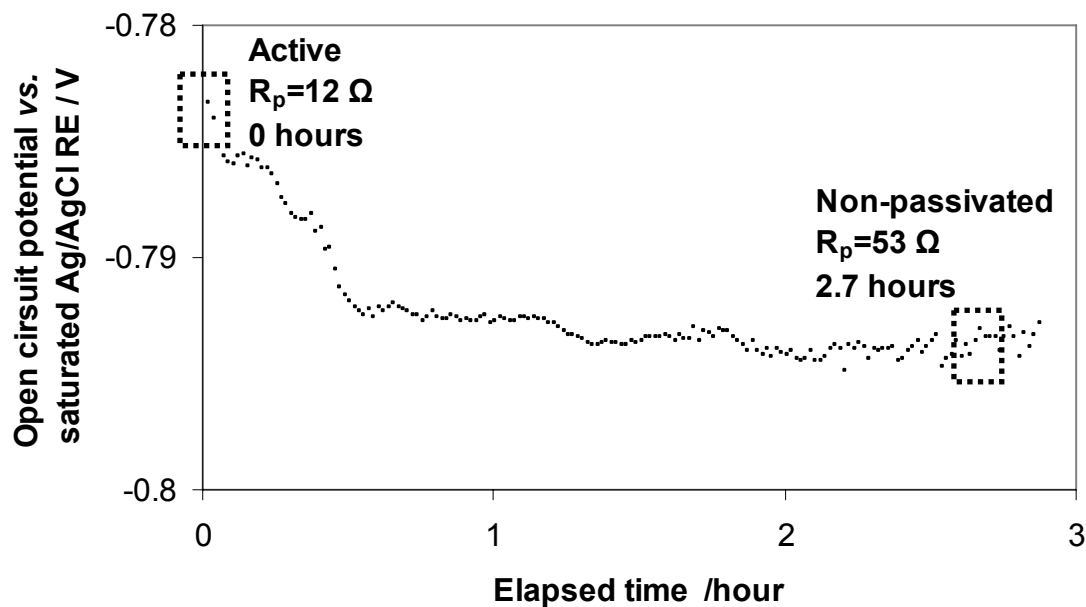


Figure 46. Open circuit potential history during initial FeCO_3 formation before passivation.

After *ca.* 60 hours of immersion, spontaneous passivation is observed as indicated by an open circuit potential increase ^[57] as depicted in Figure 45. The open circuit potential increases to a value of -0.470 V vs. reference electrode and the corrosion resistance further increases to 1370 Ω . This corresponds to a passivated surface.

Coupons were prepared for XRD and GIXRD analysis before and after passivation (2.7 and 65 hours immersion, respectively), as indicated by the boxes in Figure 45.

4.3.2 XRD and GIXRD analysis results

4.3.2.1 Conventional X-ray diffraction

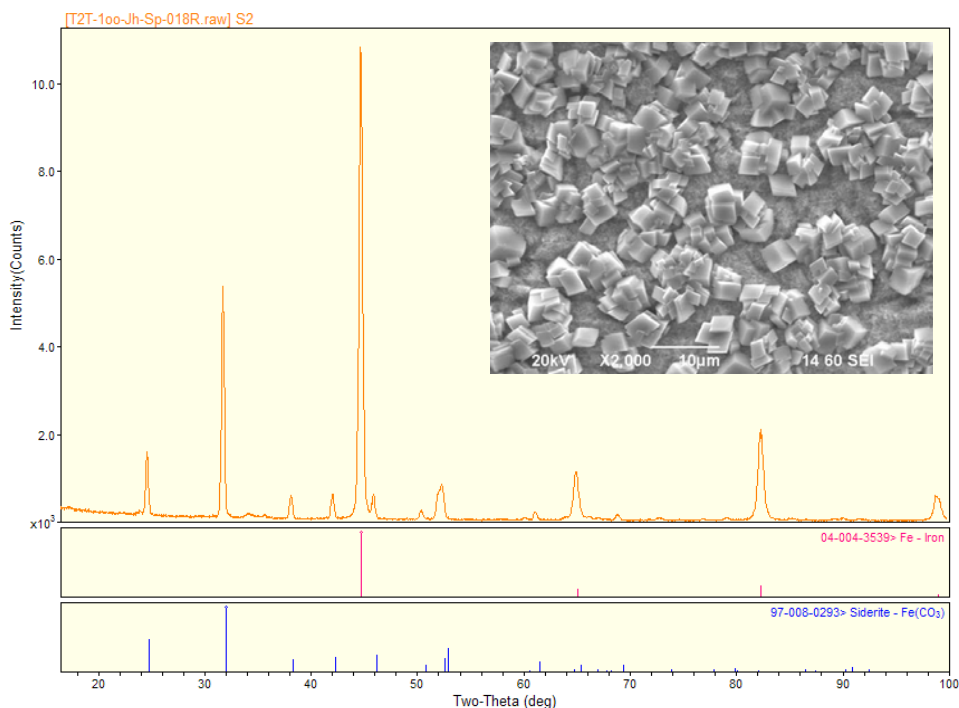


Figure 47. XRD and SEM of non-passivated steel surface after 2.7 hours immersion.

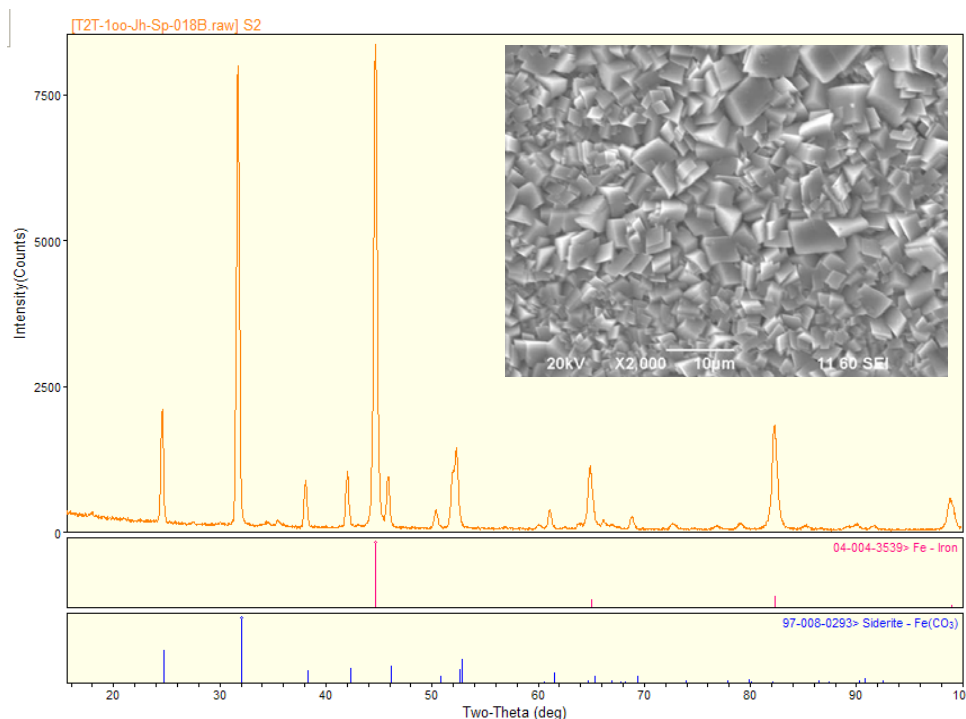


Figure 48. XRD and SEM of passivated steel surface after 65 hours immersion.

Acquired energy dispersive X-ray fluorescence (EDX) spectra were consistent with the formation of iron carbonate crystals. The continuously increasing incidence angle results in deeper penetration into the substrate beneath the film. Thus a strong diffraction signal from the substrate steel is observed.

4.3.2.2 *Grazing incidence X-ray diffraction*

XRD with grazing incidence was employed together with the SEM to more thoroughly determine the identity of the passive film. Both SEM images before and after passivation show that the top phase is iron carbonate. The GIXRD from the sample before passivation shows that only iron carbonate peaks are present, as shown in Figure

49. The diffraction pattern only represents the outer layer, therefore diffraction from the steel substrate has been eliminated. This can be seen by comparison with Figure 47 and Figure 48.

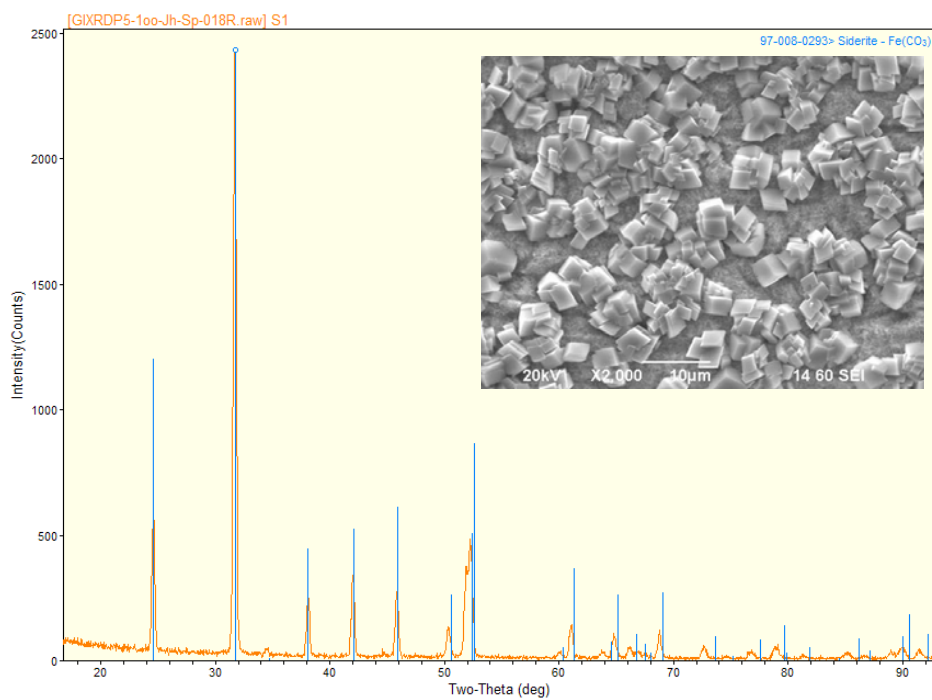


Figure 49. GIXRD and SEM of non-passivated steel surface after 2.7 hours immersion.

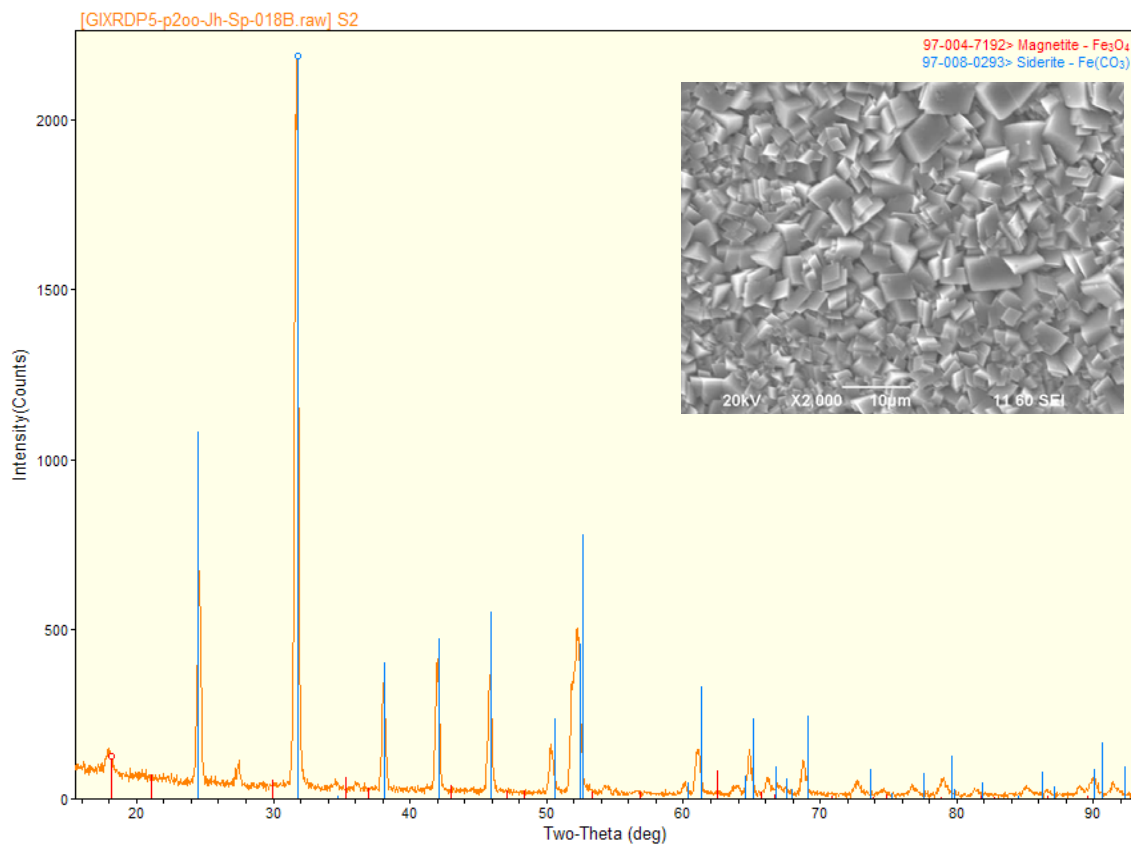


Figure 50. GIXRD and SEM of passivated metal surface after 65 hours immersion.

After the sample was passivated, an extra phase Fe_3O_4 (magnetite)^[90] along with the dominant FeCO_3 ^[91] was identified by GIXRD (Figure 50). The composition of the film was quantified using the Rietveld refinement technique.⁹² For this, the program Whole Pattern Fitting (WPF) incorporated in diffraction data analysis software JADE8.5 was utilized. A reasonable composition with 0.4 wt% of magnetite (Fe_3O_4) and 99.6 wt% of siderite (FeCO_3) was obtained. It is therefore hypothesized here that Fe_3O_4 could be the composition of the thin passive film encountered in this environment. Since passive films typically have a thickness on the nanometer scale they were difficult to observe using the conventional X-ray diffraction.

4.3.3 TEM/EDX analysis results

An image of the cross-sectional sample is shown in Figure 51. This is a High-Angle Annular Dark-Field (HAADF) STEM image where the brighter areas correspond to increased scattering of the electrons. At the top of the sample are the Pt protective layer and the gold conductive coating. Because it has a lower average atomic number, the carbonate layer is darker than the iron substrate. The interface between the iron and the iron carbonate appeared rougher at the iron grain boundaries than within the grain.

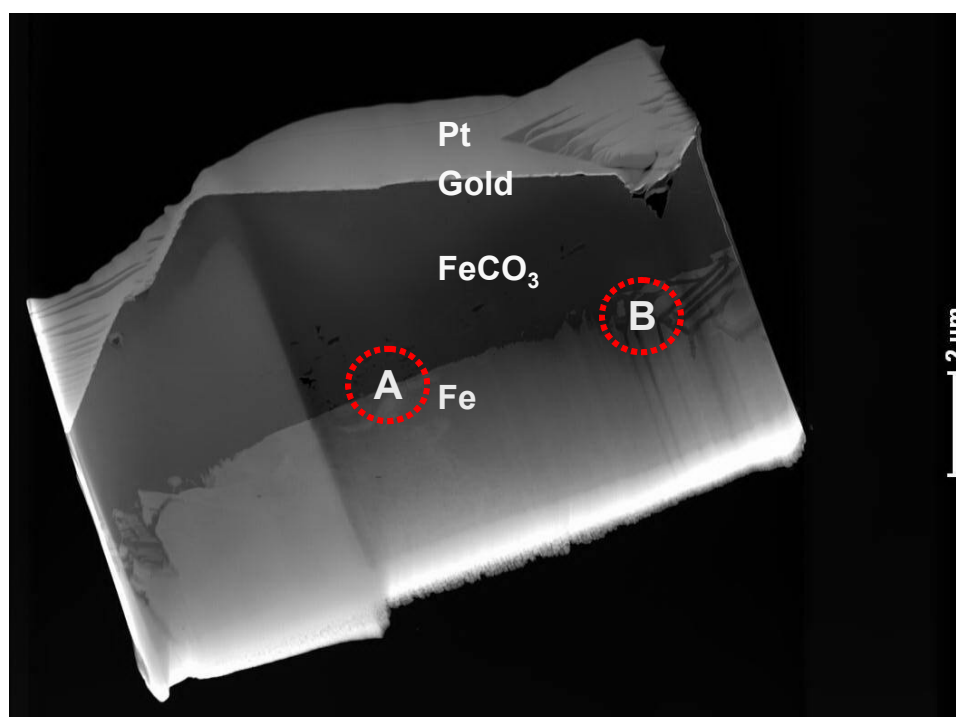


Figure 51. HAADF STEM image of a sample with circled surface **A** and **B**.

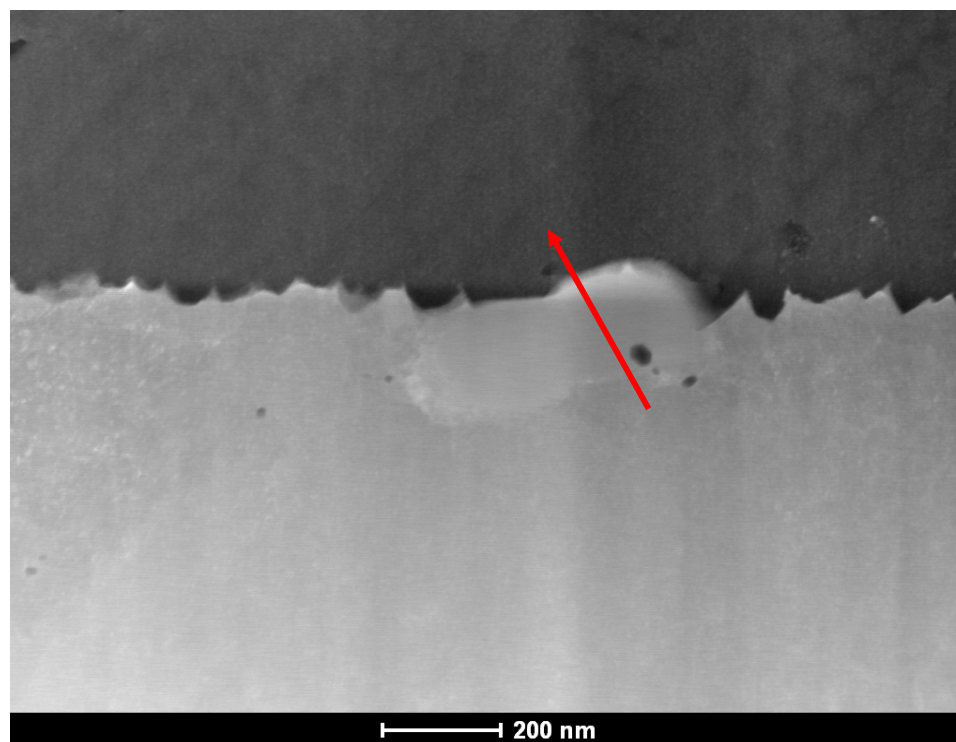


Figure 52. HAADF STEMEM image of circled area A in Figure 51 with EDX element profile indicated.

The detail from the center of the grain (location A) is shown in Figure 52. A different phase is apparent as demonstrated by a whiter color compared with steel and ferrous carbonate phase, so an STEM EDX profile was carried out using EDX at a scan step of 20 nm. The scan started from the steel substrate, went through the unknown phase and ended at the ferrous carbonate phase as indicated by the arrow. Figure 53 shows the EDX peak intensity profile. Because elemental quantification for light elements such as carbon and oxygen is problematic, we present only the peak intensities. Compared with the Fe phase, the intensity of the oxygen signal doesn't change while carbon counts increase slightly in the unknown phase. This suggests very little oxygen in the unknown phase with carbon and iron being the primary components. Comparing the

unknown and FeCO_3 phases indicates the unknown phase has more iron, about the same carbon and less oxygen than the FeCO_3 . We conclude that this phase is probably iron carbide (Fe_3C) which was exposed as the iron from the parent steel corroded away.

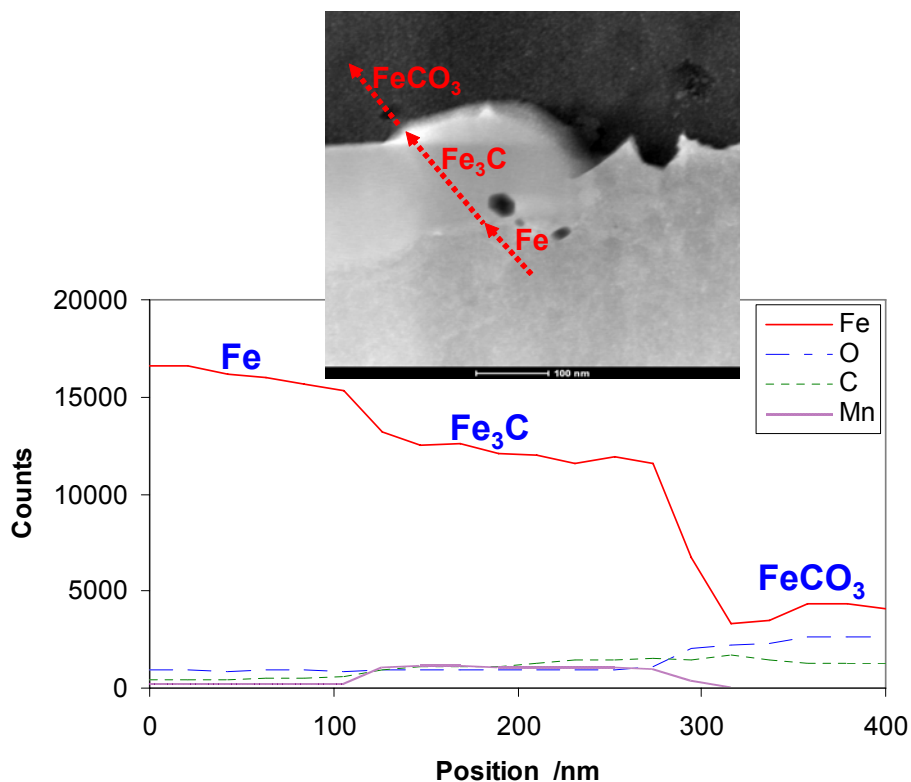


Figure 53. EDX element profile of different phases for Figure 52. Note: unknown element determined to be iron carbide (Fe_3C).

At steel grain boundary (area **B** in Figure 51), a much rougher interface is observed as compared with the middle part of the grain (area **A**). EDX analysis on area **C** of Figure 54 indicates the presence of manganese.

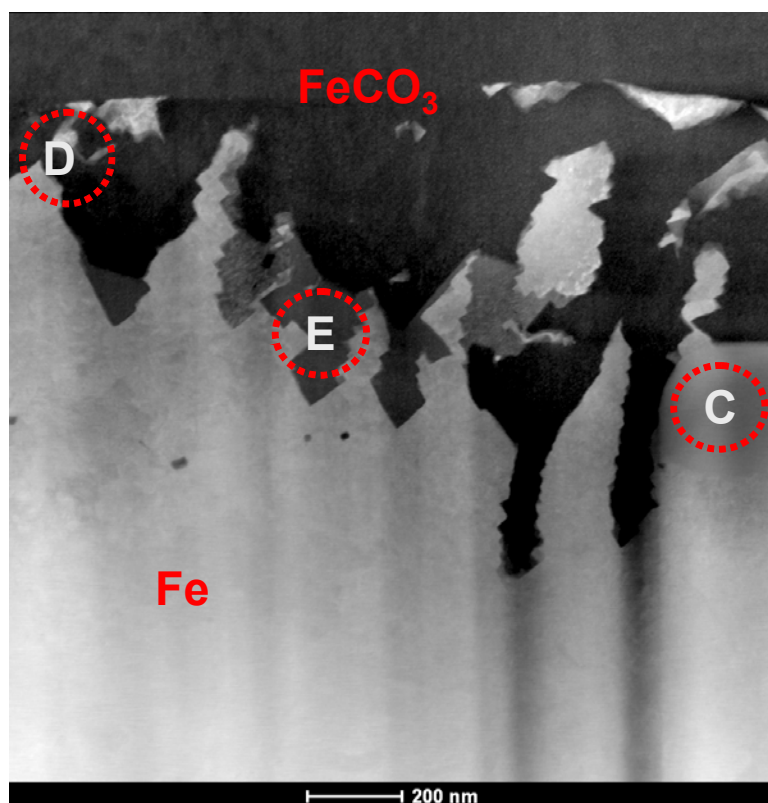


Figure 54. The TEM image of edge surface of area **B** in Figure 51 with designated areas **C**, **D** and **E** for analysis.

An EDX profile scan was done in area **D** of Figure 54 (cf. the image at the top of Figure 56). As the scan steps from steel into the iron carbonate phase, higher levels of carbon and oxygen in any carbonate containing phase should be seen. The iron level in the iron carbonate should be lower than in the steel phase. The EDX results in Figure 56 clearly show these trends. A number of phases appear in area **E** as indicated by a grey color as compared with dark FeCO_3 and white iron phases. The thickness is estimated between 20-100 nm. To identify this phase, EDX scanning to profile elements was executed as indicated by the TEM image at the top of Figure 57. Compared with pure steel phase, an obvious increase of oxygen and decrease of iron levels are observed in the

unknown phase as shown in Figure 57. The carbon level is constant in both phases. This compositional relationship between carbon and oxygen rejects the hypothesis that the passive film is a carbonate containing phase. All the above information clarifies that the passive film is a carbonate containing phase. This observation qualitatively agrees with the GIXRD results suggesting that the passive layer is magnetite (Fe_3O_4). The TEM images show that this passive film is not a continuous film covering the steel surface, but is primarily located at the boundaries between the FeCO_3 crystals. Note that the positions of the peaks and troughs for the Fe and O coincide with the different contrast regions on the TEM. This technique cannot detect hydrogen, so it cannot be used to identify the presence of any hydroxides.

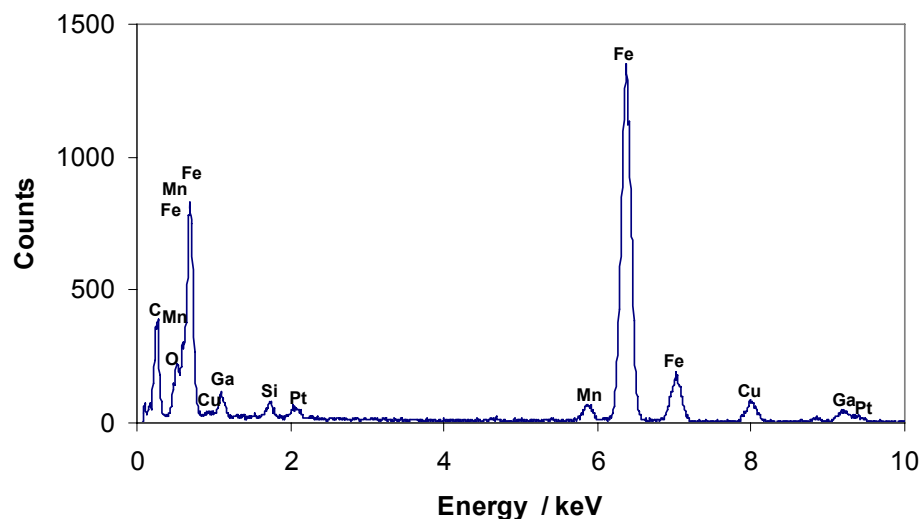


Figure 55. Alloyed element Mn is observed by EDX on area C in Figure 54.

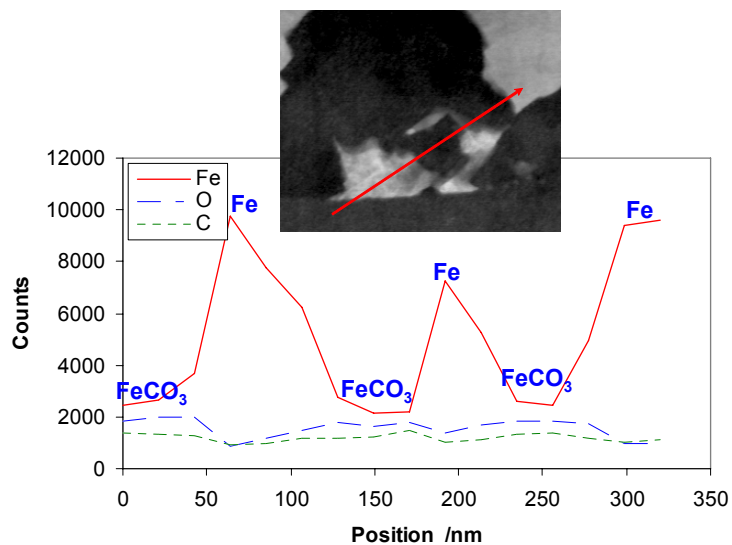


Figure 56. Element profile at different phases for area **D** in Figure 54. EDX directional scan indicated in TEM image.

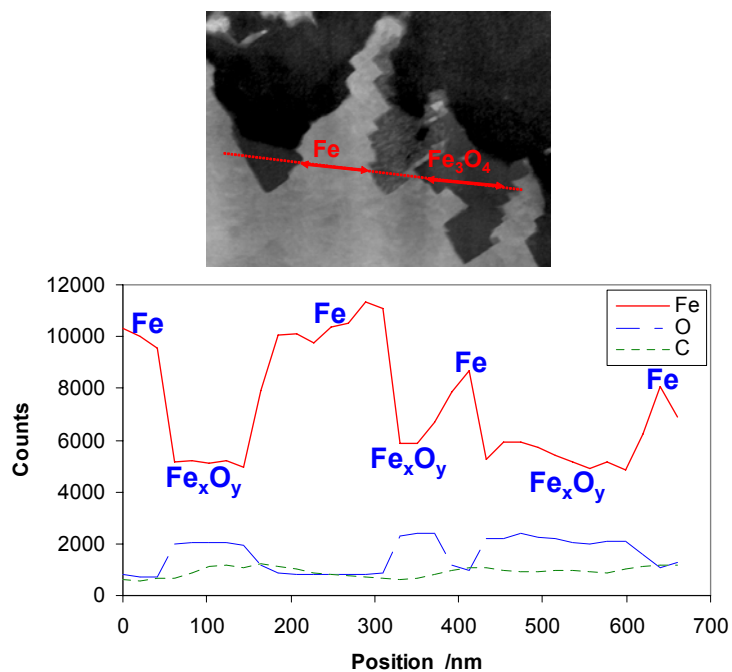
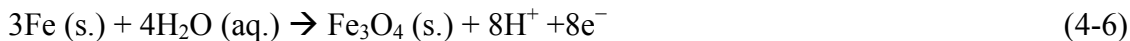


Figure 57. Element profile at different phases for Area **E** in Figure 54. EDX directional scan indicated in TEM image.

4.4. Passivation scenario for mild steel in CO₂ environments

From previous and current results it is possible now to propose a more complete mechanism of passivation of mild steel in CO₂ environments. As the steel is immersed with CO₂ aqueous electrolyte, given a high enough pH, iron carbonate can be formed when surface FeCO₃ supersaturation is achieved. As the iron carbonate scale becomes compact, it retards replenishment of protons which are consumed by corrosion at the steel surface; therefore a higher local (surface) pH can be achieved. When it reaches a critical pH for iron oxide formation, a passivating magnetite phase is speculated to be formed as follows:^[93]



This is shown schematically in a simplified Pourbaix diagram^[85] in Figure 58.

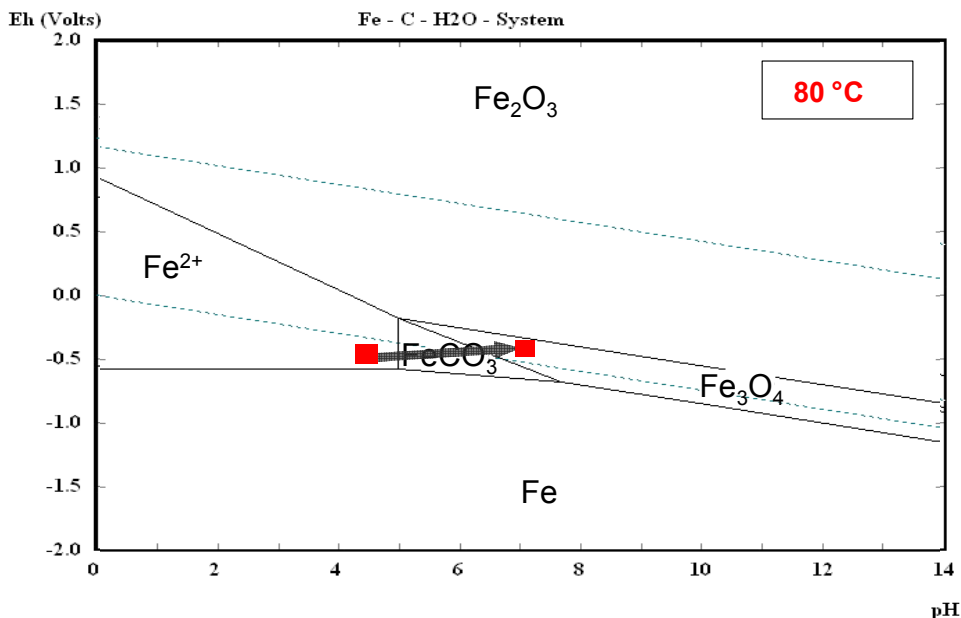


Figure 58. A Pourbaix diagram showing an increase of pH and consequently potential beneath a FeCO₃ scale leading to passivation.

Chapter 5: Mesh-capped probe design for direct pH measurements at an actively corroding metal surface⁵

5.1 Introduction

The mechanism outlined above still hinges one logical but still unproven assumption: that the local pH at a corroding steel surface, and particularly the pH underneath an iron carbonate layer, will be higher than that of the bulk. Actually it was assumed that this pH will be high enough to cause passivation of the mild steel surface. This section presents results of experiments which were done to explicitly test this hypothesis and complete the proposed mechanism of localized CO₂ corrosion.

It is well known that local surface chemistry conditions can be very different than those in the bulk and become important when chemical reactions occur at an interface.^[56, 57] Surface pH is long recognized as a key local parameter that influences electrochemical reaction mechanisms and rates^[58, 62]. Mathematical modeling, based on thermodynamic, kinetic and transport theories, has helped in the quantification of surface pH conditions^[23, 94]. However, not much has been achieved in terms of direct surface pH measurement at a corroding surface due to difficulties with probe design, manufacturing and operation. The objective of the present undertaking hinged on an effective design and deployment of a simple and flexible surface pH probe for direct measurement of surface pH at a corroding surface.

The existing designs outlined in the open literature typically deployed direct or indirect measurement methods, as summarized in Table 11, and are briefly reviewed below.

⁵ This chapter has been published in Journal of Applied Electrochemistry.

Table 11. Surface pH measurement methods

Methods		Application
Indirect	Chemical indicator (e.g. photocurrent–pH plot) ^[97, 98]	Electrolysis
	Rotating ring disc electrode ^[99]	Electrolysis
Direct	Standard pH probe ^[96]	Corrosion
	Microelectrode ^[108–114]	Corrosion, Electrolysis
	Mesh capped flat pH probe ^[100–107]	Electrolysis

5.1.1 Indirect surface pH measurement probe design

Some surface pH probe designs have been previously reported for indirect pH measurements during the electrolysis processes. One is a pH-mapping technique ^[97, 98] where a semiconductor contacts the solution and responds to the pH due to depletion of its insulating layer. The resulting capacitance change can be recorded with a generated photocurrent. This design is relatively complex, and involves elements which are not easy or cheap to obtain or manufacture. Another indirect method is surface pH measurement using a rotating ring electrode ^[99]. This technique is based on the pH-potential relation as defined by the Nernst equation and does not lend itself easily to extension to different corroding systems.

5.1.2 Direct surface pH measurement probe design

In some early research, standard pH probes were modified for direct surface pH measurement. D. M. Dražić ^[96], for example, coated a standard pH probe with a porous

silver film used as a substrate for electrochemical deposition of iron. This probe was then applied to surface pH measurement during iron surface dissolution (corrosion). Disadvantages for this design (which was initially attempted in the present work) include its fragility as well as a host of issues related to the intricacies of its fabrication and operation.

A very commonly used direct surface pH measurement device is a pH microelectrode specially designed for surface pH measurement ^[108-114]. Microtips, typically ranging from 1 to 20 μm in diameter ^[109], have been fabricated as the sensing elements of microelectrode pH probes; these have been applied in corrosion surface pH measurement ^[108, 111] as well as diffusion layer pH profiling. ^[109, 110, 112, 113] A major shortcoming of this design is that it interferes with the mass transfer boundary layers near the solid surface.

Another direct surface pH probe design was reported for electrolysis systems by Romankiw ^[100, 101]. The prototype design consists of a flat sensor pH probe with a tip which is adhered to a metal mesh. During the corrosion of the mesh, surface pH can be monitored. This surface pH probe design was further modified for rotating ^[102] or fixed ^[103, 104] metal meshes. Particular applications were reported for surface pH measurement during jet impingement tests ^[104], electrodeposition ^[105, 106] and electrochemical reduction reactions ^[107]. This surface pH probe design concept was adopted as a starting point for the present design.

5.2 Experimental

5.2.1 *Experimental design and setup*

A simple probe design for surface and interfacial pH measurement was developed as shown in Figure 59. The pH sensor used is a commercial flat pH glass probe. A compression fitting is employed to hold the pH probe body in place. A circular mild steel mesh is cut to match the size of the hollow compression fitting cap. This cap is used to push the mesh into tight adherence with the probe tip. This surface pH probe unit is inserted into the solution and the surface pH can be measured during the corrosion of the mild steel mesh. If needed, particulate materials used to simulate corrosion deposit layers can be filled in the cap and held trapped in place by another non-corroding mesh material (e.g., the stainless steel in the current study).

The advantage of this design is its simplicity, portability, low fabrication cost and flexibility. The mesh can be easily mounted, removed and replaced. It can be easily deployed to determine surface pH measurement under electrochemical control by electronically connecting the mesh to a measurement instrument. The mesh can be easily obtained or manufactured out of most metals of interest, active, passive or noble, for corrosion studies, electrolysis, catalysis, etc. Consequently, any set of heterogeneous reactions can be characterized in terms of metal surface pH. Application of this mesh-based electrode design could easily be extended to non-redox systems.

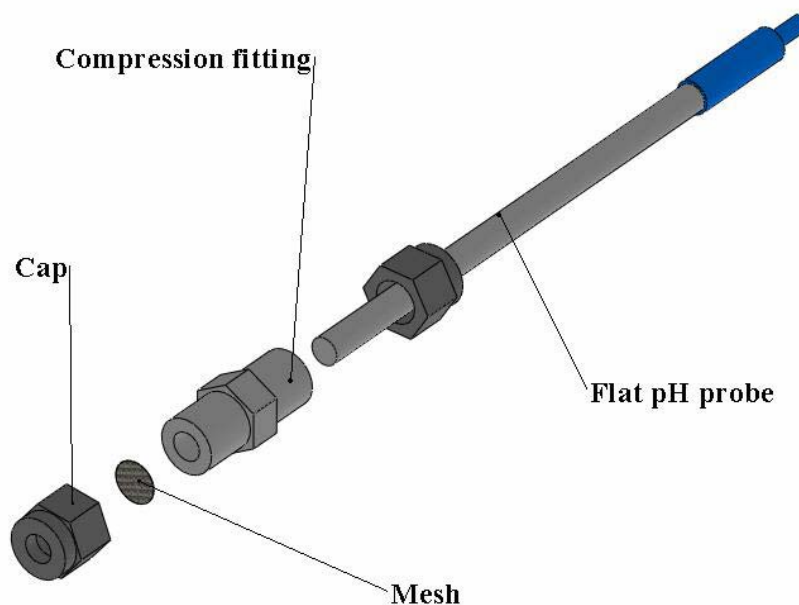


Figure 59. Surface pH probe design.

Table 12. Mild steel mesh data

Steel type	Mild steel
Form	Woven wire cloth
Mesh size	60 x 60 holes/in ²
Square size	0.009"
Wire diameter	0.0075"
Mesh open area	30.5%

In this study, the circular 3600 holes/inch² mild steel mesh was cut from a larger commercially available stock, to completely cover the pH probe surface. Details about the mild steel mesh used in the tests are listed in Table 12. The SEM images of an original single sheet mesh and a “double sheet compressed” mesh are depicted in Figure

60. The compressed mesh was produced in order to reduce the mesh pore size and investigate if this has an effect on the performance of the probe.

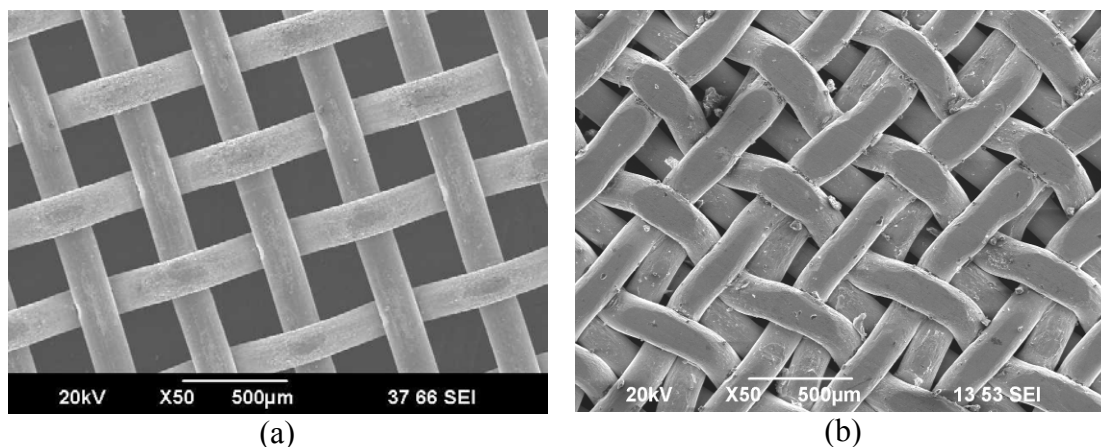


Figure 60. SEM images of (a) single sheet mesh, (b) double sheet compressed mesh.

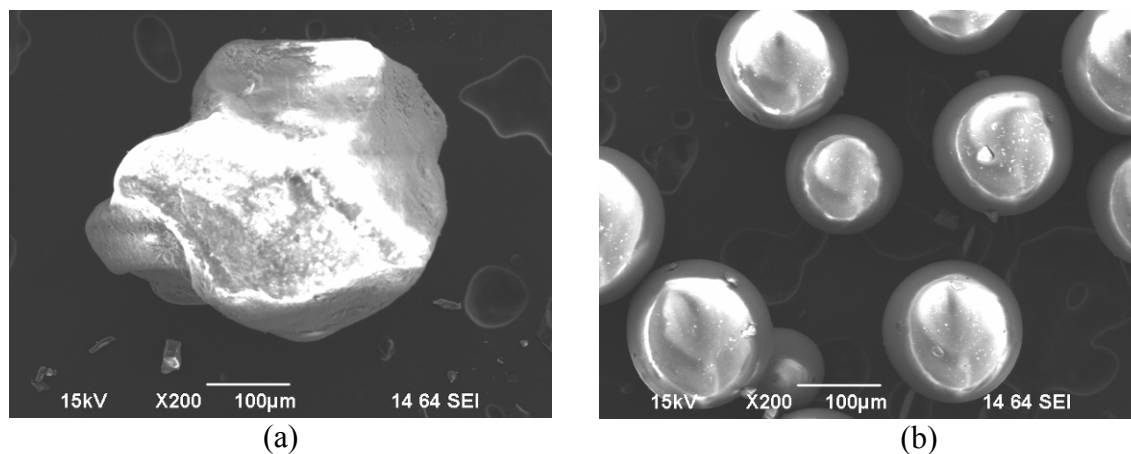


Figure 61. The images of particles used to create the deposit (a) typical sand particle (size: 100–500 μm), (b) glass bead particles (size: 50–80 μm).

The particles used to simulate the deposit layer were inert sand and glass beads, as shown in Figure 61. The particle size for the sand ranged from 100–500 μm giving a bulk layer porosity of approximately 40%. The smaller sand particles were 50–80 μm in

size giving a bulk layer porosity of about 30%. Both were deposited in the form of a layer of 5 mm in thickness.

The meshed pH electrode was deployed in a standard three-electrode corrosion glass cell, as depicted in Figure 62, filled with an aqueous solution. In this case the measurements were performed under quiescent conditions. In different arrangements, flow can be readily created by other means (e.g., by flush mounting the probe at a pipe wall or a flow channel wall, using a jet impingement setup, etc.). All these alternatives appear to be easier than rotating the metal mesh, as was done by Romankiw^[102].

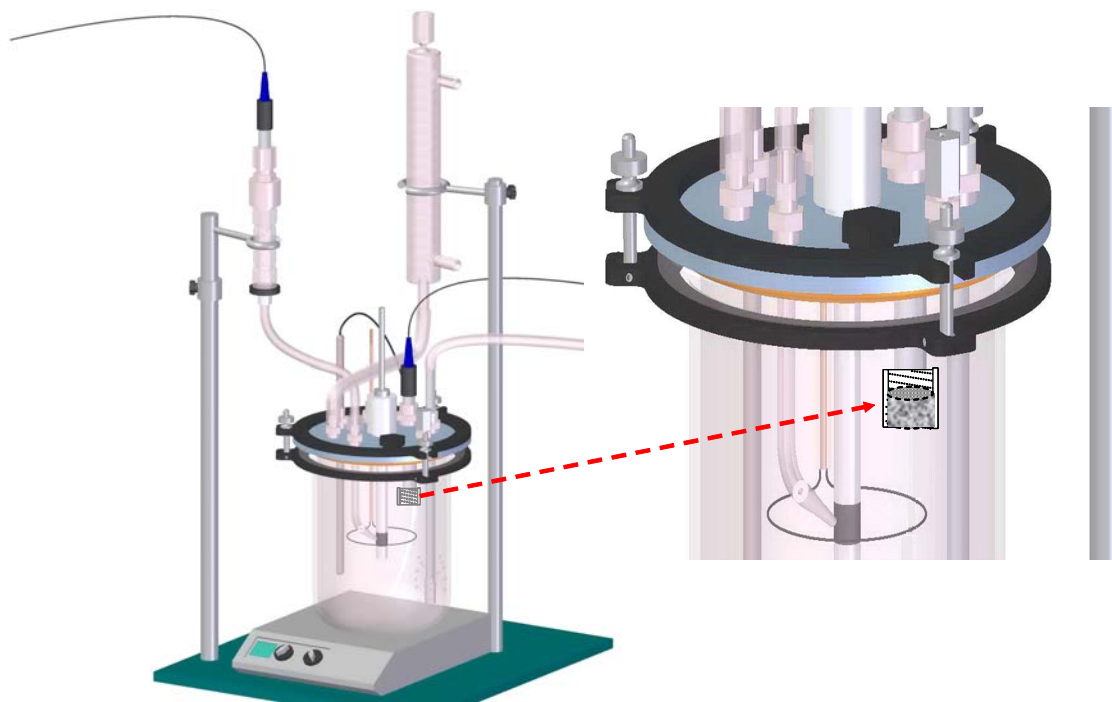


Figure 62. Surface pH measurement setup deployed in a standard three-electrode electrochemical glass cell.

5.2.2 *Experimental test matrix and procedure*

The test matrix for surface pH measurements is listed in Table 13. The effects of bulk pH, buffer capacity, temperature and surface layer porosity (achieved by using different particle sizes) were investigated.

Table 13. Test matrix for the surface pH experiments

Mesh material	C1018 mild steel
Deposit particle material	Sand, glass bead
Depth of the deposit layer /mm	5
Solution	CO ₂ -H ₂ O, Cl-H ₂ O, HAc-H ₂ O
Purge gas	N ₂ , CO ₂
Temperature /°C	25, 80
Gas partial pressure /bar	0.97, 0.53
Bulk pH	4.0, 5.0, 6.0, 6.6
NaCl concentration / wt%	1
Test period /hour	10

A 1 wt% NaCl electrolyte solution was first deaerated by purging with CO₂ or N₂ in different experiments. Solution pH was adjusted with deaerated 1M NaHCO₃ or 0.1M HCl solutions as well as acetic acid when appropriate. Temperature was controlled at 25°C and 80°C. The corresponding partial pressures of CO₂ are 0.97 bar and 0.53 bar given that the cell operated at atmospheric pressure.

Two pH probes, including a standard pH probe and a flat pH probe (fabricated for surface pH measurement), were first calibrated with standard buffer solutions at 4.00±0.01, 7.00±0.01 and 10.00±0.01 pH units. The standard pH probe was then used to

measure the bulk pH of the solution and the flat pH probe with the mild steel mesh was used for surface pH measurement. The steel mesh was first cleaned by immersing it in deaerated 0.1 to 0.5 M HCl solutions for about 10 minutes, or until oxidation products were removed and a shining metal mesh surface was produced. The mesh was then washed in isopropanol to dehydrate it and blown dry. It was mounted on the flat pH probe and tightened to the pH tip with the compression fitting cap holder. To measure the surface pH under a deposit layer, the small particles were filled as described in the design section above. Both pH probes were immersed in the corrosive solution. The steel mesh corroded and the surface pH could be monitored and compared with the bulk solution pH.

5.3 Results and discussion

The meshed surface pH probe was used to measure the surface pH for mild steel corroding in different water chemistry conditions:

CO₂ saturated solution.

N₂ saturated HCl solution.

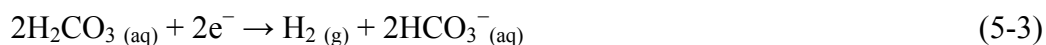
N₂ saturated HAc (acetic acid) solution.

From theory, the corrosion reactions for these environments can be summarized as two series of half cell reactions: cathodic and anodic. The cathodic reactions in strong acid electrolytes, e.g., HCl solutions, are:^[18]



The transport of reacting species from the bulk is often a limiting factor in these situations. For example, protons are consumed on the steel surface by a fast electrochemical reaction (5-1) and a decreased proton concentration, *i.e.*, a higher pH, is expected on the surface compared to the bulk value.

If weak acids, *i.e.*, carbonic acid (H_2CO_3 obtained by hydration of dissolved CO_2) or acetic acid (HAc), are present, additional cathodic reactions need to be considered such as: [18, 22]



The dominant anodic reaction is the oxidative dissolution of iron:[18]



It should be remembered that the two weak acids will partially dissociate to produce more protons and decrease the pH:



5.3.1 *Validity and reproducibility of measurement using the surface pH probe*

An initial series of experiments was conducted to confirm proper performance of the new pH probe. Figure 63 shows two sets of experiments conducted at 25°C at bulk pH 4.0, in a CO_2 saturated electrolyte using a mild steel corroding mesh. After initial variation, a stable surface pH was measured which is approximately 1.5 pH units higher than the bulk pH. This translates into a surface proton concentration 50 times less than the bulk concentration, as calculated.

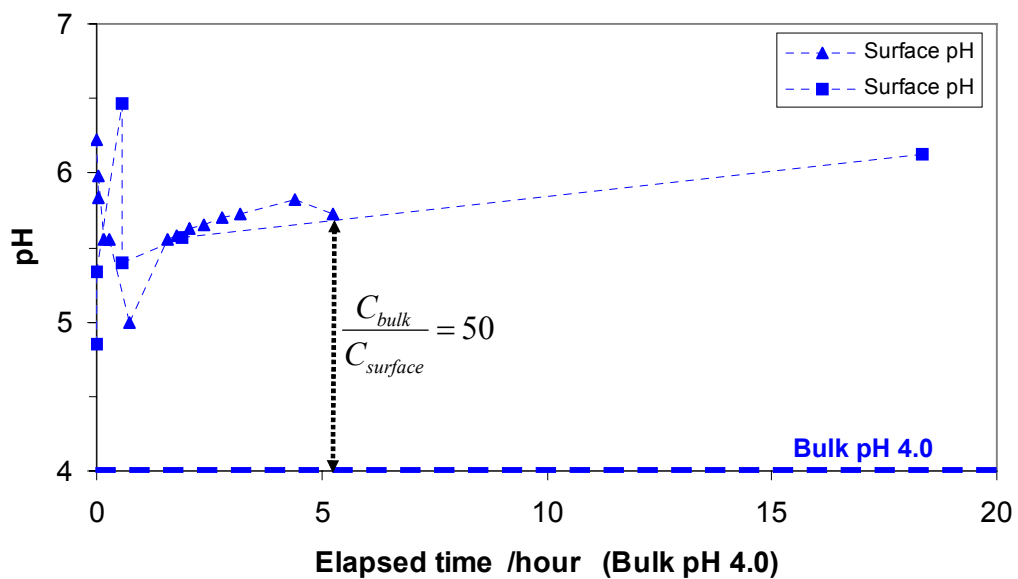


Figure 63. Two series of surface pH measurements during mild steel mesh corrosion in a CO_2 purged solution at bulk pH 4.0, $T=25^\circ\text{C}$, $p_{\text{total}}=1\text{bar}$, $P_{\text{CO}_2}=0.97\text{bar}$, $[\text{NaCl}] = 1\text{wt}\%$.

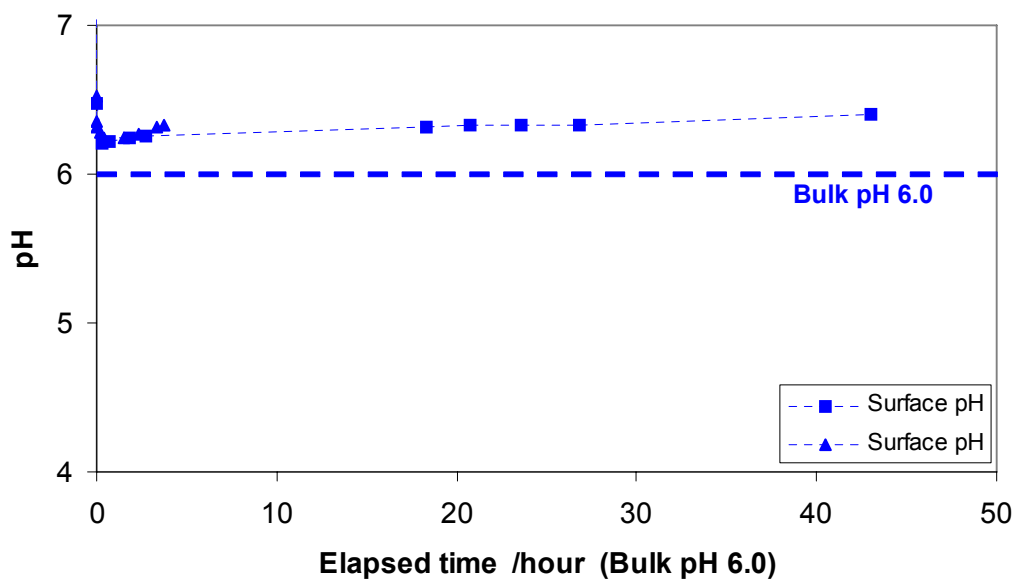


Figure 64. Surface pH measurements during mild steel mesh corrosion in a CO_2 purged solution at bulk pH 6.0, $T=25^\circ\text{C}$, $p_{\text{total}}=1\text{bar}$, $P_{\text{CO}_2}=0.97\text{bar}$, $[\text{NaCl}] = 1\text{wt}\%$.

Similar observations were shown in Figure 64 for the bulk pH 6.0, even if the pH increase was not as large. Good reproducibility is obtained, which is within 0.1 pH units. This is considered to be in the error range of the pH probe measurement system.

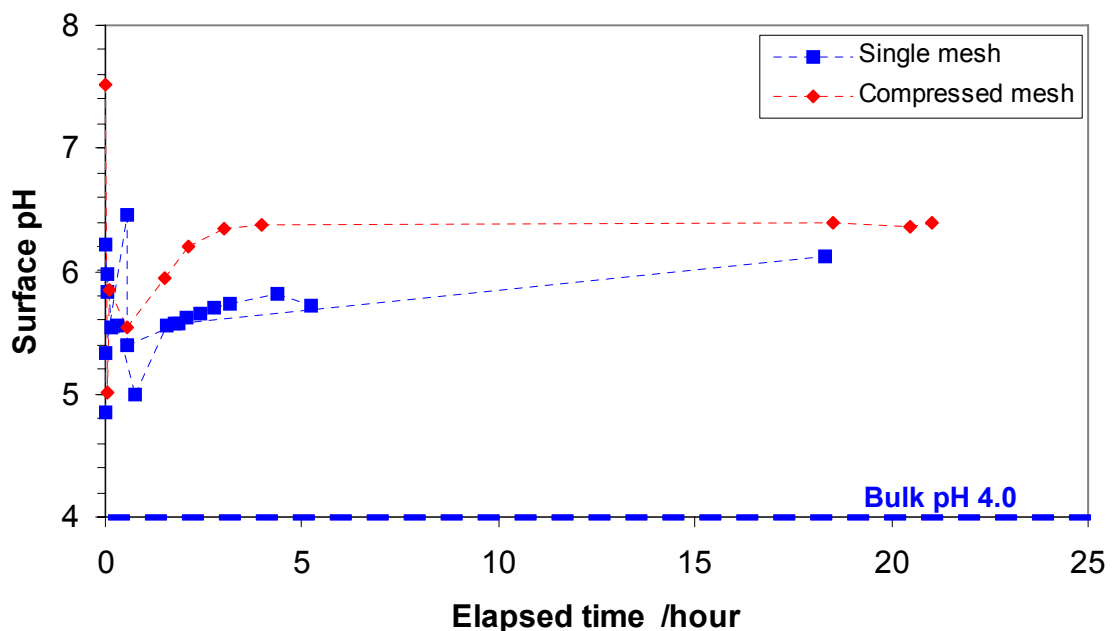


Figure 65. The surface pH measurement comparison between a single sheet mild steel mesh and a double sheet compressed mild steel mesh at bulk pH 6.0, $T=25^{\circ}\text{C}$, $p_{\text{total}}=1\text{bar}$, $p_{\text{CO}_2}=0.97\text{bar}$, $[\text{NaCl}]=1\text{wt}\%$.

The surface pH was measured using a single mesh and a compressed double mesh with a smaller pore size, as depicted in Figure 60 (a) and (b), respectively. The surface pH, as shown in Figure 65, is initially higher on the compressed mesh compared to that on the single mesh. It is thought that this is due to the fact that ions diffuse less readily from surface to bulk through the tighter mesh barrier making it slower for the pH probe to

reach a steady state. After an extended period of time, both probes reach approximately the same value.

5.3.2 Chemical buffer effect on surface pH

Since the pH is affected by the buffer capacity of the electrolyte, three cases are compared in Figure 66, all at bulk pH 4.0.

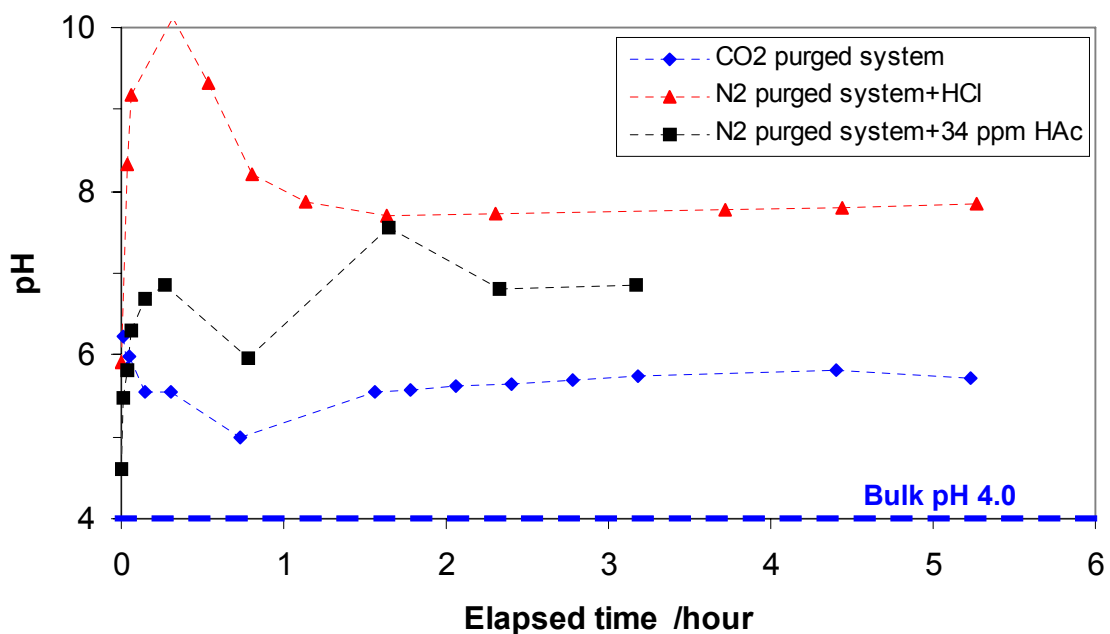


Figure 66. Surface pH during mild steel mesh corrosion in an aqueous solution purged with CO₂ or N₂ at bulk pH 4.0, T=25°C, p_{total}= 1bar, P_{CO₂/N₂}=0.97 bar, [NaCl] = 1wt%.

In a N₂ purged HCl solution the surface pH stabilizes at 7.8, *i.e.*, almost 4 pH units higher than the bulk pH. The surface pH increases only to 5.8 if the pH 4 solution is buffered by CO₂ where carbonic acid provides an extra source of H⁺ (see reaction 5-6) and contributes to a lower surface pH than observed for a N₂ saturated HCl electrolyte.

For an N₂ purged HAc system, the surface pH stabilizes at about 7. The degree of deviation of surface pH from the bulk value increases with decreasing buffer capacity. The highest observed surface pH values occur in systems with the least bulk solution buffering capacity.

5.3.3 Temperature effect on surface pH

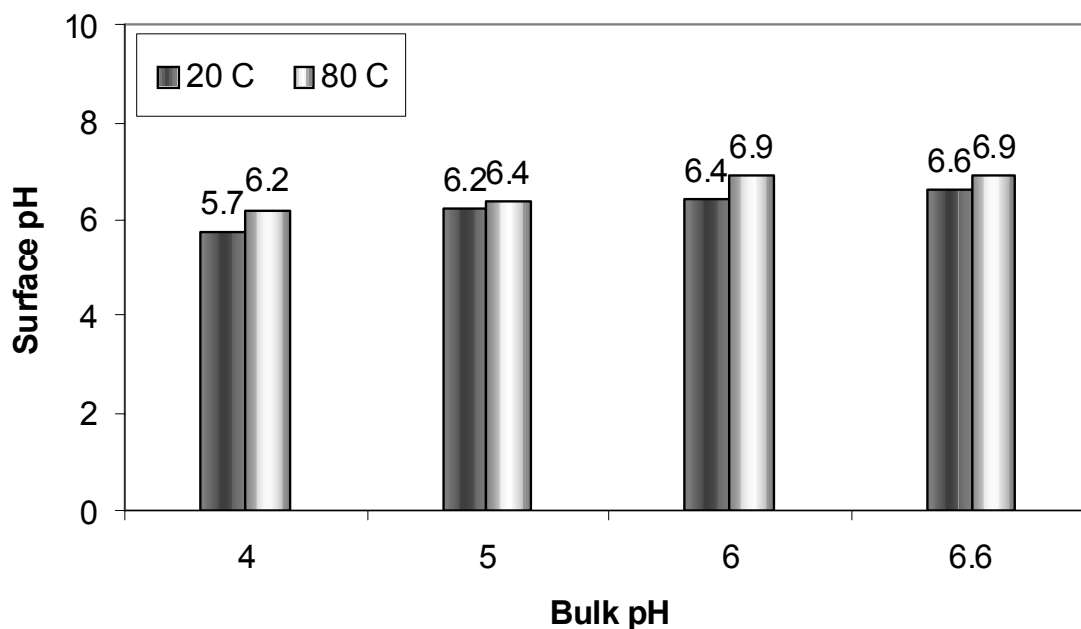


Figure 67. Surface pH comparison during a mild steel mesh corrosion, between 25°C and 80°C in a solution saturated with CO₂ under bulk pH 4.0, $p_{\text{total}}=1\text{bar}$, $p_{\text{CO}_2}=0.97\text{bar}$ (at 25°C), $p_{\text{CO}_2}=0.53\text{bar}$ (at 80°C), [NaCl] = 1wt%.

Higher surface pH was observed at higher temperature in all the series of measurements. A comparison of surface pH at 25 °C and 80 °C is given in Figure 67 (for a bare corroding mild steel mesh) and Figure 68 (under a glass bead deposit layer). The surface conditions can be alkaline at 80°C while they remain acidic at 25 °C. This is due

to the fact that corrosion rate is higher at higher temperature and more protons are consumed. This results in a higher surface pH. Besides, CO_2 dissolves less in the solution at higher temperatures and constitutes a weaker buffer solution. Both mechanisms contribute to a higher surface pH at higher temperature.

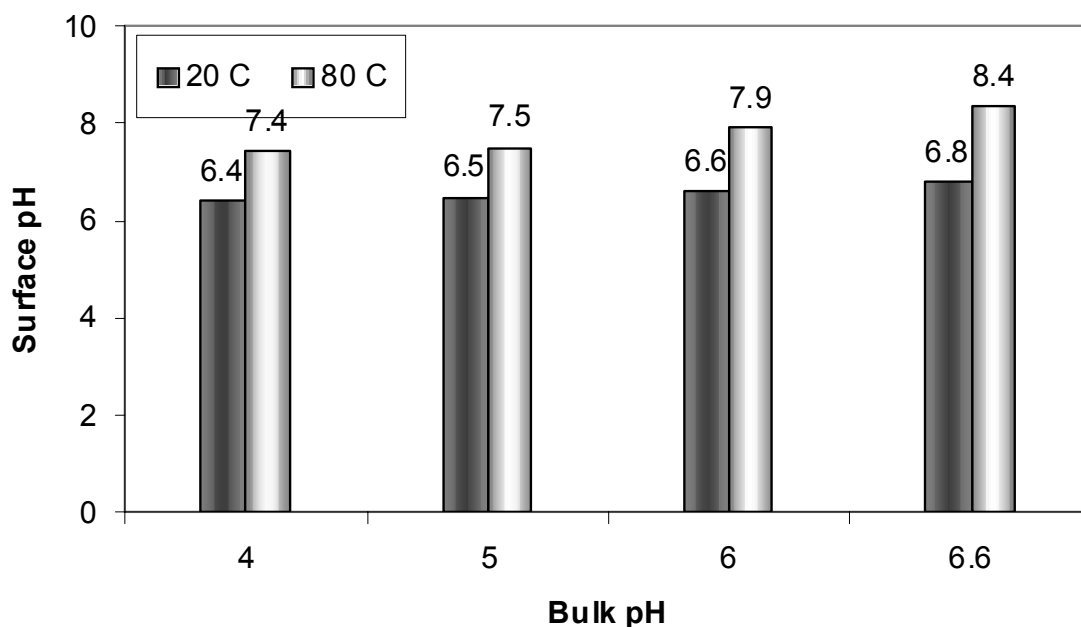


Figure 68. Surface pH measurement during mild steel mesh corrosion under a glass bead deposit layer 5mm in depth at different temperatures under bulk pH 4.0, 5.0, 6.0 and 6.6, $p_{\text{CO}_2}=0.97$ bar (at 25 °C) or $p_{\text{CO}_2}=0.53$ bar (at 80 °C) $[\text{NaCl}]=1\text{wt}\%$.

5.3.4 Effect of deposit layer porosity on surface pH

When a 5 mm thick glass bead deposit layer (particle size 50-80 μm) was introduced on the mild steel mesh, the surface pH increased above pH 6, even over pH 8 in some cases as demonstrated in Figure 69 and Figure 70, at both low and high temperature.

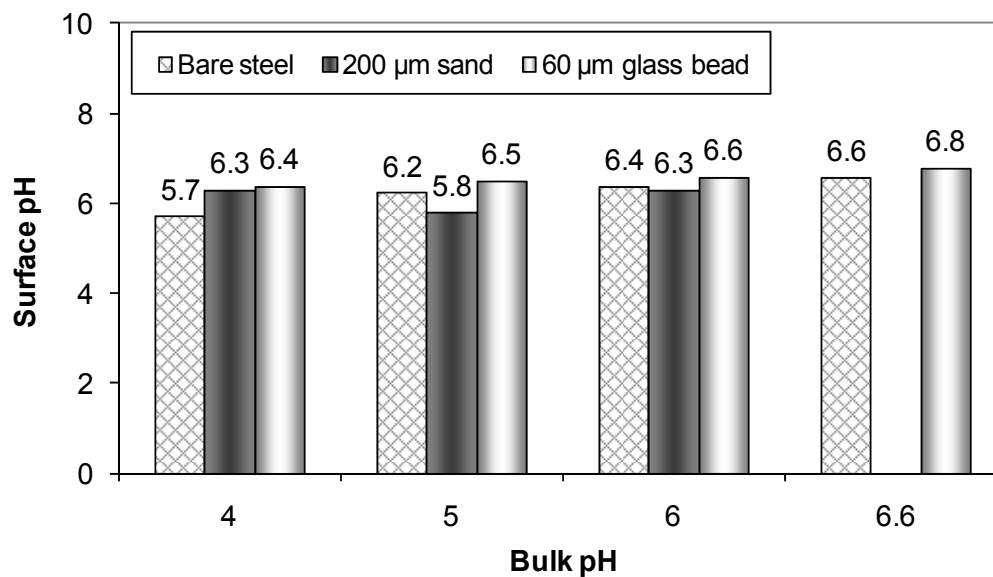


Figure 69. Surface pH measurement for a bare mild steel mesh and one under 5mm depth deposit, corroding at bulk pH 4.0, 5.0, 6.0, 6.6, $T=25^{\circ}\text{C}$, $p_{\text{CO}_2}=1$ bar, $[\text{NaCl}]=1\text{wt}\%$.

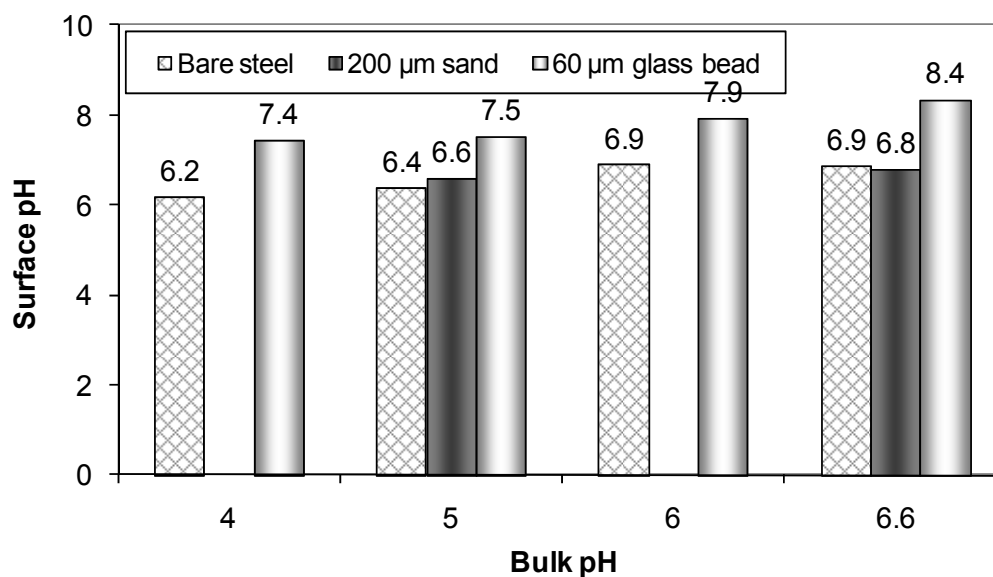


Figure 70. Surface pH measurement for a bare mild steel mesh and one under 5mm depth deposit, corroding at bulk pH 4.0, 5.0, 6.0, 6.6, $T=80^{\circ}\text{C}$, $p_{\text{CO}_2}=0.53$ bar, $[\text{NaCl}]=1\text{wt}\%$.

5.3.5 Surface pH measurement at different bulk pH values

Surface pH measurement data were compiled in Table 14 for various bulk pH values and at different temperatures, all obtained in a CO₂ purged solution. For all the cases, higher surface pH was observed compared with bulk solution pH for a corroding mild steel mesh. Similarly, higher surface pH observations were made under deposit layers. Greater surface pH deviation was observed at lower bulk pH conditions. Finer glass bead deposits with a lower porosity made the surface pH deviation from the bulk larger, even in some cases reaching mildly alkaline surface conditions in an acidic bulk solution. This indicates that, take an example of corrosion in CO₂ environments, more alkaline local water chemistry can be achieved under the corrosion product layer. The consequence is that a stable passive phase, Fe₃O₄, forms, exactly as observed and reported in literature. [62]

Table 14. Surface pH measurement during mild steel mesh corroding in a CO₂ saturated solution, with and without deposit layers

T /°C	P _{CO2} /bar	Bulk pH of solution	Surface pH under deposit		
			bare steel	sand	glass bead
25	0.97	4	5.7	6.3	6.4
		5	6.2	5.8	6.5
		6	6.4	6.3	6.6
		6.6	6.6	NA	6.8
80	0.53	4	6.2	NA	7.44
		5	6.4	6.6	7.53
		6	6.9	NA	7.92
		6.6	6.9	6.8	8.35

Chapter 6: Modeling localized CO₂ corrosion on mild steel⁶

6.1 Introduction

There are virtually no comprehensive mechanistic models of localized CO₂ corrosion. Probably the most notable is the one proposed in Achour^[37] work. It is a mechanistic model based on galvanic effects, hypothesizing that a galvanic cell could be established between the anodic pit surface and the film covered cathode. The open circuit potential difference between the anode and cathode of the cell was not experimentally quantified in that work. The mathematical treatment of this galvanic effect had the open circuit potential of the cathode artificially set 100mV higher than that of the anode. Clearly some of the general ideas developed in this work were adopted and further developed in the present effort.

To summarize, in the present study, it was revealed that under scaling conditions, an iron carbonate film can be developed. Local conditions underneath the iron carbonate film facilitate formation of a passive film containing Fe₃O₄. This leads to a higher open circuit potential on the passivated surface than on the bare steel surface. When the integrity of the films is locally corrupted, a galvanic cell can be established between the passivated surface and bare surface. This results in accelerated corrosion on the bared surface (anode) and retarded corrosion on the passivated surface (cathode). The present electrochemical mechanistic model was developed to describe this physicochemical process. The key novelty in the current model is that it can predict the spontaneous passivation of the cathode as well as the galvanic potential difference and galvanic current in the established galvanic cell between the bare pit surface (anode) and the

⁶ This chapter has been published as an ICC 17th conference paper (paper No. 2687).

passivated surrounding surface (cathode). Thus the polarized potential of the anode can be calculated explicitly.

6.2 Localized CO₂ corrosion mechanism

Combination of the information presented above permits the development of a localized corrosion mechanism, as shown in Figure 71. The mechanism can be summarized as follows. In the initial stage, the steel is exposed to a corrosive environment. A ferrous carbonate scale can form when its solubility limit is exceeded (Figure 71-1). The local pH increases beneath the ferrous carbonate scale. Consequently, a passive film (Fe₃O₄) is formed resulting in passivation, as evidenced by an increase in the potential (Figure 71-2). Localized corrosion may be initiated when the ferrous carbonate scale is locally damaged due to mechanical or chemical effects. The passive film is then exposed to the bulk environment where the pH is lower compared with that under the scale. As a result, the passive film dissolves and the steel becomes locally depassivated (Figure 71-3) leading to further passive film removal at the surrounding area (Figure 71-4). The potential of the large surrounding surface covered by passive film and protective ferrous carbonate scale is higher than that of the bare metal surface, which leads to establishment of a galvanic cell. This results in the bare steel corroding at a very high rate due to the galvanic effect (Figure 71-5). Detachment of the iron carbonate scale causes the pit to grow wider (Figure 71-6).

chemistry model describes the major chemical reactions in CO₂ aqueous environments, including CO₂ gas dissolution, CO₂ hydration, carbonic acid dissociation and water dissociation. The following text describes the model in more detail.

6.3.1 Water chemistry model

The CO₂ in the gas phase dissolves in the aqueous solution and then hydrates to produce carbonic acid. The latter only partially dissociates in the solution to produce protons and bicarbonate ions. Bicarbonate ions further dissociate and generate carbonate ions and protons [18–25] and the equations to describe them are presented in Chapter 2 but are repeated here for convenience:

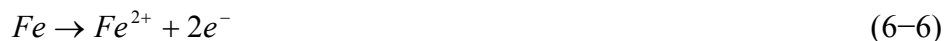


6.3.2 Electrochemistry model

The electrochemistry model is composed of three modules to describe: the active steel dissolution reactions at the anode, the spontaneous passivation reaction on the cathode and the galvanic cell establishment between the anode and the cathode.

6.3.2.1 Modeling reactions on the anode

The key oxidation reaction on the anode is iron dissolution:



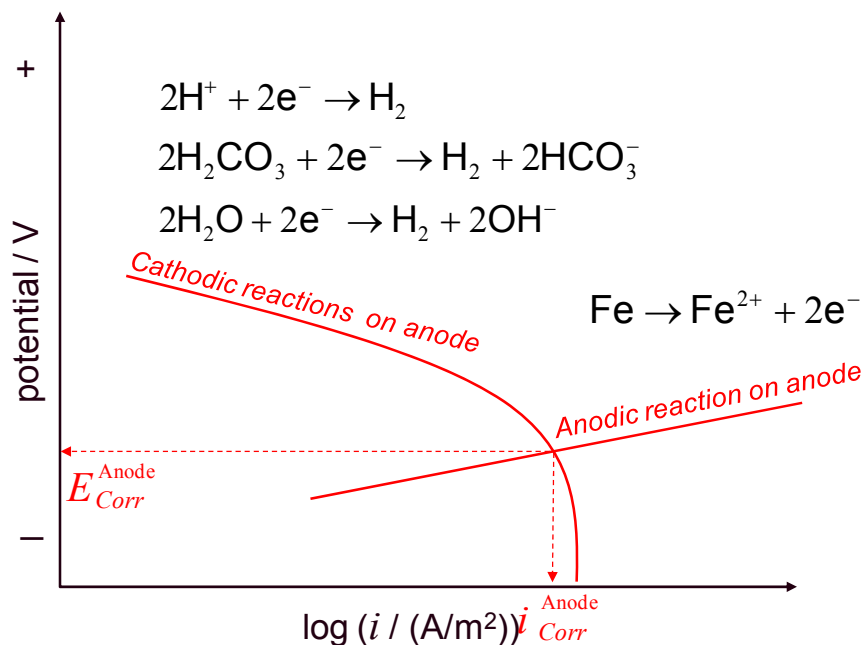


Figure 72. Schematic representation of active corrosion on the bare anode surface (pit bottom).

The main reduction reactions occurring on the anode are carbonic acid reduction, proton reduction and water reduction.



Both the oxidation and reduction reactions happening on the anode are schematically shown in Figure 72. In this mathematical model, the electrochemical parameters and physical properties used to describe these electrochemical reactions were previously given by S. Nestic^[18-25] and are described below.

The corrosion rate is linearly related to the corrosion current density as defined:

$$CR = \text{const.} \cdot i_{\text{corr}} \quad (6-10)$$

where, CR is corrosion rate in mm/year, const. is a material depend constant, 1.155 for steel. i_{corr} is corrosion current density in A/m².

The corrosion reaction kinetics can be controlled by charge transfer and/or by mass transfer processes:

$$\frac{1}{i_{\text{corr}}} = \frac{1}{i_r} + \frac{1}{i_L} \quad (6-11)$$

where, i_r is the charge transfer (activation) controlled reaction current density (rate) and i_L is the mass transfer limited current density (rate). The i_L can be determined by the flow conditions and will be discussed in the following sections.

The Butler- Volmer equation can be used to calculate i_r expressed as:

$$i_{r,a} = i_0 \left\{ e^{\left[\frac{(1-\alpha) \cdot n \cdot F}{R \cdot T} \cdot (E - E_{\text{eq}}) \right]} - e^{\left[\frac{(-\alpha) \cdot n \cdot F}{R \cdot T} \cdot (E - E_{\text{rev}}) \right]} \right\} \quad E > E_{\text{rev}} \text{ or } \eta > 0 \quad (6-12)$$

and:

$$i_{r,c} = i_0 \left\{ e^{\left[\frac{(-\alpha) \cdot n \cdot F}{R \cdot T} \cdot (E - E_{\text{rev}}) \right]} - e^{\left[\frac{(1-\alpha) \cdot n \cdot F}{R \cdot T} \cdot (E - E_{\text{eq}}) \right]} \right\} \quad E < E_{\text{rev}} \text{ or } \eta < 0 \quad (6-13)$$

For a system which involves many reacting species, the governing equation expressing charge balance at steady state can be expressed as:

$$\sum_i i_{i,c} = \sum_i i_{i,a} \quad (6-14)$$

Cathodic reactions:

a). Carbonic acid reduction

Carbonic acid reduction as shown by equation (6-11) can be calculated using the governing equation:

$$\frac{1}{i_{c,H_2CO_3}} = \frac{1}{i_{r,H_2CO_3}} + \frac{1}{i_{l,H_2CO_3}} \quad (6-15)$$

The charge transfer current density (electrochemical reaction control) and the chemical reaction limiting current density are defined as ^[18]:

$$i_{c,H_2CO_3} = i_{o,H_2CO_3} \cdot 10^{\frac{E_{corr} - E_{rev,H_2CO_3}}{b_c}} \quad (6-16)$$

$$i_{l,H_2CO_3} = Fc_{CO_2,aq} (D_{H_2CO_3} K_0^O k_0^f)^{0.5} f \quad (6-17)$$

where, i_{o,H_2CO_3} is the exchange current density depending on pH, H_2CO_3 concentration, and temperature:

$$\frac{\partial \log i_{o,H_2CO_3}}{\partial pH} = 0.5 \quad (6-18)$$

$$\frac{\partial \log i_{o,H_2CO_3}}{\partial c_{H_2CO_3}} = 1 \quad (6-19)$$

$$\frac{i_{o,H_2CO_3}}{i_{o,H_2CO_3}^{ref}} = e^{-\frac{\Delta H_{H_2CO_3}}{R} \left(\frac{1}{T} - \frac{1}{T_{ref}} \right)} \quad (6-20)$$

where $\Delta H_{H_2CO_3}$ is the enthalpy of activation (50 kJ/mol), T_{ref} is the reference temperature to be 25°C, and i_0^{ref} is the exchange current density for hydrogen ion reduction at the reference temperature (0.0846 ^[18]). b_c is the cathodic Tafel slope defined below:

$$b_c = 2.303 \frac{RT}{0.5F} \quad (6-21)$$

E_{rev,H_2CO_3} is the reversible potential for carbonic acid reduction as below¹⁸,

$$E_{rev,H_2CO_3} = -\frac{2.303RT}{F} pH \quad (6-22)$$

The $c_{CO_2, aq}$ is the concentration of carbon dioxide in the solution and calculated by water chemistry model. $D_{H_2CO_3}$ is the diffusion coefficient of carbonic acid and can be obtained from equation (6-36) knowing D_{ref,H_2CO_3} is 1.3E-9 at room temperature [9].

The μ_{ref} is $8.905 \cdot 10^{-4}$ Ps·S in equation (6-20) used to calculate the limiting current density. K_0^O is the equilibrium constant for the CO₂ hydration reaction can be assumed constant $2.58 \cdot 10^{-3}$. The k_0^f is the forward reaction rate for the CO₂ hydration reaction and can be expressed as [18]:

$$k_0^f = 10^{169.2 - 53.0 \log T - \frac{11,715}{T}} \quad (6-23)$$

$f_{H_2CO_3}$ is the flow factor, a function of the reaction diffusion layer¹¹⁷.

$$f_{H_2CO_3} = \frac{1 + e^{-2\zeta_{H_2CO_3}}}{1 - e^{-2\zeta_{H_2CO_3}}} = \coth \zeta_{H_2CO_3} \quad (6-24)$$

where

$$\zeta_{H_2CO_3} = \frac{\delta_{m,H_2CO_3}}{\delta_{r,H_2CO_3}} \quad (6-25)$$

and δ_{m,H_2CO_3} is the mass transfer (diffusion) layer thickness and δ_{r,H_2CO_3} is the chemical reaction layer thickness.

$$\delta_{m,H_2CO_3} = \frac{D_{H_2CO_3}}{k_{m,H_2CO_3}} \quad (6-26)$$

$$\delta_{r,H_2CO_3} = \sqrt{\frac{D_{H_2CO_3}}{k_0^b}} \quad (6-27)$$

The $D_{H_2CO_3}$ is the carbonic acid diffusion coefficient; k_{m,H_2CO_3} is the carbonic acid mass transfer coefficient and determined by fluid dynamics. k_0^b is the backward reaction rate of carbonic acid dehydration reaction and can be obtained by:

$$k_0^b = \frac{10^{\frac{169.2 - 53.0 \log T - \frac{11,715}{T}}{}}}{2.58 \times 10^{-3}} \quad (6-28)$$

b) H⁺ ion reduction

The H⁺ ion reduction calculation can start from the governing equation is shown in the following:

$$\frac{1}{i_{c,H^+}} = \frac{1}{i_{r,H^+}} + \frac{1}{i_{l,H^+}} \quad (6-29)$$

where, i_{r,H^+} is the charge transfer current density and i_{l,H^+} is the mass transfer limiting current density and can be calculated as follows.

The same formula as equations (6-12 to 6-14 and 6-31 to 6-38) is applied to calculate the charge transfer current density knowing the parameters of $\Delta H_{H_2CO_3}=30$ kJ/mol, $i_0^{ref}=0.05$ A/m² [18] at $T_{ref}=25$ °C.

The reversible potential for H⁺ reduction E_{rev,H^+} is a function of temperature, pH, and the partial pressure of hydrogen in bar, as shown below.

$$E_{rev,H^+} = E_{rev,H^+}^O - \frac{2.303RT}{F} pH - \frac{2.303RT}{2F} \log P_{H_2} \quad (6-30)$$

The limiting current density for proton reduction can be calculated as follows.

The i_L is the mass transfer limited corrosion current density and can be calculated by:

$$i_{lim(i)} = nk_{m,i}Fc_i \quad (6-31)$$

where, n is the number of charges (electrons) transferred during an electrochemical reaction, c_i is the concentration. $k_{m,i}$ is the mass transfer coefficient for species i and can be obtained by:

$$Sh = \frac{k_m d}{D} = const. \cdot Re^x Sc^y \quad (6-32)$$

where, Re is the Reynolds number, and Sc is the Schmidt number.

$$Re = \frac{dv\rho}{\mu} \quad (6-33)$$

$$Sc = \frac{\mu}{\rho D} \quad (6-34)$$

where, d is the hydraulic diameter, ρ is solution density, D is diffusion coefficient and can be determined by:

$$D = D_{ref} \left(\frac{T}{T_{ref}} \right) \left(\frac{\mu_{ref}}{\mu} \right) \quad (6-35)$$

where D_{ref} is the diffusion coefficient at the reference temperature T_{ref} . μ_{ref} is the viscosity at a reference temperature of 25°C and μ is the water viscosity in Pa·S depending on temperature and can be determined by:

$$\mu = 1.002 \times 10^{-3} \times 10^{\frac{1.3272 \times (293.15 - T) - 0.001053 \times (293.15 - T)^2}{T + 378.15}} \quad (6-36)$$

For a rotating cylinder, Eisenberg's^[115] correlation gives:

$$Sh = \frac{k_m d_p}{D} = 0.0165 Re^{0.86} Sc^{0.33} \quad (6-37)$$

where D_p is the diameter of the pipeline in m,

For a straight pipe, Berger and Hau's correlation can be applied^[116]:

$$Sh = \frac{k_m d_c}{D} = 0.0791 Re^{0.7} Sc^{0.356} \quad (6-38)$$

where d_c is the diameter of rotating cylinder.

c) Water reduction

The reduction rate of H_2O is controlled by the charge-transfer process under the assumption that water molecules are always present at the steel surface. The redox systems including H_2O , H_2CO_3 and H^+ have the same reversible potential considering the equivalent thermodynamics.

The exchange current density for water reduction $i_{o(H_2O)}$ depends on the temperature. There is no variation of the exchange current density from pH 3 to pH 6.

Knowing the parameters of $\Delta H_{H_2O} = 30 \text{ kJ/mol}$ ¹⁸, $i_0^{\text{ref}} = 3 \cdot 10^{-5} \text{ A/m}^2$ ¹⁸ at $T_{\text{ref}} = 25^\circ\text{C}$, the charge transfer current density can be calculated. The limiting current density is obtained from fluid dynamics and is not repeated.

Anodic reaction

Iron oxidation is the only anodic reaction in the current corrosion system. Its anodic reaction is considered to be under charge transfer control as expressed below:

$$i_{a,Fe} = i_{o,Fe} \cdot 10^{\frac{E_{\text{corr}} - E_{\text{rev},Fe}}{b_a}} \quad (6-39)$$

The reversible potential can be expressed as follows:

$$E_{\text{rev},Fe} = -0.44 + \frac{2.303RT}{2F} \log c_{Fe^{2+}} \quad (6-40)$$

Here it is assumed that ferrous ion reduction or the so called “iron deposition” is negligible comparing to carbonic acid, proton and water reduction. The current model

only accounts for the iron oxidation. Thus, a reference potential $E_{\text{ref,Fe}}$, a reference current density $i_{\text{ref,Fe}}$ and the Tafel slope b_a will be enough to represent the anodic corrosion reaction.

The reference potential for anodic dissolution of iron $E_{\text{ref,Fe}}$ was reported to be -0.488 V¹⁸. The exchange current density is:

$$i_{o,Fe} = i_{o,Fe}^{\text{ref}} \times e^{-\frac{\Delta H_{Fe}}{R} \left(\frac{1}{T} - \frac{1}{T_{\text{ref}}} \right)} \quad (6-41)$$

where $i_{o,Fe}^{\text{ref}}$ is 1 A/m² [18], the activation enthalpy for anodic reaction $\Delta H_{\text{H}_2\text{O}}$ is 37.5 kJ/mol from 20°C to 50°C [18].

The anodic Tafel slope for iron dissolution is:

$$b_a = 2.303 \frac{R(T_c + 273.15)}{1.5F} \quad (6-42)$$

6.3.2.1 Modeling spontaneous reactions on the cathode

A passive film, which is likely to be a form of oxide such as Fe_3O_4 , can form beneath a protective iron carbonate film leading to passivation of the cathode. Therefore under these conditions the oxidation reaction on the passivated cathode surface is the passive dissolution of iron. The overall anodic reaction for the passive anodic dissolution of iron can be written as:



The rate of this reaction corresponds to the “vertical” region of the anodic polarization curve in Figure 73). The passivation current density, a kinetic parameter, describing the passive iron dissolution reaction rate on the cathode (Figure 73), has to be

experimentally determined; little information on spontaneous passivation of mild steel has been reported in the literature.

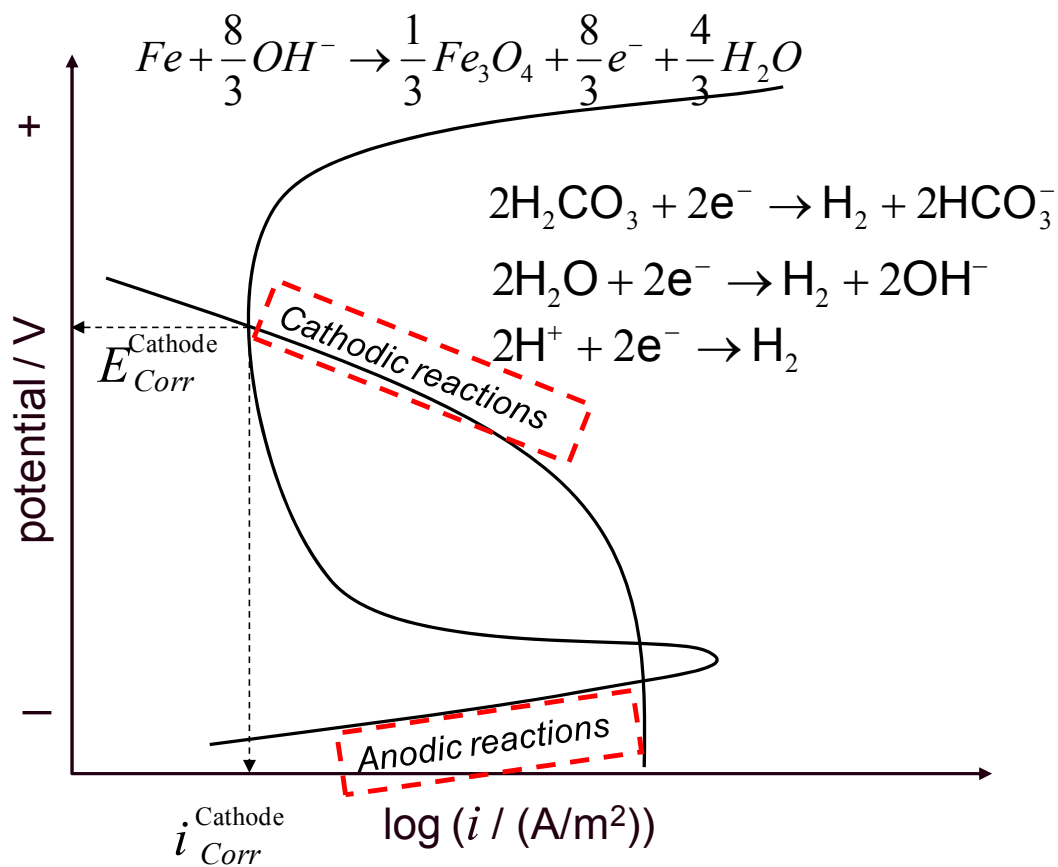


Figure 73. Schematic representation of passive corrosion on the cathode (iron carbonate covered steel surface around the pit).

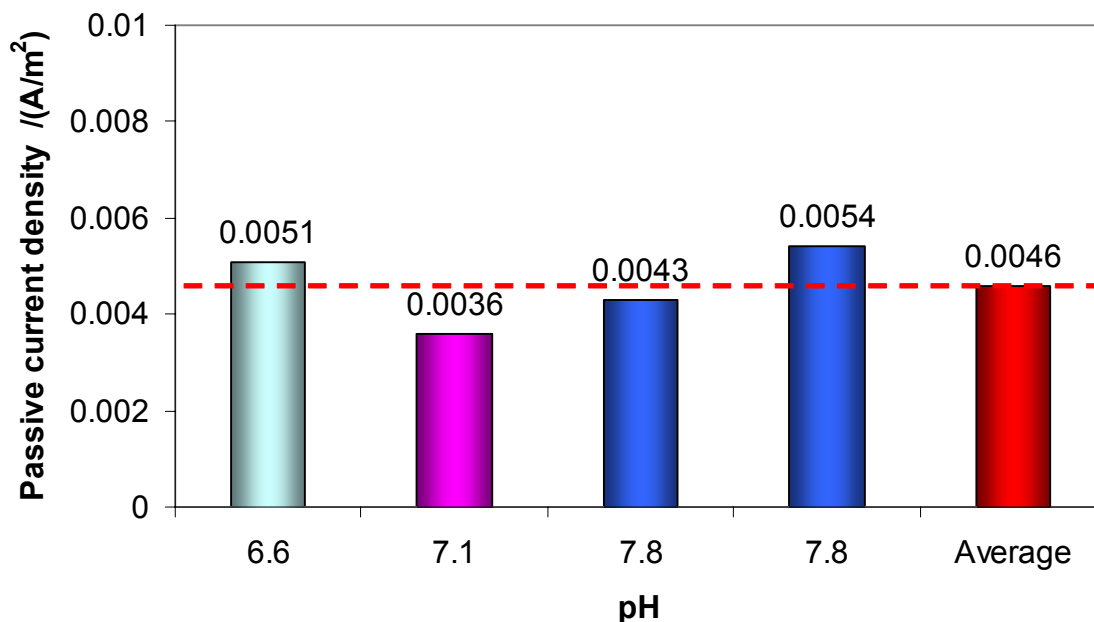


Figure 74. Spontaneous passivation current density as a function of pH at $T=80^{\circ}\text{C}$, $P_{\text{CO}_2}=0.53$ bar, $P_{\text{total}}=0.53$ bar, $\text{NaCl}=1$ wt. %.

The passivation current density for the anodic reaction appears to be independent of pH as shown in Figure 74. These data were obtained from the present work and the corrosion rate measurements after the achieving spontaneous passivation on the steel surface exposed to CO_2 aqueous environments.

The reduction reactions that occurs on the cathode includes carbonic acid, proton and water reduction. It is assumed that the nature of these reduction reactions occurring on the cathode is the same as those occurring on the anode surface. However, the kinetics on the passivated cathode appears to be slower compared with those occurring on a bare anode due to the presence of an iron carbonate film. A retardation factor f was introduced to estimate the film protective properties and the effect on the reduction

reactions because the present model cannot explicitly predict the film properties such as film porosity, film thickness and pore tortuosity, etc. This factor is used as in equation (6-44) and can be related to the pH as depicted in Figure 75.

$$i_{c, passive}^o = \frac{i_{c, bare}^o}{f} \quad (6-44)$$

where, $i_{c, passive}^o$ and $i_{c, bare}^o$ are the exchange current densities for reduction reaction on the passive and bare steel surfaces respectively.

Knowing the kinetics of the oxidation and reduction reaction processes on the cathode, the open circuit potential, corrosion rate and polarization curves for spontaneous passivation on the cathode can be calculated.

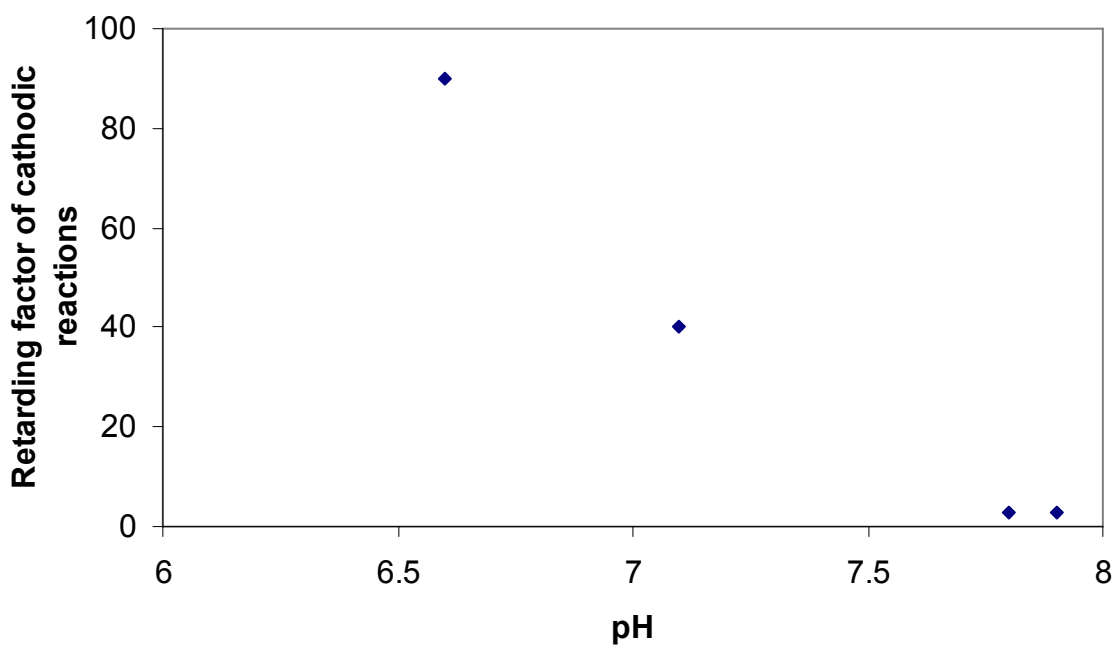


Figure 75. Factor f at $T=80^{\circ}\text{C}$, $P_{\text{CO}_2}=0.53$ bar, $P_{\text{total}}=1$ bar, $\text{NaCl}=1$ wt. %.

6.3.2.1 Modeling the galvanic cell established between anode and cathode

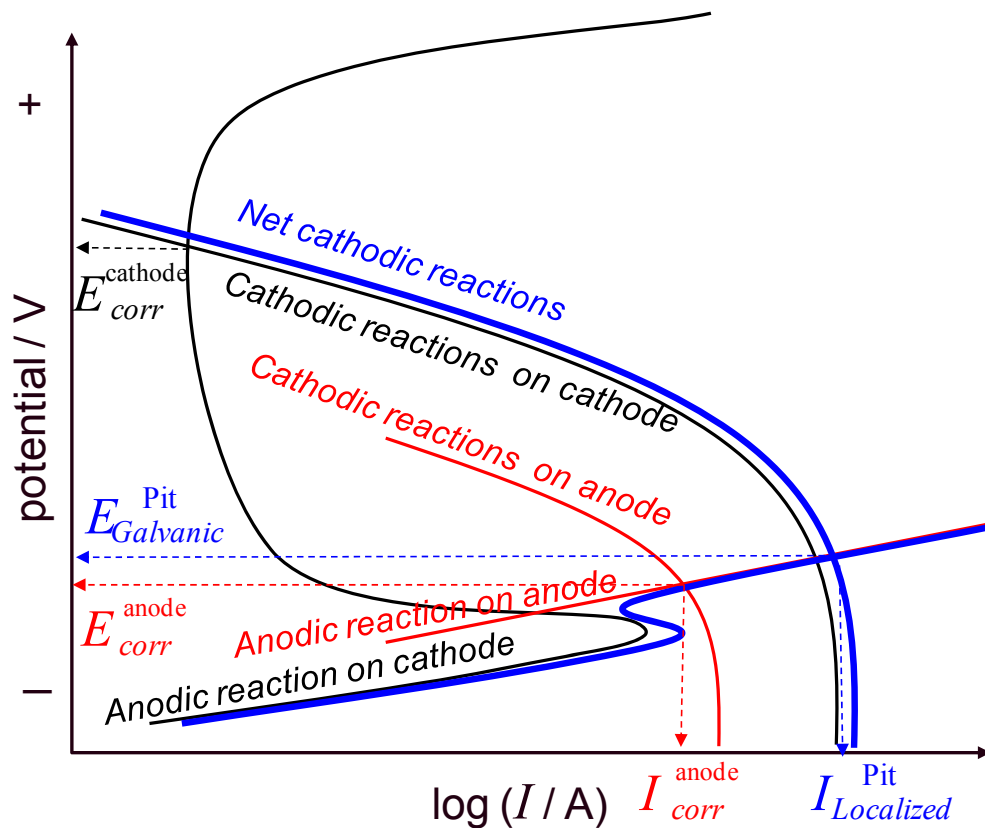


Figure 76. Scheme for galvanic cell established between bare anode and passive cathode.

The galvanic cell between anode and cathode can now be modeled since the rates of the reactions on these surfaces are quantifiable. The overall charge balance is established: oxidation currents from all the reactions on both surfaces (anode and cathode) are balanced by the overall reduction currents from the reactions, as shown in Figure 76. The mixed potential obtained is the galvanic or coupled potential. The

current flowing between the anode and cathode at the coupled potential is the galvanic current. The localized corrosion current (rate) can be calculated if the area ratio of the passivated cathode and the actively corroding pit is known. As shown schematically in Figure 76, the corrosion rate at the anode is accelerated after the galvanic cell is established.

6.4 Experimental validation of the model

The model was validated with the potentiodynamic polarization sweeps performed on a bare steel surface, passive surface and *via* artificial pit tests.

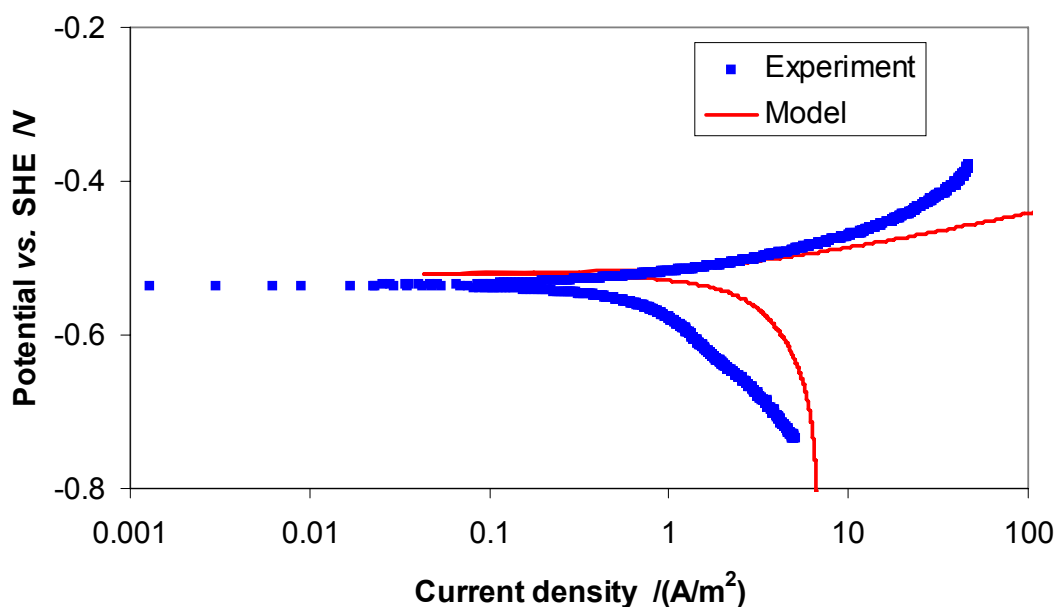


Figure 77. Model prediction matches an example of experimental polarization curves on a bare steel surface at $T=80\text{ }^{\circ}\text{C}$, $\text{pH } 7.0$, $P_{\text{CO}_2}=0.53\text{ bar}$, $P_{\text{total}}=1\text{ bar}$, $\text{NaCl}=1\text{ wt. \%}$.

An example of a potentiodynamic polarization sweep on a bare steel surface is shown in Figure 77. Comparison of the experimental data and model prediction shows a

reasonable agreement for the purposes of the present model. The deviation in the higher potential zone becomes severe as expected. The surface tends to be passive at this high pH condition in experiments.

Figure 78 shows a typical spontaneous passivation process. At the beginning of the test, the coupon was immersed in the solution. The open circuit potential was monitored and after a while a large change in the positive direction was observed without any external applied current or potential. This is an indication of spontaneous steel surface passivation.

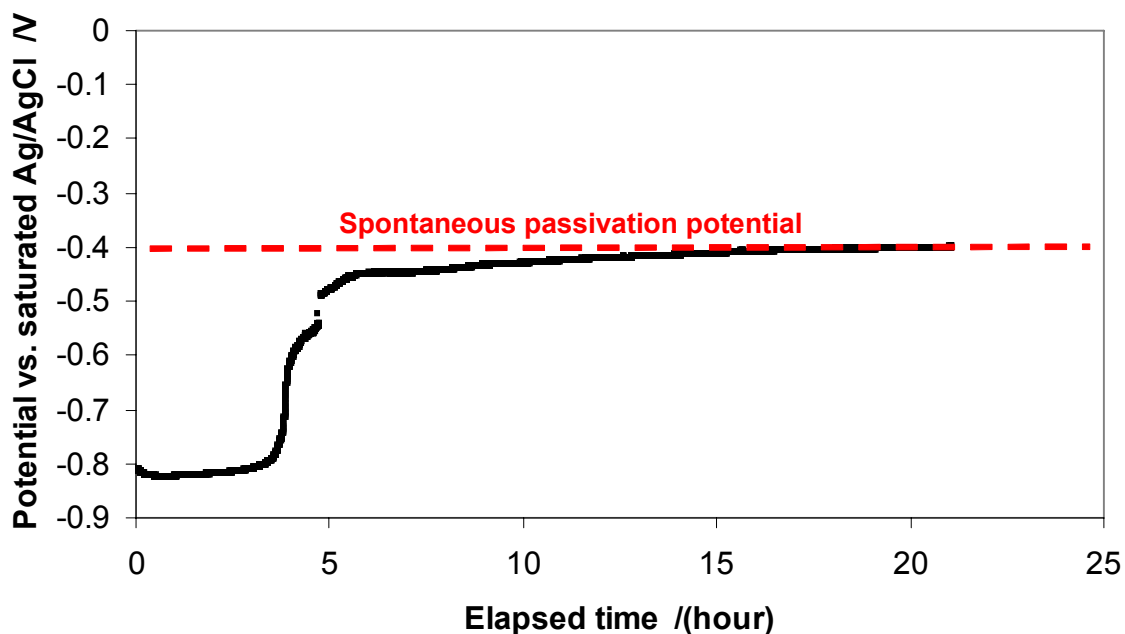


Figure 78. Open circuit potential change for the case of spontaneous passivation at $T=80$ °C, pH 7.8, NaCl=1 wt. %, $P_{CO_2}=0.53$ bar, $P_{total}=1$ bar, $Fe^{2+}_{initial}=0$ ppm.

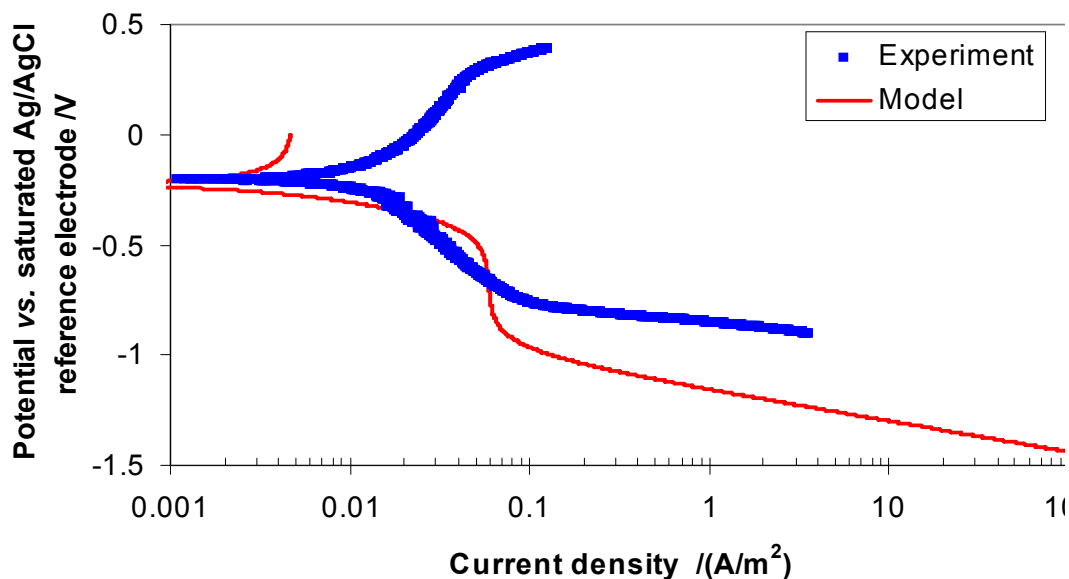


Figure 79. Comparison of model prediction and an experimental polarization curve on a passive steel surface at $T=80\text{ }^{\circ}\text{C}$, $\text{pH } 7.8$, $P_{\text{CO}_2}=0.53\text{ bar}$, $P_{\text{total}}=1\text{ bar}$, $\text{NaCl}=1\text{ wt. } \%$.

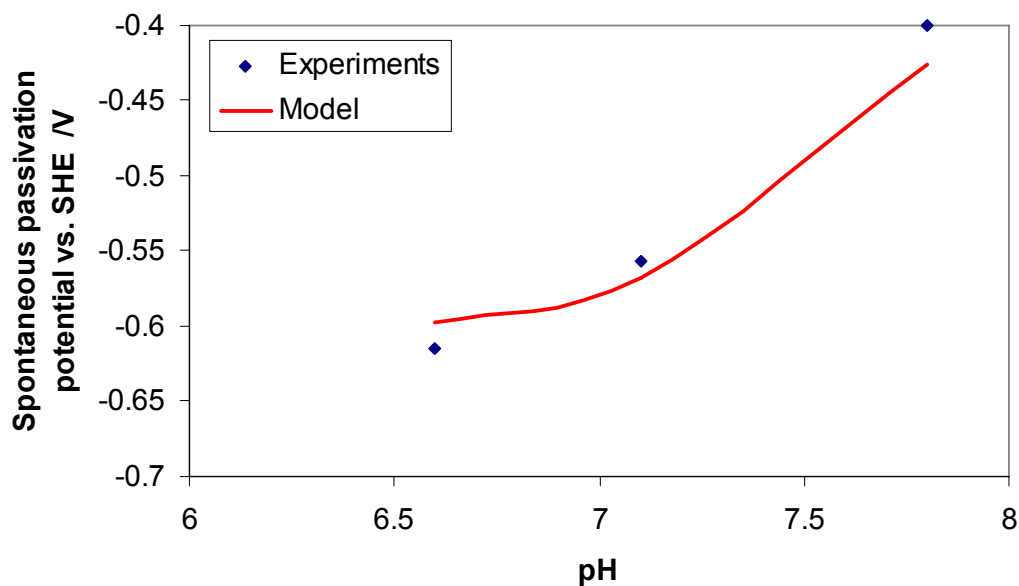


Figure 80. Comparison of a spontaneous passivation potential between the model and experimental data at $T=80\text{ }^{\circ}\text{C}$, $\text{NaCl}=1\text{ wt. } \%$, $P_{\text{CO}_2}=0.53\text{ bar}$, $P_{\text{total}}=1\text{ bar}$, $\text{Fe}^{2+}_{\text{initial}}=0\text{ ppm}$.

After the surface was fully passivated, a potentiodynamic polarization sweep was conducted. Experimental results and the model prediction are compared in Figure 79, where a good agreement is observed. The predicted pH dependence of the spontaneous passivation potential is in good agreement with the experimental data, as shown in Figure 80.

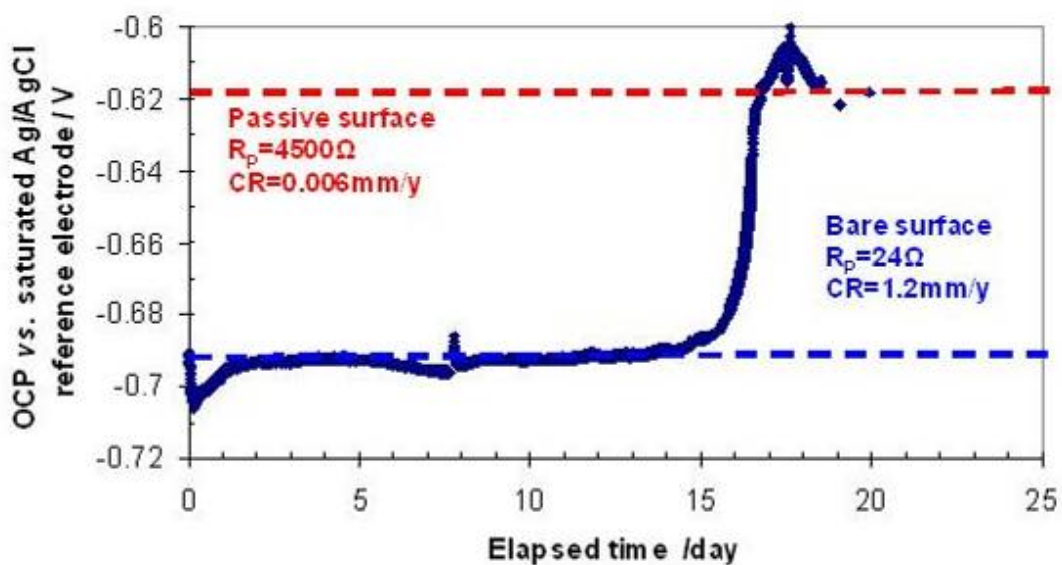


Figure 81. Open circuit potential (OCP) profile for spontaneous passivation on the cathode at $T=80\text{ }^{\circ}\text{C}$, $\text{pH } 6.6$, $\text{NaCl}=1\text{ wt } \%$, $P_{\text{CO}_2}=0.53\text{ bar}$, $P_{\text{total}}=1\text{ bar}$, $\text{Fe}^{2+}_{\text{initial}}=0\text{ ppm}$.

The galvanic cell model was validated by artificial pit tests. The set-up and procedure for the artificial pit has been previously discussed. The key idea behind the artificial pit test is that the cathode is initially spontaneously passivated, an example is shown in Figure 81. Subsequently a fresh small steel anode is then introduced and serves as an anode. Its open circuit potential is lower than that of the passivated cathode

surface. The two surfaces are then connected by a zero resistance ammeter (ZRA) and the resulting current measured.

The data obtained are shown in Figure 82 for a cathode to anode area ratio of 350. The coupled potential lies between the open circuit potential of the active anode and passive cathode.

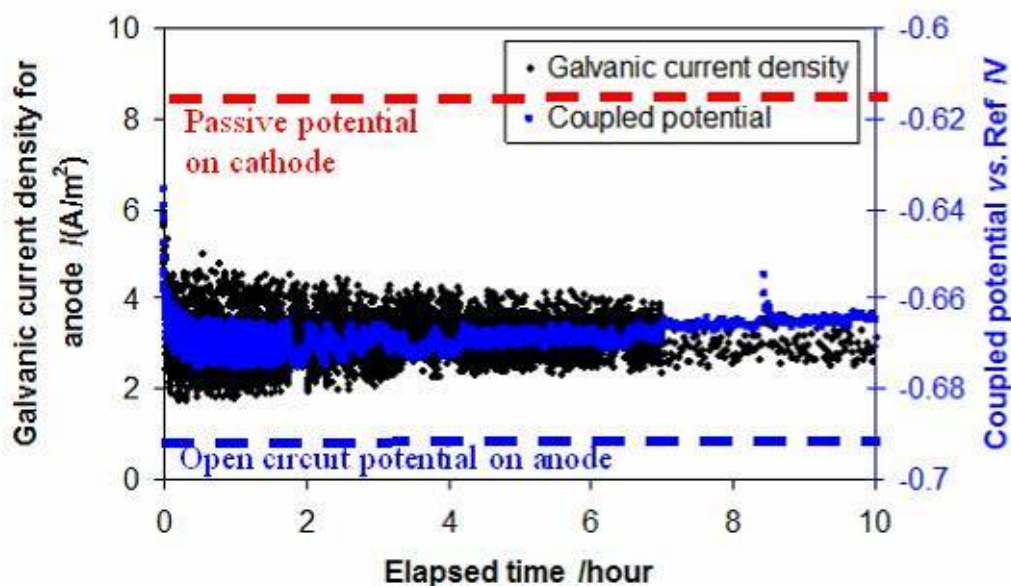


Figure 82. Galvanic current density with respect to anode and coupled potential profiles after the anode and cathode were connected during artificial pit test at $T=80\text{ }^{\circ}\text{C}$, $\text{pH } 6.6$, $\text{NaCl}=1\text{ wt. \%}$, $P_{\text{CO}_2}=0.53\text{ bar}$, $P_{\text{total}}=1\text{ bar}$, $\text{Fe}^{2+}_{\text{initial}}=0\text{ ppm}$, area ratio=350.

Figure 83 focuses on the galvanic current density with respect to the anode. The experimental data shows that the galvanic current density varies within a range of 2–4 A/m^2 . The prediction from the model is $7.6\text{ A}/\text{m}^2$, more than twice that experimentally observed. This is considered acceptable for this early stage of the model development. A ratio of the localized corrosion rate to the uniform corrosion rate of the anode represents a

measure of the severity of localized corrosion propagation. Comparison between the experimental results and model prediction for the ratio are in good agreement, as shown in Figure 84. A more detailed overview of the predictions is listed in Table 15 for this case.

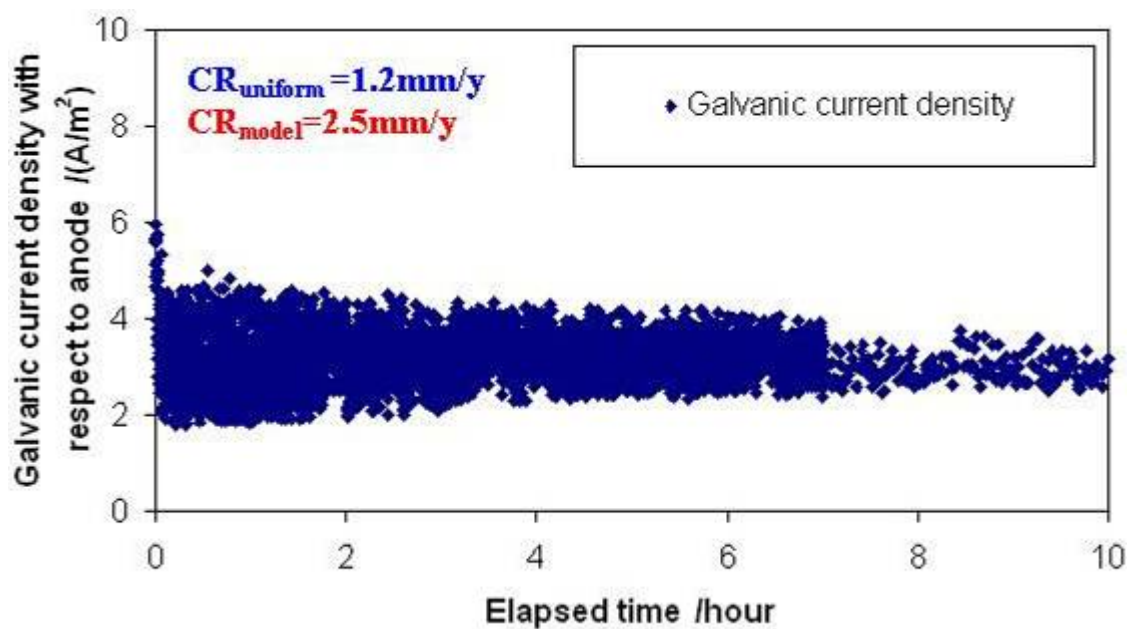


Figure 83. Galvanic current density with respect to the anode comparison between model prediction and experimental data at $T=80$ °C, pH 6.6, NaCl=1 wt. %, $P_{CO_2}=0.53$ bar, $P_{total}=1$ bar, $Fe^{2+}_{initial}=0$ ppm, area ratio=350.

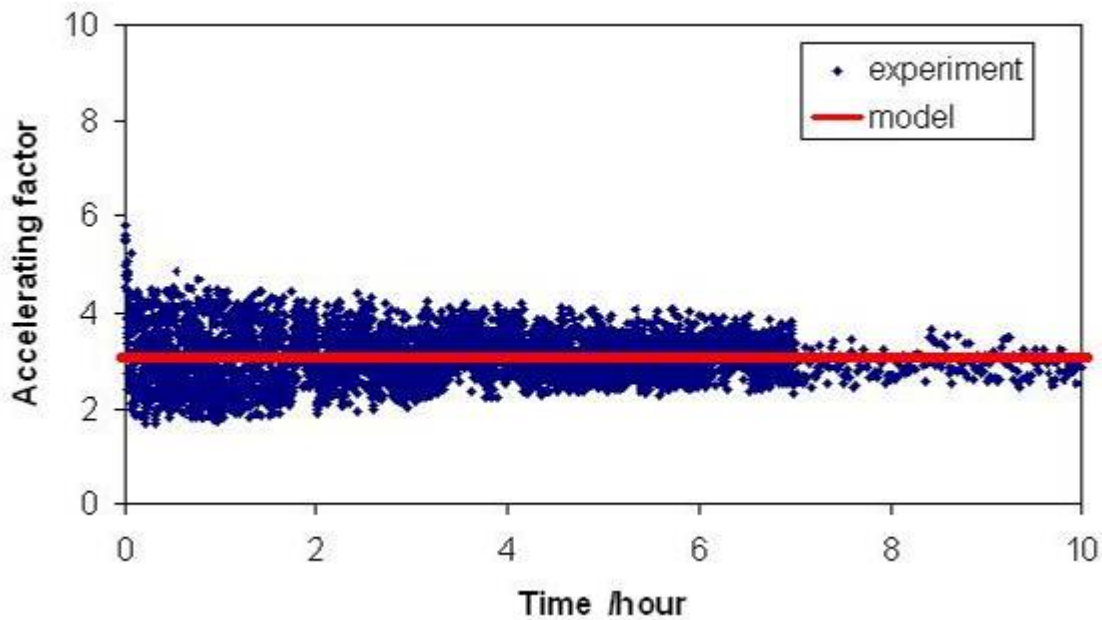


Figure 84. Localized corrosion acceleration factor comparison between model and experimental data at $T=80\text{ }^{\circ}\text{C}$, $\text{pH } 6.6$, $\text{NaCl}=1\text{ wt. \%}$, $P_{\text{CO}_2}=0.53\text{ bar}$, $P_{\text{total}}=1\text{ bar}$, $\text{Fe}^{2+}_{\text{initial}}=0\text{ ppm}$, $\text{area ratio}=350$.

Table 15. Comparison compilation of the experimental data and model predictions

		experiment	model
OCP cathode	/ V	-0.60 to -0.62	-0.60
OCP anode	/ V	-0.69 to -0.70	-0.72
Mixed potential	/ V	-0.68 to -0.67	-0.69
Increased potential of anode	/ mV	20–30	23
CRlocalized	/(mm/y)	2.2–4.4	7.6
CRuniform	/(mm/y)	1.2	2.5
Accelerating factor: (CRlocalized/CRuniform)		1.8–3.7	3.0

Chapter 7: Conclusions and future work suggestions

7.1 Conclusions

Localized CO₂ corrosion mechanisms were investigated by artificial pit cell, potential dynamic polarization, cyclic polarization, spontaneous passivation, depassivation tests and surface analysis using SEM, EDX, XRD, GIXRD and TEM/EDX. Summarizing all the above acquired knowledge permits the development of a galvanic mechanism for localized corrosion as follows.

- In the initial step, the ferrous carbonate scale is formed when its solubility limit is reached.
- This can cause a higher pH beneath a compact ferrous carbonate scale compared with that of the bulk.
- Consequently a magnetite (Fe₃O₄) passive film is locally formed, resulting in the potential increase.
- If the iron carbonate scale is locally damaged, the passive film dissolves and the steel is locally depassivated, leading to the exposure of its bare surface to bulk solution.
- The potential on the passivated surface is higher than that of the bare metal surface. The corrosion on bare steel surface is accelerated due to a galvanic coupling with the surrounding iron carbonate covered surface.

7.2 Future research suggestions

Localized CO₂ corrosion is a complex process. The research reported above uncovers just a tip of an iceberg. More extensive studies will be invaluable. Some ideas developed here can be referred to for future studies.

Pit geometry effects were studied under pure CO₂ environments. Although the effect could be observed, an improved controlled geometry design will be preferred. Only very simple single phase flow was considered in this research. A more realistic well controlled flow needs to be introduced into the study. Temperature effect were not investigated in this study, only 80°C was used. Extension of pH range, especially toward lower pH, needs to be looked at. Other environmental factors including H₂S effect, organic acid effect and oxygen effect on galvanic mechanism could be systematically investigated.

Extended research on scale property relation to localized corrosion initiation and propagation definitely benefit deeper understanding of localized corrosion mechanisms. The growth mechanism and kinetics for passive film can be improved using advanced surface analysis. A detailed study on passivation, environmental factors and water chemistry will improve the understanding of localized corrosion mechanisms.

A preliminary localized corrosion model was developed. The pit geometry, IR drop, mass transfer, surface concentration calculation and effect of more corrosive species can be addressed in future studies. Besides, more experimental data are needed to further validate this model.

7.3 Future development concepts: “super artificial pit” design

A “super artificial pit”, was intended for the future research in the middle or large scale tests. The concept of the design has been developed as shown in Figure 85. The big surface is the cathode. The pit is a thin wire fixed in a holder. The pit depth can be adjusted by a screw connection. Four pits can be assembled in one unit. The advantage of this design is that more area ratios and pit depth options can be configured rather easily and reproducibly. The pit interaction can be investigated by connecting different pits during tests. Several types of pit geometry can be configured in one test. This design has great versatility. It can be used in conjunction with various pieces of flow equipment.

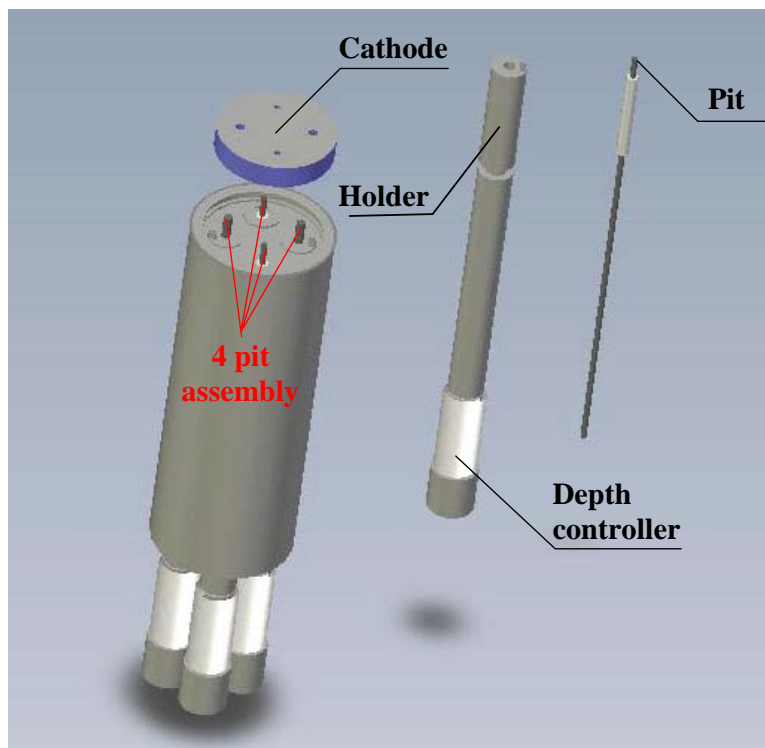


Figure 85. Scheme for super artificial pit design.

References

1. G.H. Koch, M.P.H. Brongers, N.G. Thompson, Y.P. Virmani and J.H. Payer, Corrosion Costs and Preventive Strategies in the United States, FWHA-RD-01-156, U.S. Department of Transportation, Federal Highway Administration (2002).
2. C. de Waard and D. E. Williams, Prediction of Carbonic Acid Corrosion in Natural Gas Pipelines, First International Conference on the Internal and External Protection of Pipes, Sept. 9th – 11th, University of Durham, Paper No. F1 (BHRA Fluid Engineering, Cranfield, Bedford, England, 1975).
3. C. de Waard and D. E. Williams, Carbonic Acid Corrosion of Steel, Corrosion, Vol. 31, No. 5, 1975, pp. 177–181.
4. G. Schmitt and B. Rothmann, Studies on the Corrosion Mechanism of Unalloyed Steel in Oxygen-Free Carbon Dioxide Solutions. Part I. Kinetics of the Liberation of Hydrogen, Werkstoffe und Korrosion, Vol. 29, 1977, pp. 816–822.
5. G. Schmitt and B. Rothmann, Studies on the Corrosion Mechanism of Unalloyed Steel in Oxygen-Free Carbon Dioxide Solutions. Part II. Kinetics of Iron Dissolution, Werkstoffe und Korrosion, Vol. 28, 1978, pp. 98–100.
6. A. Ikeda, M. Ueda and S. Mukai, Influence of Environmental Factors on Corrosion in CO₂ Source Well, Advances in CO₂ Corrosion (Editors: P. A. Burke, A. I. Asphanhani and B. S. Wright), Vol. 2, Houston: NACE, 1985, pp.1–22.
7. A. Ikeda, M. Ueda and S. Mukai, CO₂ Behavior of Carbon and Cr Steels, Advances in CO₂ Corrosion (Editors: R. H. Hausler and H. P. Godard), Vol. 1, Houston: NACE, 1985, pp.39–51.

8. D. M. Kern, The Hydration of Carbon Dioxide, *Journal of Chemical Education*, Vol 37, 1960, pp. 14.
9. L. G. S. Gray and B. G. Anderson, Mechanism of Carbon Steel Corrosion in Brines Containing Dissolved Carbon Dioxide at pH 4, *CORROSION/89*, paper No. 464 (Houston, TX: NACE, 1989).
10. L. G. S. Gray and B. G. Anderson, Effect of pH and Temperature on the Mechanism of Carbon Steel Corrosion by Aqueous Carbon Dioxide, *CORROSION/90*, paper No. 40 (Houston, TX: NACE, 1990).
11. C. de Waard and U. Lotz, Prediction of CO₂ Corrosion of Carbon Steel, *CORROSION/93*, paper No. 69 (Houston, TX: NACE, 1993).
12. C. de Waard, U. Lotz and A. Dugstad, Influence of Liquid Flow Velocity on CO₂ Corrosion: A Semi-empirical Model, *CORROSION/95*, paper No. 128 (Houston, TX: NACE, 1995).
13. B. F. M. Pots, Mechanistic Models for the Prediction of CO₂ Corrosion Rates under Multi-phase Flow Conditions, *CORROSION/95*, paper No. 137 (Houston, TX: NACE, 1995).
14. E. Gulbrandsen, J. Kvarekval and H. Miland, Effect of Oxygen Contamination on the Inhibition of CO₂ Corrosion, *CORROSION/2001*, paper No. 01054 (Houston, TX: NACE, 2001).
15. H.-H. Huang, W.-T. Tsai, and J.-T. Lee, Electrochemical Behavior of A516 Carbon Steel in Solutions Containing Hydrogen Sulfide, *Corrosion*, Vol. 52, No. 9, 1996, pp.708–713.

16. K.S. George and S. Nescic, Investigation of Carbon Dioxide Corrosion of Mild Steel in the Presence of Acetic Acid - Part 1: Basic Mechanisms, *Corrosion*, Vol. 63, No. 2, 2007, pp.178–186.
17. Y. Garsany and D. Pletcher, The Role of Acetate in CO₂ Corrosion of Carbon Steel: Has the Chemistry been Forgotten?, *CORROSION/2002*, paper No. 02273 (Houston, TX: NACE, 2002).
18. S. Nescic, J. Postlethwaite and S. Olsen, An Electrochemical Model for Prediction of Corrosion of Mild Steel in Aqueous Carbon Dioxide Solutions, *Corrosion*, Vol. 54, No. 4, 1996, 280–294.
19. E. W. J. van Hunnik and B. F. M. Pots, The Formation of Protective FeCO₃ Corrosion Product Layers in CO₂ Corrosion, *CORROSION/96*, paper No. 6 (Houston, TX: NACE, 1996).
20. S. Nescic, M. Nordsveen, R. Nyborg and A. Stangeland, A Mechanistic Model for CO₂ Corrosion with Protective Iron Carbonate Films, *CORROSION/2001*, paper No. 01040 (Houston, TX: NACE, 2001).
21. S. Nescic, K.-L. J. Lee and V. Ruzic, A Mechanistic Model of Iron Carbonate Film Growth and the Effect on CO₂ Corrosion of Mild Steel, *CORROSION/2002*, paper No. 237 (Houston, TX: NACE, 2002).
22. Keith George and S. Nešić; Investigation of Carbon Dioxide Corrosion of Mild Steel in the Presence of Acetic Acid—Part 1: Basic Mechanisms, *Corrosion*, Vol. 63, No. 2, 2007, pp. 178–186.

23. M. Nordsveen, S. Nestic, R. Nyborg and A. Stangeland, A Mechanistic Model for Carbon Dioxide Corrosion of Mild Steel in the Presence of Protective Iron Carbonate Films-Part1: Theory and Verification, *Corrosion*, Vol. 59, No. 5, 2003, pp.443–456.
24. S. Nestic, M. Nordsveen, R. Nyborg and A. Stangeland, A Mechanistic Model for Carbon Dioxide Corrosion of Mild Steel in the Presence of Protective Iron Carbonate Films-Part2: A Numerical Experiment, *Corrosion*, Vol. 59, No. 6, 2003, pp.489–497.
25. S. Nestic and K-L. J. Lee, A Mechanistic Model for Carbon Dioxide Corrosion of Mild Steel in the Presence of Protective Iron Carbonate Films-Part3: Film Growth Model, *Corrosion*, Vol. 59, No. 7, 2003, pp.616–628.
26. K. Chokshi, W. Sun and S. Nestic, Iron Carbonate Scale Growth and the Effect of Inhibition in CO₂ Corrosion of Mild Steel, *CORROSION/2005*, paper No. 05285 (Houston, TX: NACE, 2005).
27. O. A. Nafday and S. Nestic, Iron Carbonate Scale Formation and CO₂ Corrosion in the Presence of Acetic Acid, *CORROSION/2005*, paper No. 05295 (Houston, TX: NACE, 2005).
28. U. R. Evans, *An Introduction to Metallic Corrosion*, (3rd Edition), Arnold, London: Edward Arnold Publisher Ltd., 1981, pp. 36.
29. D. A. Jones, *Principles and Prevention of Corrosion*, (2nd Edition), Upper Saddle River, NJ: Prentice Hall, Inc., 1996, pp. 191–196.
30. M. W. Joosten, T. Johnsen, H. H. Hardy, J. Jossang and J. Feder, Fractal Behavior of CO₂ Pits, *CORROSION/92*, paper No. 406 (Houston, TX: NACE, 1992).

31. M. W. Joosten T. Johnsen, A. Dugstad, T. Walmann, J. Jossang, P. Meakin and J. Feder, In Situ Observation of Localized CO₂ Corrosion, CORROSION/94, paper No. 3 (Houston, TX: NACE, 1994).
32. K. Videm and A. Dugstad, Corrosion of Mild steel in an Aqueous Carbon Dioxide Environment. Part 1: Solution Effects, Material Performance, 1989, pp. 63–67.
33. K. Videm and A. Dugstad, Corrosion of Mild Steel in an Aqueous Carbon Dioxide Environment. Part 2: Scale Formation, Material Performance, 1989, pp. 46–50.
34. K. Videm and A. M. Koren, Corrosion, Passivity and Pitting of Carbon Steel in Aqueous Solutions of HCO₃⁻, CO₂ and Cl⁻, CORROSION/92, paper No. 12 (Houston, TX: NACE, 1992).
35. K. Videm, Fundamental Studies Aimed at Improving Models for Prediction of CO₂ Corrosion of Carbon Steels, Progress in the Understanding and Prevention of Corrosion, Vol. 1: Barcelona, Spain, 1993, pp.504–512.
36. A. Marie, K. Halvorsen and T. Sønvedt, CO₂ Corrosion Model for Carbon Steel including a Wall Shear Stress Model for Multiphase Flow and Limits for Production to Avoid Mesa Attack, CORROSION/99, paper No. 42 (Houston, TX: NACE, 1999).
37. M. H. Achour, J. Kolts, A. H. Johannes and G. Liu, Mechanistic Modeling of Pit Propagation in CO₂ Environment under High Turbulence Effects, CORROSION/93, paper No. 87, (Houston, TX: NACE, 1993).
38. S. Nesic, Y. Xiao and B. F. M. Pots, A Qusia 2-D Localized Corrosion Model, CORROSION/2004, paper No. 628 (Houston, TX: NACE, 2004).

39. G. Schmitt, W. Bucken and R. Fanebust, Modeling Microturbulences at Surface Imperfections as Related to Flow – Induced Localized Corrosion, *Corrosion*, Vol. 48, No. 5, 1991, pp. 431–440.
40. G. Schmitt and M. Horstemeier, Fundamental Aspects of CO₂ Metal Loss Corrosion – Part II: Influence of Different Parameters on CO₂ Corrosion Mechanism, *CORROSION/2006*, paper No. 06112, (Houston, TX: NACE, 2006).
41. G. Schmitt, T. Gudde and E. Strobel-Effertz, Fracture Mechanical Properties of CO₂ Corrosion Product Scales and Their Relation to Localized Corrosion, *CORROSION/96*, paper No. 9, (Houston, TX: NACE, 1996).
42. G. Schmitt, C. Bosch, U. Pankoke, W. Bruckhoff and G. Siegmund, Evaluation of Critical Flow Intensities for FILC in Sour Gas Production, *CORROSION/98*, paper No. 46, (Houston, TX: NACE, 1998).
43. G. Schmitt, M. Mueller, M. Papenfuss and E. Strobel-Effertz, Understanding Localized CO₂ Corrosion of Mild Steel from Physical Properties of Iron Carbonate Scales, *CORROSION/99*, paper No. 38 (Houston, TX: NACE, 1999).
44. G. Schmitt, M Mueller, Critical Wall Shear Stresses in CO₂ Corrosion of Carbon Steel, *CORROSION/2002*, paper No. 44, (Houston, TX: NACE, 2002).
45. G. Schmitt and S. Feinen, Effect of Anions and Cations on the Pit Initiation in CO₂ Corrosion of Iron and Steel, *CORROSION/2000*, paper No. 00001, (Houston, TX: NACE, 2000).

46. G. Schmitt, C. Bosch, P. Plagemann and K. Moeller, Local Wall Shear Stress Gradients in the Slug Flow Regime – Effect of Hydrocarbon and Corrosion Inhibitor, CORROSION/2002, paper No. 02244, (Houston, TX: NACE, 2002).
47. C. F. Chen, M. X. Lu, D. B. Sun, Z. H. Zhang and W. Chang, Effect of Chromium on the Pitting Resistance of Oil Tube Steel in a Carbon Dioxide Corrosion System, Corrosion, Vol. 61, No. 6, 2005, pp. 594–601.
48. Z. Xia, K. – C. Chou and Z. Szklarska-Smialowska, Pitting Corrosion of Carbon Steel in CO₂-Containing NaCl Brine, Corrosion, Vol. 45, No. 8, 1989, pp. 636–642.
49. J. L. Crolet, Which CO₂ Corrosion, Hence Which Prediction? in Predicting CO₂ Corrosion in the Oil and Gas Industry, London: The Institute of Materials, 1994, pp. 1–26.
50. R. Nyborg and A. Dugstad, Mesa Corrosion Attack in Carbon Steel and 0.5% Chromium Steel, CORROSION/98, paper No. 29 (Houston, TX: NACE, 1998).
51. A. Dugstad, Mechanism of Protective Film Formation during CO₂ Corrosion of Carbon Steel, CORROSION/98, paper No. 31 (Houston, TX: NACE, 1998).
52. R. Nyborg, Initiation and Growth of Mesa Corrosion Attack during CO₂ Corrosion of Carbon Steel, CORROSION/98, paper No. 48 (Houston, TX: NACE, 1998).
53. R. Nyborg and A. Dugstad, Understanding and Prediction of Mesa Corrosion, CORROSION/2003, paper No. 642 (Houston, TX: NACE, 2003).
54. Yuhua Sun, Keith George and Srdjan Nešić, The Effect of Cl⁻ and Acetic Acid on Localized CO₂ Corrosion in Wet Gas Flow, CORROSION/2003, paper No. 03327 (Houston, TX: NACE, 2003).

55. Y. Sun and S. Netic, A Parametric Study and Modeling on Localized CO₂ Corrosion in Horizontal Wet Gas Flow, CORROSION/2004, paper No. 04380 (Houston, TX: NACE, 2004).
56. J. Han, Y. Yang, B. Brown and S. Netic, Electrochemical Investigation of Localized CO₂ Corrosion on Mild Steel, CORROSION/2007, paper No. 07323, (Houston, TX: NACE, 2007)
57. J. Han, Y. Yang, B. Brown and S. Netic, Roles of Passivation and Galvanic Effects in Localized CO₂ Corrosion of Mild Steel, CORROSION/2008, paper No. 08332, (Houston, TX: NACE, 2008)
58. J. Han, D. Young, S. Nešić and A. Tripathi, Characterization of the Passive Films on Mild Steel in CO₂ Environments, ICC/2008, paper No. 2511 (Las Vegas, NV).
59. J. Han, Srdjan Nešić and B. N. Brown, Galvanic Model for Localized CO₂ Corrosion, ICC/2008, paper No. 2687 (Las Vegas, NV).
60. J. Han, S. Nešić and B. N. Brown, Investigation of the Galvanic Mechanism for Localized CO₂ Corrosion Propagation Using the Artificial Pit Technique, Corrosion, 2009 (in press).
61. J. Han, B. N. Brown, D. Young and S. Nešić, Mesh-capped Probe Design for Direct pH Measurements at an Actively Corroding Metal Surface, Journal of the Applied Electrochemistry (in press).
62. J. Han, D. Young, H. Colijn, A. Tripathi and S. Nešić, Chemistry and Structure of the Passive Film on Mild Steel in CO₂ Environments, Industrial & Engineering Chemistry Research, Vol. 48, 2009, pp. 6296-6302.

63. A. Turnbull, D. Coleman, A. J. Griffiths, P. E. Francis and L. Orkney, Effectiveness of Corrosion Inhibitors in Retarding the Rate of Propagation of Localized Corrosion, *Corrosion*, Vol. 59, No. 3, 2003, pp. 250–257.
64. J. Marsh, J. W. Palmer and R. C. Newman, Evaluation of Inhibitor Performance for Protection against Localized Corrosion, *CORROSION/2002*, paper No. 288, (Houston, TX: NACE, 2002).
65. H. Smith, On Equilibrium in the System: Ferrous Carbonate, Carbon Dioxide and Water, *Journal of the American Chemical Society*, Vol. 40, 1918, pp. 879–883.
66. P. C. Singer and W. Stumm, The Solubility of Ferrous Iron in Carbonate Bearing Waters, *J. Am. Water Works Assoc.*, Vol. 62, 1970, pp. 198–202.
67. J. Bruno, P. Wersin and W. Stumm, On the Influence of Carbonate in Mineral Dissolution: II. The Solubility of FeCO_3 (s) at 25 °C and 1 atm Total Pressure, *Geochimica et Cosmochimica Acta*, Vol. 56, 1992, pp. 1149–1155.
68. J. Greenberg and M. Tomson, Precipitation and Dissolution Kinetics and Equilibria of Aqueous Ferrous Carbonate vs. Temperature, *Applied Geochemistry*, Vol. 7, 1992, pp. 185–190.
69. A. Dugstad, The Importance of FeCO_3 Supersaturation on the CO_2 Corrosion of Carbon Steels, *CORROSION/92*, paper No. 14 (Houston, TX: NACE, 1992).
70. W. Preis, H. Gamsjäger, Thermodynamic Investigation of Phase Equilibria in Metal Carbonate–Water–Carbon Dioxide System, *Monatshefte für Chemie*, Vol. 132, 2001, pp. 1327–1346.

71. D. L. Jensen, J. K. Boddum, J. C. Tjell and T. H. Christensen, The Solubility of Rhodochrosite (MnCO_3) and Siderite (FeCO_3) in Anaerobic Aquatic Environments, *Applied Geochemistry*, Vol. 17, 2002, pp. 503–511.
72. W. Preis and H. Gamsjäger, Critical Evaluation of Solubility Data: Enthalpy of the Formation of Siderite, *Phys. Chem. Chem. Phys.*, Vol. 4, 2002, pp. 4014–4019.
73. C. A. R. Silva, X. Liu and F. J. Millerol, Solubility of Siderite (FeCO_3) in NaCl Solutions, *Journal of Solution Chemistry*, Vol. 31, No. 2, 2002, pp. 97–108.
74. G. M. Marion, D. C. Catling and J. S. Kargel, Modeling Aqueous Ferrous Iron Chemistry at Low Temperatures with Application to Mars, *Geochimica et Cosmochimica Acta*, Vol. 67, No. 22, 2003, pp. 4251–4266.
75. Nesic, S., Corrosion Center, Ohio University, personal communication, 2007.
76. W. Sun, S. Nešić, R. C. Woollam, The Effect of Temperature and Ionic Strength on Iron Carbonate (FeCO_3) Solubility Limit, *Corrosion Science* Vol. 51, No 6, 2009, pp. 1273–1276.
77. T. Engel, P. Reid, *Thermodynamics, Statistical Thermodynamics and Kinetics*, San Francisco: Pearson, 2006, pp. 230–234.
78. The Nobel Foundation,
http://nobelprize.org/educational_games/physics/microscopes/tem/index.html,
accessed time: Nov. 18, 2008.
79. C. R. Brundle, C. A. Evans, Jr. and S. Wilson, *Encyclopedia of Materials Characterization: Surfaces, Interfaces, Thin Films*, Boston: Butterworth-Heinemann, 1992, pp. 72–84, 120–134.

80. A. R. West, *Solid State Chemistry and its Applications*, Chichester, West Sussex, England: John Wiley & Sons, Ltd., 1998, pp. 115–186.
81. S. A. Stepanov, *Grazing-Incidence X-Ray Diffraction*, 3th Autumn School on X-ray Scattering from Surfaces and Thin Layers, Smolenice, Slovakia, October 1–4, 1997.
82. B. K. Tanner, T. P. A. Hase, T. A. Lafford and M. S. Goorsky, *Grazing Incidence in-Plane X-Ray Diffraction in the Laboratory*, JCPDS - International Centre for Diffraction Data 2004, *Advances in X-ray Analysis*, Vol. 47, 2004, pp. 309–314.
83. S. Sembiring, B. O'Connor, D. Li, A. van Riessen and C. Buckley, I. Low and R. De Marco, *Grazing Incidence X-Ray Diffraction Characterization of Corrosion Deposits Induced by Carbon Dioxide on Mild Steel*, JCPDS - International Centre for Diffraction Data 2004, *Advances in X-ray Analysis*, Vol. 43, 2004, pp. 319–325.
84. J. C. Vickerman, *Surface Analysis - The Principal Technique*, Chichester, West Sussex, England: John Wiley & Sons, Ltd., 2005, pp. 215–266, 393–449.
85. M. Pourbaix, *Atlas of Electrochemical Equilibria in Aqueous*, (English Edition), Oxford: Pergamon Press, 1966, pp. 307–321.
86. X. -P. Guo and Y. Tomoe, *The Effect of Corrosion Product Layers on the Anodic and Cathodic Reactions of Carbon Steel in CO₂ Saturated MDEA Solutions at 100°C*, *Corrosion Science*, Vol. 41, 1999, pp. 1391–1402.
87. J. K. Heuer and J. F. Stubbins, *An XPS Characterization of FeCO₃ Films from CO₂ Corrosion*, *Corrosion Science*, Vol. 41, 1999, pp. 1231–1243.

88. R. De Marco, Z. Jiang, B. Pejic and E. Poinen, An In Situ Synchrotron Radiation Grazing Incidence X-Ray Diffraction Study of Carbon Dioxide Corrosion, *Journal of The Electrochemical Society*, Vol.152, No. 10, 2005, pp. B389–B392.
89. R. De Marco, Z. Jiang, D. John, M. Sercombe and B. Kinsella, An in situ Electrochemical Impedance Spectroscopy/Synchrotron Radiation Grazing Incidence X-ray Diffraction Study of the Influence of Acetate on the Carbon Dioxide Corrosion of Mild Steel, *Electrochimica Acta*, Vol. 52, 2007, pp. 3746–3750.
90. H. S. W. Chang, C. C. Chiou and Y. W. Chen, Synthesis, Characterization, and Magnetic Properties of Fe₃O₄ Thin Films Prepared via a Sol–Gel Method, *Journal of Solid State Chemistry*, Vol. 128, 1997, pp. 87–92.
91. D L. Graf, Crystallographic Tables for the Rhombohedral Carbonates, *American Mineralogist*, Vol. 46, 1961, pp. 1283-1316.
92. H. M. Rietveld, A Profile Refinement Method for Nuclear and Magnetic Structures, *Journal of Applied Crystallography*, Vol. 2, No. 2, 1969, pp. 65-71.
93. B. MacDougall and M. J. Graham, Chapter 6: Growth and Stability of Passive Films in Corrosion Mechanisms in Theory and Practice (2ed), Marcus, P. (editor); Marcel Dekker, Inc.: New York, 2002, p.190.
94. S.C. Dexter and S.H. Lin, Calculation of Seawater pH at Polarized Metal Surfaces in the Presence of Surface Films, *Corrosion*, Vol. 48, No. 1, 1992, pp. 50-60.
95. D. M. Drazic, S. Djordjevic, M. Vojnovic and B. Pastrovic, Promene pH uz Provrsinu electrode pri izdvajanju vodonika, 1969.

96. D. M. Drazic, The Influence of Diffusion Controlled Hydrogen Evolution Reaction on the Kinetics of Codeposition of Cobalt (The original paper was published at 20-th CITCE meeting Strasburg 1969).
97. T. Yoshinobu, H. Iwasaki, M. Nakao, S. Nomura, T. Nakanishi, S. Takamatsu and K. Tomita, Application of Chemical Imaging Sensor to Electro Generated pH Distribution, Japanese Journal of Applied Physics, Vol. 37, 1998, pp. L353–L355.
98. T. Yoshinobu, T. Harada and H. Iwasaki, Application of pH-Imaging Sensor to Determining the Diffusion Coefficients of Ions in Electrolytic Solutions, Japanese Journal of Applied Physics, Vol. 39, 2000, pp. L318–L320.
99. F. King, C. D. Litke and Y. Tang, Effect of Interfacial pH on the Reduction of Oxygen on Copper in Neutral NaClO_4 Solution, Journal of Electroanalytical Chemistry, Vol. 384, 1995, pp. 105–113.
100. L. T. Romankiw, Specific Ion Activity Measurement at an Electrode during Electrolysis, IBM Technical Disclosure Bulletin, Vol. 13, No. 1, 1970, pp. 69–70.
101. L. T. Romankiw, pH Changes at the Cathode during Electrolysis on Ni, FeCu and their Alloys and a Simple Technique for Measuring pH Changes at Electrodes, Proceedings of the Symposium on Electrodeposition Technology, Theory and Practice, 1987, pp. 301–325.
102. H. Deligianni and L. T. Romankiw, In Situ Surface pH Measurement during Electrolysis Using a Rotating pH Electrode, IBM J. Res. Develop., Vol. 37, No. 2, 1993, pp. 85–95.

103. J. Ji, W. C. Cooper, D. B. Dreisinger and E. Peters, Surface pH Measurements during Nickel Electrodeposition, *Journal of Applied electrochemistry*, Vol. 25, 1995, pp. 642–650.
104. C. Deslouis, I. Frateur, G. Maurin and B. Tribollet, Interfacial pH Measurement during the Reduction of Dissolved Oxygen in a Submerged Impinging Jet Cell, *Journal of Applied Electrochemistry*, Vol. 27, 1997, pp.482–492.
105. S. L. Diaz, O. R. Mattos, O. E. Barcia and F. J. Fabri Miranda, ZnFe Anomalous Electrodeposition: Stationaries and Local pH Measurements, *Electrochimica Acta*, Vol. 47, 2002, pp. 4091–4100.
106. A. P. Ordine, S.L. Diaz, I. C. P. Margarit, O.E. Barcia and O. R. Mattos, Electrochemical Study on Ni–P Electrodeposition, *Electrochimica Acta*, Vol. 51, 2006, pp. 1480–1486.
107. M. Nobial, O. Devos, O. Rosa Mattos and B. Tribollet, The Nitrate Reduction Process: A way for Increasing Interfacial pH, *Journal of Electroanalytical Chemistry*, Vol. 600, 2007, pp. 87–94.
108. Z. Lewandowski, W. C. Lee, W.G. Charazklis and B. Little, Dissolved Oxygen and pH Microelectrode Measurements at Water-Immersed Metal Surfaces, *Corrosion*, Vol. 45, No. 2, 1989, pp. 92–98.
109. C. Wei, A. J. Bard, G. Nagy and K. Toth, Scanning Electrochemical Microscopy. 28. Ion-Selective Neutral Carrier-based Microelectrode Potentiometry, *Analytical Chemistry*, Vol. 67, 1995, pp. 1346–1356.

110. J. Park, C.-H. Paik and H. C. Alkire, Scanning Microsensors for Measurement of Local pH Distributions at the Microscale, *Journal of the Electrochemical Society*, Vol. 143, No. 8, 1996, pp. L174–L176.
111. E. Klusmann and J. W. Schultze, pH-Microscopy – Theoretical and Experimental Investigations, *Electrochimica Acta*, Vol. 42, 1997, pp. 3123–3134.
112. T. Honda, K. Murase, T. Hirato and Y. Awakura, pH Measurement in the Vicinity of a Cathode Evolving Hydrogen Gas Using an Antimony Microelectrode, *Journal of Applied Electrochemistry*, Vol. 28, 1998, pp. 617–622.
113. E. Tada, K. Sugawara and H. Kaneko¹, Distribution of pH during Galvanic Corrosion of a Zn/steel Couple, *Electrochimica Acta*, Vol. 49, 2004, pp. 1019–1026.
114. Y.-S. Choi, J. J. Shim and J. G. Kim, Effects of Chromium, Cobalt, Copper, Nickel, and Calcium on the Corrosion Behavior of Low-Carbon Steel in Synthetic Groundwater, *Corrosion*, Vol. 61, No. 5, 2005, pp. 490–497.
115. M. Eisenberg, C. W. Tobias and C. R. Wilke, Ionic mass transfer and concentration polarization at rotating electrodes, *J. Electrochemical Society*, Vol. 101, 1954, p. 306-319.
116. F. P. Berger and K. Hau, Mass transfer in turbulent pipe flow measured by the electrochemical method, *International Journal of Heat Mass and Transfer*, Vol. 20, 1977, pp. 1185-1194.
117. S. Nestic, B. F. M. Pots, J. Postlethwaite, and N. Thevenot, Superposition of diffusion and chemical reaction controlled limiting currents – application to CO₂ corrosion, *J. Corrosion Science and Engineering*, ISSN, 1466-8858, 1995.